Search for supersymmetry in diphoton final states with the Compact Muon Solenoid experiment

Matthew Lawrence Joyce
Jewell Ridge, Virginia

M.S., Virginia Polytechnic Institute and State University, 2008

A Dissertation presented to the Graduate Faculty of the University of Virginia in Candidacy for the Degree of Doctor of Philosophy

Department of Physics

University of Virginia
October 2021

ABSTRACT

This document presents a search for new physics having final states with two photons and missing transverse energy. Data from proton-proton collisions with a center of mass energy of $\sqrt{s} = 13$ TeV were used. Said data was collected at the CERN LHC in the years 2016-2018 and make up a total integrated luminosity of 137 fb^{-1}. Interpretation of the results was done in the context of gauge mediated supersymmetry breaking or more specifically the T5gg and T6gg simplified models. The T5gg model is one where gluino pairs are produced which yield neutralinos which then each decay into a gravitino and a photon. In the T6Wg model squark pairs are produced which yield neutralinos and then, as in the T5Wgg, each neutralino decays to a gravitino and a photon. The gravitino would escape the detector undetected and therefore lead to a final state with missing transverse energy and two photons. No significant excess was observed above the expected standard model backgrounds. Lower limits were placed on the masses of the squarks and gluinos in the context of gauge mediated supersymmetry breaking. Models with squark masses below 1.79 TeV were excluded at a 95% confidence level as were models with gluino masses below 2.08 TeV.

"Physics is a lot like life, and you're going to have disappointments. The issue is how you come back from them."

— Frank Beamer (modified)

CONTENTS

LIST OF FIGURES

LIST OF TABLES

ACKNOWLEDGEMENTS

There are so many people that I would like to thank for making this possible, but there just isn't enough space here to thank them all. I would first like to thank my advisor, Brad Cox. You struck a great balance of letting me figure things out on my own and helping me when I found myself in the weeds. I like to think that you've molded me into a physicist that can do "useful things" and not one of those physicists that "thinks the ntuples just come out of a pipe on the detector". Thank you Chris Neu for being a great colleague and friend. I appreciate all of your advice, both personal and professional, and for being there when I was going through some tough times.

Thank you Steve Boi for your friendship and making the tomes of homework more tolerable. I don't think I would have made it without the alliance we forged. Thank you Thomas Anderson for being the guy that makes HEP run and more importantly for becoming such a good friend. You helped me fix too many things to count and you made the many drives to Fermilab enjoyable. I will miss our long discussions over coffee and sometimes wine.

Last but certainly not least, I would like to thank my family. Heather, it is safe to say that without your support I would not have even started the PhD program. You had faith in me even when I didn't have it in myself.

Thank you for believing in me and making me believe in myself. Thank you Dad for pushing me in the right directions throughout my life and teaching me how to work hard and pursue my dreams. Thank you Mom for all of the love and support you've shown me over the years. You always told me I could be anything I wanted and you were right.

1. THE STANDARD MODEL OF PARTICLE PHYSICS

1.1 The Standard Model

The Standard Model (SM) of particle physics is a Lorentz-invariant quantum field theory (QFT) that describes the dynamics of elementary particles. Three critical developments leading to the formation of the SM, as described by Steven Weinberg[48], were the quark model proposed by Gell-Mann[31] and Zweig[51] in 1964, the idea of gauge symmetry by Yang and Mills[50] in 1954, and the notion of spontaneous gauge symmetry breaking proposed by Goldstone[33] in 1961. This ultimately led to the SM in its current form as a gauge theory with the symmetry group

$$G_{SM} = SU(3)_C \otimes SU(2)_L \otimes U(1)_Y \tag{1.1}$$

where $SU(3)_C$ is responsible for strong interactions and $SU(2)_L \otimes U(1)_Y$ is responsible for unified electromagnetic and weak interactions, also known as electroweak interactions.

Associated with each of these symmetry groups is a set of massless spin-1 vector fields called gauge bosons. These are listed in Table 1.1 along with the associated charge or generator for that group. There are eight such gauge bosons in $SU(3)_C$ called gluons $G_\mu^{1,\ldots,8}$. There are three gauge bosons $W_\mu^{1,2,3}$

in $SU(2)_L$ and one gauge boson B_μ in $U(1)_Y$. The gauge bosons mediate the interactions between spin-1/2 fields ψ, spin-0 fields ϕ, and spin-1 fields for non-Abelian gauge fields. At this point it's worth noting that the W^3 and B gauge fields are not observable bosons, but are mixed by electroweak symmetry breaking to produce observable bosons. The details of this will be covered in Section 1.2.

There are twelve fermion fields which can be split into six lepton fields and six quark fields. Both quarks and leptons are comprised of three generations. For quarks there are three "up-type" quarks (up u, charm c, and top t) and three "down-type" quarks (down d, strange s, and bottom b). The lepton fields are electron e, muon μ, tau τ, and three neutrino fields ν_e, ν_μ, and ν_τ. The fermion fields and their representations under G_{SM} are listed in Table 1.2. Each fermion field can be expressed in terms of left and right chirality fields, which are represented by doublets ψ_L in the left-handed case and singlets ψ_R in the right-handed case with

$$\psi = \psi_R + \psi_L \tag{1.2}$$
$$\psi_R = \frac{1}{2}(1+\gamma^5)\psi \tag{1.3}$$
$$\psi_L = \frac{1}{2}(1-\gamma^5)\psi \tag{1.4}$$

The SM also contains a complex scalar doublet field ϕ called the Higgs field in honor of Peter Higgs, who was among one of the physicists who proposed its existence in 1964 [35].

The strong interaction is described by the theory of quantum chromodynamics (QCD). The Lagrangian for the QCD interaction can be written

Tab. 1.1: Boson fields in the SM

Symbol	Associated Charge	Symmetry group
B_μ	weak hypercharge Y	$U(1)_Y$
$G_\mu^{1,\ldots,8}$	color $C = (r, g, b)$	$SU(3)_C$
$W_\mu^{1,2,3}$	weak isospin T_3	$SU(2)_L$

as

$$\mathcal{L}_{QCD} = \bar{\psi}(i\gamma^\mu D_\mu)\psi - \frac{1}{2}TrG_{\mu\nu}G^{\mu\nu} \tag{1.5}$$

where

$$G_{\mu\nu} = \partial_\mu G_\nu - \partial_\nu G_\mu - ig_s[G_\mu, G_\nu] \tag{1.6}$$

$$D_\mu = \partial_\mu - ig_s G_\mu \tag{1.7}$$

and g_s is related to the strong coupling constant.

1.2 Electroweak Symmetry Breaking

A crucial feature of the SM is electroweak symmetry breaking. The electroweak interaction, first proposed by Glashow, Weinberg, and Salam in the 60's, is the unified description of electromagnetic and weak interactions under the $SU(2)_L \otimes U(1)_Y$ symmetry. The electromagnetic interaction is described by quantum electrodynamics (QED), which is an Abelian gauge theory under the $U(1)_{EM}$ symmetry group. The gauge boson in QED is the photon and couples to electric charge Q. The QED Lagrangian is given by

$$\mathcal{L}_{QED} = \bar{\psi}(i\gamma^\mu D_\mu - m)\psi - \frac{1}{4}F_{\mu\nu}F^{\mu\nu} \tag{1.8}$$

Tab. 1.2: Fermions in the SM. The first two numbers listed in the third column give the supermultiplet representation under $SU(3)_C$ and $SU(2)_L$ respectively. A **1** means that it is not charged under that group and therefore will not couple to the associated force. A **3** as the first number means that it has color charge and couples to the strong force. A **2** for the second number means that it has weak isospin and couples to the weak force. The third number gives the value of the weak isospin. Adjoint representation is specified by the presence of a bar over the number.

Name	Notation	Representation under $SU(3)_C \otimes SU(2)_L \otimes U(1)_Y$
Left-handed quark doublet	$\begin{pmatrix} u_L \\ d_L \end{pmatrix}, \begin{pmatrix} c_L \\ s_L \end{pmatrix}, \begin{pmatrix} t_L \\ b_L \end{pmatrix}$	$(3,\ 2,\ \frac{1}{6})$
Right-handed up-type quark singlet	$u_R^\dagger,\ c_R^\dagger,\ b_R^\dagger$	$(\bar{3},\ 1,\ \text{-}\frac{2}{3})$
Right-handed down-type quark singlet	$d_R^\dagger,\ s_R^\dagger,\ t_R^\dagger$	$(\bar{3},\ 1,\ \frac{1}{3})$
Left-handed lepton doublet	$\begin{pmatrix} \nu_{eL} \\ e_L \end{pmatrix}, \begin{pmatrix} \nu_{\mu L} \\ \mu_L \end{pmatrix}, \begin{pmatrix} \nu_{\tau L} \\ \tau_L \end{pmatrix}$	$(1,\ 2,\ \text{-}\frac{1}{2})$
Right-handed charged lepton singlet	$e_R^\dagger,\ \mu_R^\dagger,\ \tau_R^\dagger$	$(\bar{1},\ 1,\ 1)$

where

$$F_{\mu\nu} = \partial_\mu A_\nu - \partial_\nu A_\mu \tag{1.9}$$

$$D_\mu = \partial_\mu + ieQA_\mu \tag{1.10}$$

and A_μ is the electromagnetic or photon field.

The Lagrangian for the unbroken $SU(2)_L \otimes U(1)_Y$ symmetry is given by

$$\mathcal{L}_{EW} = \bar{\psi} i\gamma^\mu D_\mu \psi - Tr\frac{1}{8}W_{\mu\nu}W^{\mu\nu} - \frac{1}{4}B_{\mu\nu}B^{\mu\nu} \tag{1.11}$$

where

$$W_{\mu\nu} = \partial_\mu W_\nu - \partial_\nu W_\mu - ig_w[W_\mu, W_\nu] \tag{1.12}$$

$$B_{\mu\nu} = \partial_\mu B_\nu - \partial_\nu B_\mu \tag{1.13}$$

with a separate fermion term for each field ψ_R and ψ_L. The covariant derivative D_μ is given by

$$D_\mu = \partial_\mu + ig_w T_j W_\mu^j + ig_Y \frac{Y}{2} B_\mu \tag{1.14}$$

with W^j_μ and T_j written in terms of raising and lowering operators

$$W^{\pm}_\mu = \frac{1}{\sqrt{2}}(W^1_\mu \mp iW^2_\mu) \tag{1.15}$$

$$T^{\pm} = \frac{1}{\sqrt{2}}(T_1 \pm iT_2) \tag{1.16}$$

$$W^0_\mu = W^3_\mu \tag{1.17}$$

$$T^0 = T_3 \tag{1.18}$$

The neutral portion of the covariant derivative $ig_w T_3 W^3_\mu + ig_Y \frac{Y}{2} B_\mu$must contain the electromagnetic term $ieAQ$ for the electromagnetic interaction to be unified with the weak interaction, so the W^3_μ and B_μ fields need to linear combinations of the photon field A_μ and another field Z_μ. After symmetry breaking, which is discussed a little later in this section, this relationship can be written in terms of the electroweak mixing angle θ_w, also known as the Weinberg angle, as

$$\begin{pmatrix} A_\mu \\ Z_\mu \end{pmatrix} = \begin{pmatrix} \cos\theta_W & \sin\theta_W \\ -\sin\theta_W & \cos\theta_W \end{pmatrix} \begin{pmatrix} B_\mu \\ W^3_\mu \end{pmatrix} \tag{1.19}$$

The weak isospin T_3 and weak hypercharge Y can be related to the electric charge Q with the Gell-Mann-Nishijima formula

$$Y = 2(Q - T_3) \tag{1.20}$$

and the coupling constants g_w, g_Y, and e are related to the mixing angle by

$$e = g_w \cos\theta_W = g_Y \sin\theta_W \tag{1.21}$$

$$\sin\theta_W = \frac{g_Y}{\sqrt{g_w^2 + g_Y^2}} \tag{1.22}$$

$$\cos\theta_W = \frac{g_w}{\sqrt{g_w^2 + g_Y^2}} \tag{1.23}$$

At this point the $W_\mu^{1,2,3}$ and B_μ fields have been mixed to produce the observable fields W_μ^+, W_μ^-, A_μ, and Z_μ, but this is still inconsistent with experimental observations as these bosons and all of the fermions are still massless in this model. In order to generate the masses while maintaining the renormalizability of the gauge theory,which relies on the symmetry of the Lagrangian, the symmetry needs to be spontaneously broken. The symmetry is still in the Lagrangian but appears to be broken by the ground state. This is done by the introduction of a complex scalar doublet field called the Higgs field which is expressed as

$$\phi = \begin{pmatrix} \phi^+ \\ \phi^0 \end{pmatrix} = \frac{1}{\sqrt{2}} \begin{pmatrix} \phi_1 + i\phi_2 \\ \phi_3 + i\phi_4 \end{pmatrix} \tag{1.24}$$

where the fields ϕ_i are real scalar fields. The Lagrangian for the Higgs field is

$$\mathcal{L}_{Higgs} = (D_\nu \phi)^\dagger (D^\nu \phi) - V(\phi^\dagger \phi) \tag{1.25}$$

with the potential $V(\phi^\dagger\phi)$ being given by

$$V(\phi^\dagger\phi) = \mu^2\phi^\dagger\phi + |\lambda|(\phi^\dagger\phi)^2 \tag{1.26}$$

and the covariant derivative

$$D_\nu = \partial_\nu - \frac{i}{2}g_w W^i_\nu\sigma_i - \frac{i}{2}g_Y B_\nu \tag{1.27}$$

Since $\mu^2 < 0$, this potential has the shape of a sombrero as is shown in Figure 1.1. The scalar fields have some positive vacuum expectation value (VEV) satisfying

$$\phi^\dagger\phi = v^2 = -\frac{\mu^2}{\lambda} \tag{1.28}$$

at the minimum which allows us to write the ground state as

$$\phi_{ground} =< 0|\phi|0 >= \frac{1}{\sqrt{2}}\begin{pmatrix} 0 \\ v \end{pmatrix} \tag{1.29}$$

Expanding the Higgs field about it's minimum as

$$\phi_{ground} \to \phi(x) = \frac{1}{\sqrt{2}}e^{i\sigma_\alpha\theta^\alpha(x)}\begin{pmatrix} 0 \\ v + h(x) \end{pmatrix}, \alpha = 1, 2, 3 \tag{1.30}$$

results in a massive field $h(x)$ and and three massless scalar fields, or Goldstone bosons, $\theta_{1,2,3}$ which represent degrees of freedom. By then transforming into the unitary gauge we can remove the phase factor, thereby eliminating the explicit appearance of the three Goldstone bosons in the

Lagrangian. In gauging away the Goldstone bosons, the three degrees of freedom reappear as longitudinal polarization states of the W^+, W^-, and Z bosons. In other words, the W and Z bosons have become massive by "eating" the Goldstone bosons.

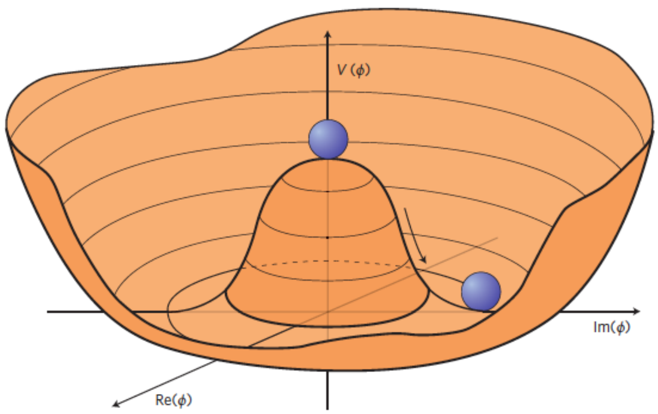

Fig. 1.1: The Higgs potential is shown as a function of the complex scalar field's real and imaginary parts. The balls illustrate that the stable vacuum state of nature is not located at $\phi = 0$ because the symmetry at that point is spontaneously broken. Instead the stable vacuum state of nature is located somewhere along the circle of minimum potential. Reprint from [7]

Writing the Lagrangian in Equation 1.25 in terms of the physical W and Z fields and evaluating at the VEV gives

$$\begin{aligned}\mathcal{L}_{Higgs} =& \frac{1}{2}\partial_\nu h \partial^\nu h + \frac{1}{4} g_w^2 W_\nu^+ W^{-\nu}(v+h)^2 \\ &+ \frac{1}{8}\frac{g_w^2}{\cos^2\theta_W} Z_\nu Z^\nu (v+h)^2 - V[\frac{1}{2}(v+h)^2]\end{aligned} \tag{1.31}$$

The v^2 terms give the W and Z boson masses and the h^2 term gives the mass of the Higgs boson as

$$M_W = \frac{1}{2} g_w v \tag{1.32}$$

$$M_Z = \frac{1}{2} v \frac{g_w}{\cos\theta_W} = \frac{M_W}{\cos\theta_W} \tag{1.33}$$

$$M_H = \sqrt{2}|\mu| \tag{1.34}$$

while the photon remains massless.

Charged leptons and quarks also acquire mass through Yukawa interactions via the Higgs mechanism. For leptons the Yukawa interaction has the form of

$$\mathcal{L}_{Yukawa} = -G_e[\bar{e_R}\phi^\dagger \ell_L + \bar{\ell_L}\phi e_R] \tag{1.35}$$

where

$$\ell_L = \begin{pmatrix} \nu_{eL} \\ e_L \end{pmatrix} \tag{1.36}$$

and G_e is an arbitrary coupling parameter. Note that this is the Yukawa term for the electron doublet. The muon and tau doublets would have the same form. Then using the unitary gauge version of ϕ we get

$$\mathcal{L}_{Yukawa} = -\frac{G_e}{\sqrt{2}}(v+h)(\bar{e_L}e_R + \bar{e_R}e_L) \tag{1.37}$$

$$= -\frac{G_e v}{\sqrt{2}}(\bar{e}e) - \frac{G_e}{\sqrt{2}}(h\bar{e}e) \tag{1.38}$$

where the electron mass is given by

$$m_e = \frac{G_e v}{\sqrt{2}}. \tag{1.39}$$

Repeating the process for the second and third lepton generations gives the muon and tau masses as

$$m_\mu = \frac{G_\mu v}{\sqrt{2}}, m_\tau = \frac{G_\tau v}{\sqrt{2}} \tag{1.40}$$

Since there are no ν_R fields in the SM, neutrinos are not able to acquire mass the way charged leptons do.

In order to generate quark masses for both the up and down-type quarks it's necessary to use ϕ, which has $Y = 1$, and the conjugate multiplet which is given by

$$\tilde{\phi} = i\tau_2\phi^* = \begin{pmatrix} \phi^{0^*} \\ -\phi^- \end{pmatrix} \tag{1.41}$$

and has Y = -1. The conjugate multiplet then, similar to ϕ, breaks to

$$\tilde{\phi} \rightarrow \begin{pmatrix} v+h \\ 0 \end{pmatrix} \tag{1.42}$$

The Yukawa term for the first generation quarks has the form

$$\mathcal{L}_{Yukawa} = -G_d\bar{q_L}\phi d_R - G_u\bar{q_L}\tilde{\phi}u_R + h.c. \tag{1.43}$$

where G_d and G_u are arbitrary coupling parameters and

$$q_L = \begin{pmatrix} u_L \\ d_L \end{pmatrix}. \tag{1.44}$$

Applying the broken *phi* and $\tilde{\phi}$ gives us

$$\mathcal{L}_{Yukawa} = -(m_d \bar{d}d + m_u \bar{u}u)(1 + \frac{h}{v}) \tag{1.45}$$

where the mass eigenstates are

$$m_q = \frac{G_q v}{\sqrt{2}}. \tag{1.46}$$

It's worth noting that for each of these masses there is an arbitrary coupling parameter (G_q, G_e, G_μ, and G_τ). This means that the values of the fermion masses are not predicted by SM, but these parameters are tuned to reflect observation.

At this point we can summarize the particle content of the SM and their allowed interactions in a way that is seen in Figure 1.2.

1.3 Problems with the SM

Though the SM has proven to be largely successful, there are still some limitations which must be addressed. We can group these two categories. The first of which is phenomena that have been observed experimentally yet are not explained by the SM. The second is the question of why the SM requires a high degree of fine tuning of parameters to properly explain some phenomena.

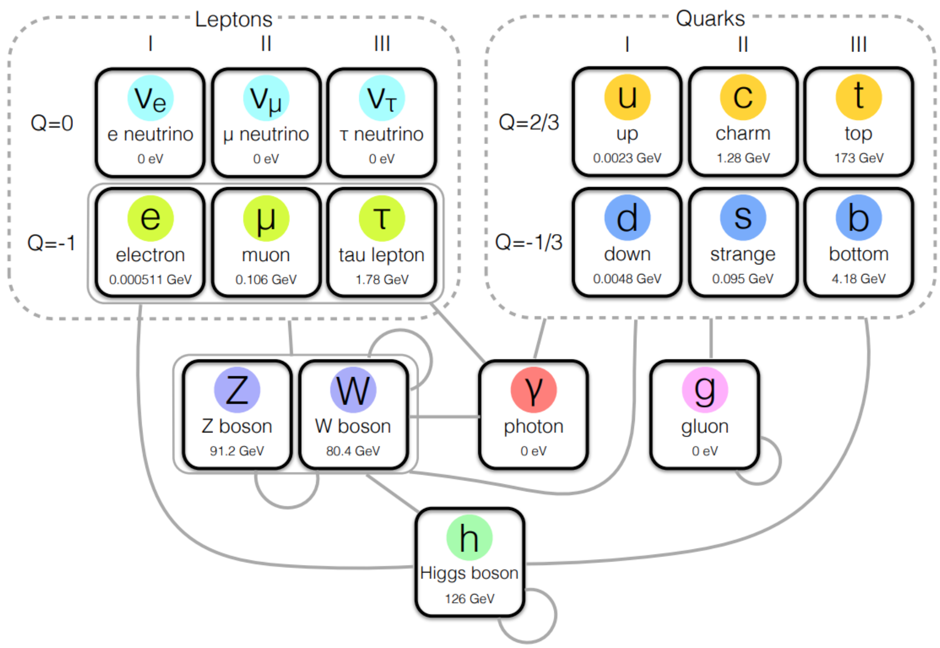

Fig. 1.2: Summary of particle content in the SM. Gray lines connecting groups of particles indicates allowed interactions. Self-coupling is indicated by a gray line connecting a particle to itself. The leptons and quarks are organized in columns corresponding to generation, which is specified at top, and rows corresponding to electric charge Q, which is listed to the left. Each particle's mass is listed beneath its name and symbol. It should be noted that neutrinos in the SM are still treated as massless leptons despite the fact that experimental evidence has established that at least two of the neutrinos are massive. Reprinted from [37]

1.3.1 Missing from the SM

The following is a description of some of the things that are missing from the SM. This list is non-exhaustive but is meant to highlight the need for theories beyond the current scope of the SM in order to get a more complete understanding of all natural phenomena.

Perhaps the most noticeable omission in the SM is a description of the gravitational force. While gravity is well understood over large distances by other means, attempts to construct a quantum theory of gravity have not been successful.

Another issue is the lack of neutrino mass in the SM. Neutrinos are left-handed without right-handed counterparts and therefore do not couple to the Higgs field which leaves them massless. Experimental observations have shown that neutrinos undergo flavor oscillations which is only possible if they are massive. The mechanism by which neutrinos gain their mass cannot be explained in the current framework of the SM.

The inability to explain the evidence of the presence of dark matter in the observable Universe is another shortcoming of the SM. Studies of galactic rotation curves, the cosmic microwave background, and gravitational lensing, for example, indicate that dark matter comprises approximately 30% of the energy density of the Universe is comprised of non-baryonic dark matter[12]. While there are a number of theories proposed that explain the existence of dark matter, there is currently no explanation in the SM.

There are many other problems in addition to those discussed above, such as the hierarchy of masses, the values of the angles in the Cabibbo-Kobayashi-Maskawa matrix (CKM), and the origin of the CP-violating phase in CKM.

1.3.2 Fine tuning

The issue of fine tuning revolves around the fact that there are at least 19 free parameters in the SM that are set by hand to seemingly unrelated and arbitrary values[28]. Having to tune these parameters to have specific values in order to match observations is somewhat unsatisfying in a theoretical sense and begs the questions of whether there is some underlying mechanism that is causing them to take on these particular values. The hierarchy problem is one such fine tuning issue which is related to the observed mass of the Higgs boson, measured to be 125 GeV by the CMS[20] and ATLAS[4] experiments. Its mass receives one-loop quantum corrections from all fermions which can be written as

$$\Delta m_H^2 = -\frac{|\lambda_f|^2}{8\pi^2}\Lambda_{UV}^2 + ... \tag{1.47}$$

where λ_f is the Yukawa coupling and Λ_{UV} is the ultraviolet cutoff which is energy up to which the SM is valid, which is taken to be at the Planck scale (10^{19} GeV). The quadratic dependence of the Higgs mass on Λ_{UV} would make it much larger than the observed value. Counter terms from all orders of perturbation theory would have to be extraordinarily precise and enormous in order to cancel the large corrections and keep the Higgs mass at its observed value.

2. SUPERSYMMETRY

Supersymmetry (SUSY) is an elegant theory that deals with some of the SM issues described in Section 1.3.2. One of the primary motivations of SUSY is to have a symmetric theory that connects fermions to bosons. The SUSY operator Q generates a transformation between boson and fermion states with

$$Q|Boson\rangle = |Fermion\rangle, \tag{2.1}$$

$$Q|Fermion\rangle = |Boson\rangle \tag{2.2}$$

This means that for every SM boson there is a fermion superpartner and vice versa. It's important to note that the spins of the superpartners will differ from their SM counterparts by 1/2, while the other quantum numbers remain unchanged. We now have a remedy for the hierarchy problem if we realize that the one-loop level corrections due to scalars is of the opposite sign for that of fermions and is given by

$$\Delta m_H^2 = \frac{\lambda_s}{16\pi^2}\Lambda_{UV}^2 + ... \tag{2.3}$$

where the coupling in this case is λ_s. We can then cancel the troublesome one-loop corrections if we were to have two complex scalar fields for each

SM fermion and the $\lambda_s = |\lambda_f|^2$.[39]

2.0.1 Minimal Supersymmetric Standar Model (MSSM)

In the SUSY framework the SM particles and their superpartners are arranged in supermultiplets[39]. The SM fermions and their superpartners belong to chiral multiplets. Each of which contains a Weyl fermion and a complex scalar field. In these chiral multiplets, the names for each superpartner is that of its SM counterpart but this an 's' in front of it, i.e. 'selectron', 'stop squark', or more generally 'sleptons' and 'squarks'. The 's' is meant to denote that it is a scalar superpartner. The SM spin-1 gauge bosons and their superpartners belong to gauge supermultiplets. Each of these contains a massless spin-1 boson and a massless Weyl fermion. The Weyl fermions in the gauge supermultiplet are referred to with an 'ino' added as a suffix, i.e. 'wino', 'gluino', or more generally as 'gauginos'. Table 2.1 shows the particles in MSSM and their associated SM particles. After

Tab. 2.1: Summery of SM particles and superpartners

SM particles		Spin	MSSM particles		Spin
Quark	q	1/2	Squark	$\tilde{q}$	0
Lepton	l	1/2	Slepton	$\tilde{l}$	0
Gluon	g	1	Gluino	$\tilde{g}$	1/2
B	B	1	Bino	$\tilde{B}$	1/2
W	W	1	Wino	$\tilde{W}$	1/2
Higgs	H	0	Higgsino	$\tilde{H}$	1/2

electroweak symmetry breaking the neutral gauginos, $\tilde{W}_0$ and $\tilde{B}_0$, and the Higgsino form four mass eigenstates referred to as neutralinos $\tilde{\chi}_0$.

A new quantum number, *R-parity*, is used in the MSSM. One major reason for the introduction and conservation of this new quantum number is to prevent proton decay in the MSSM. It can written as

$$P_R = (-1)^{3\cdot(B-L)+2s} \tag{2.4}$$

where B represents the baryon number, L represents the lepton number, and s gives the spin. All SM particles have $P_R = +1$ and all superpartners have $P_R = -1$. This means that if we conserve R-parity all SUSY particles must will be produced in even number, or in the case of a collider experiment they will be pair produced. Conservation of R-parity also makes the lightest SUSY particle (LSP) completely stable making it a good candidate for dark matter. From the standpoint of a collider experiment, the completely stable LSP will exit the detector without leaving a signal so long as it is electrically neutral. This lack of signal will present in the form of an imbalance in the reconstructed momentum in the transverse plane of the detector. The magnitude of this imbalance is called the missing transverse energy E_T^{miss}.

2.1 Gauge-mediated supersymmetry breaking

Superpartners and their SM counterparts would have the same masses if SUSY were an unbroken symmetry, but since there has yet to be any experimental evidence of SUSY at what should be detectable masses, it must be that SUSY is a broken symmetry. In this analysis we will focus on the model of gauge-mediated supersymmetry breaking (GMSB) in which SUSY is spontaneously broken. In this model the SUSY breaking occurs in a "hidden" sector and then the breaking is communicated to the "visible" sector by messenger particles via SM gauge interactions[39].

The lightest SUSY particle in GMSB is the gravitino $\tilde{G}$, which is the superpartner of the graviton. Since the graviton is a spin-2 particle, this makes the gravitino spin-3/2. The gravitino is significantly lighter than all of the other SUSY particles in this model and since it is only able to interact with SM particles gravitationally, it would leave the detector without depositing any energy. The lightest neutralino is taken to be the next-to-lightest supersymmetric particle (NLSP) and we assume that this promply decays as $\tilde{\chi}_1^0 \to \gamma\tilde{G}$, $\tilde{\chi}_1^0 \to Z\tilde{G}$, or $\tilde{\chi}_1^0 \to H\tilde{G}$ of which the first has a branching ratio of over 90% in most GMSB models[47]. In this analysis we assume a 100% branching ratio for $\tilde{\chi}_1^0 \to \gamma\tilde{G}$.

As strong productions are dominant at a proton-proton collider such as the LHC, the prevailing modes of SUSY production are gluino pair production and squark pair production. These are the modes that we target in this analysis. In particular this analysis looks at two simplified models, T5gg and T6gg. In the T5gg simplified model gluino pairs are produced from the proton-proton collision. The gluinos decay to quark-antiquark pairs and neutralinos. Each neutralino then decays to a photon and a gravitino. In the T6gg simplified model squark pairs are produced which then each decays to a quark or antiquark and a neutralino. The neutralinos then each decay to a photon and a gravitino.

2.2 Current experimental bounds on supersymmetry

At present, there has been no experimental evidence of supersymmetry. The absence of this evidence has allowed for limits to be placed on allowed sparticle production cross sections and masses. Figure 2.1 shows mass regions excluded for different sparticles from various analyses.

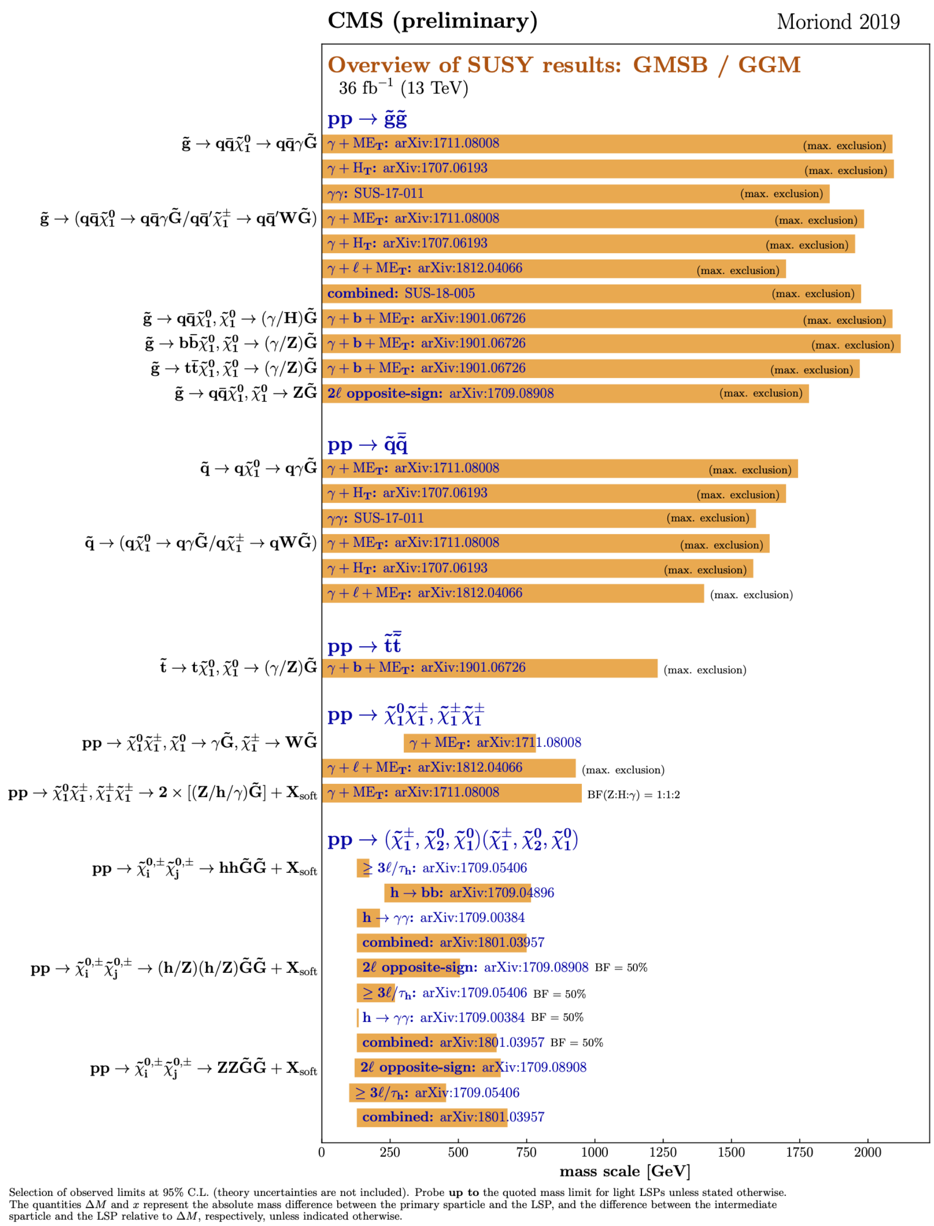

Fig. 2.1: Excluded ranges of sparticle masses from selected CMS results.

3. THE LARGE HADRON COLLIDER

The Large Hadron Collider (LHC) is a 26.7 kilometer-long, two-ring particle accelerator and collider located on the border of France and Switzerland at the European Organization for Nuclear Research (CERN). During normal operations the LHC maintains two counter-rotating beams of proton bunches that collide at four interaction points (IP) with up to $\sqrt{s} = 14$ TeV center of mass energy and a luminosity of $10^{34}\mathrm{cm}^{-2}\mathrm{s}^{-1}$. The ALICE (Point 2), ATLAS (Point 1), CMS (Point 5), and LHC-b experiments each have a detector at one of these interaction points as scene in Figure 3.1 . The CMS and ATLAS are general-purpose detectors while LHC-b specializes in beauty quark studies. ALICE is a heavy-ion experiment which uses $^{208}Pb - p$ or $^{208}Pb -^{208} Pb$ collisions that can also be produced by the LHC.

3.1 Injection Complex

In order to bring the protons from rest up to their target collision energy a series of accelerators, as shown in Figure 3.2, are used. The acceleration sequence begins with the injection of hydrogen gas into a duoplasmatron. Here a bombardment of electrons ionize the hydrogen atoms while an electric field pushes them through the duoplasmatron cavity. The result is 100 keV protons being passed on to a quadrapole magnet which guides them into the aperture of a linear accelerator (LINAC2). The radio frequency (RF) cavities in LINAC2 accelerate the protons up to 50 MeV. At this point the protons are sent into one of four rings in the Proton Synchrotron Booster (PSB). The PSB repeatedly accelerates the protons around a circular path until they reach an energy of 1.4 GeV. The bunches of protons from each PSB ring are then sequentially injected into the single-ringed Proton Synchrotron (PS). Each bunch injected into the PS are captured by one of the "buckets" (Figure 3.3) provided by the PS RF system which also manipulates the bunches into the desired profile and proton density. These proton bunches are accelerated to 25 GeV and injected into the Super Proton Synchrotron (SPS) where they are accelerated to 450 GeV. Finally the proton bunches are injected into the LHC ring where they are accelerated to 6.5 TeV and collided in 25 ns intervals to yield a center of mass energy of $\sqrt{s} = 13$ TeV.

3.2 Tunnel and Magnets

The LHC was designed to produce collisions with up to $\sqrt{s} = 14$ TeV. That requires confining and guiding 7 TeV protons around the circumference of the LHC ring. The ring is housed in a 4 meter-wide underground tunnel that ranges in depth between 45 and 170 meters below the surface. This tunnel was repurposed from the Large Electron-Positron (LEP) Collider which previously occupied the space. For this reason the tunnel is not completely circular but is instead made up of alternating curved and straight sections of 2500 m and 530 m in length respectively. The straight sections, labeled 1-8 in Figure 3.1, are used as either experimental facilities or sites for hardware necessary for LHC operations such as RF cavities for momentum cleaning, quadrupole magnets for beam focusing, and sextupole magnets for acceleration and betatron cleaning.

Steering a 7 TeV proton beam around the curved sections requires a magnetic field of 8.33 Tesla which is provided by 1223 superconducting dipole magnets cooled to 1.9 K. A cross section of the LHC dipole is shown in Figure 3.4. Supercooled liquid helium flows through the heat exchanger pipe to cool the iron yolk to a temperature of 1.9 K. Ultra high vacuum is maintainted in the outer volume to provide a layer of thermal insulation between the inner volume and the outer steel casing. Inside the iron yolk is a twin bore assembly of niobium-titanium superconducting coils. Two parallel beam pipes are located within the focus of the superconducting coils. This is the ultra high vacuum region where the subatomic particles are confined as they travel around the LHC ring.

3.3 Luminosity

The number of events generated per second for specific process having cross-section σ_{event} is given by:

$$\frac{dN_{event}}{dt} = L\sigma_{event} \tag{3.1}$$

where L in the machine luminosity. The machine luminosity for a Gaussian beam distribution can be written in terms of the beam parameters as:

$$L = \frac{N_b^2 n_b f_{rev} \gamma_r}{4\pi\epsilon_n \beta*} F \tag{3.2}$$

where N_b is particle density in each bunch, n_b is the number of bunches in each beam, f_{rev} is the frequency of revolution, and γ_r is the relativistic gamma factor. The variables ϵ_n and $\beta*$ are the normalized transverse beam emittance and the beta function at the IP respectively, while F is the geometric reduction factor depending due to the beams' crossing angle at the IP. [29]

The total number of events produced over a given amount of time would then be

$$N_{event} = \sigma_{event} \int L dt = \sigma_{event} L_{integrated}. \tag{3.3}$$

The integrated luminosity delivered each year to the CMS experiment is shown in 3.5. The analysis presented here uses data collected from the 2016, 2017, and 2018 campaigns which gives a combined integrated luminosity of 158.7 fb^{-1}.

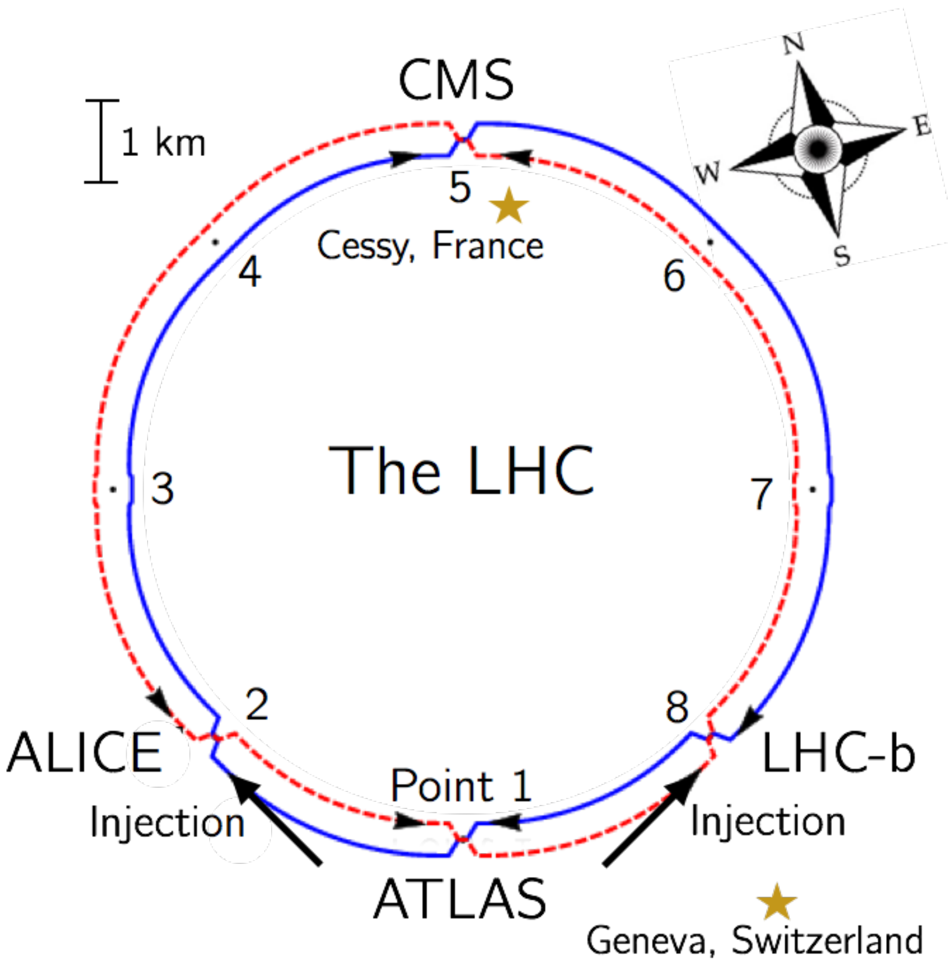

Fig. 3.1: Interaction points of the LHC

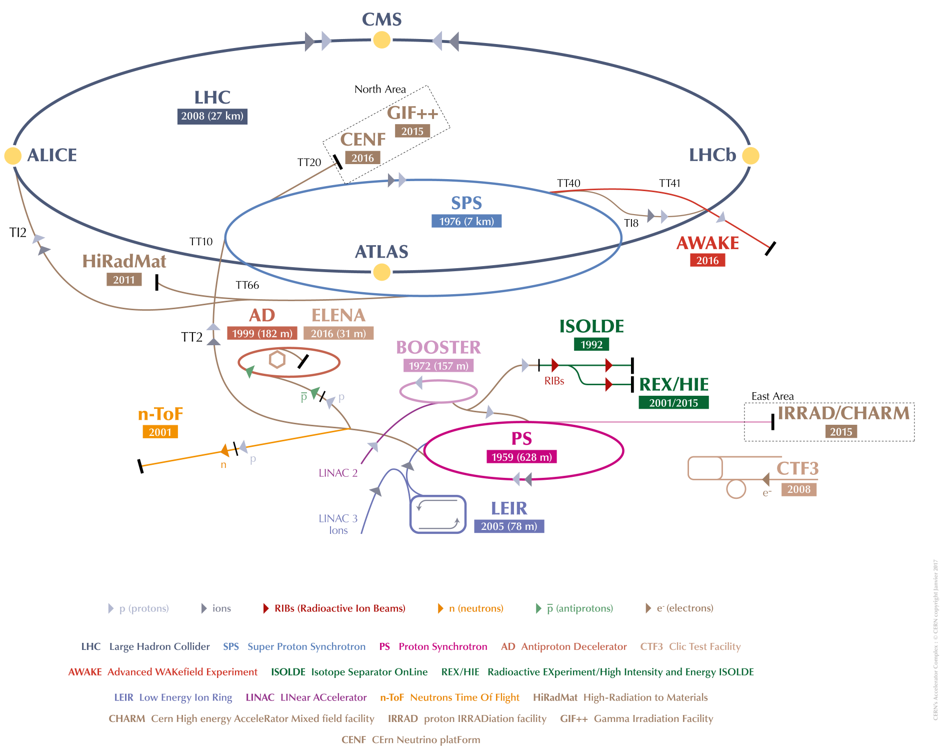

Fig. 3.2: Layout of LHC accelerator complex [29].

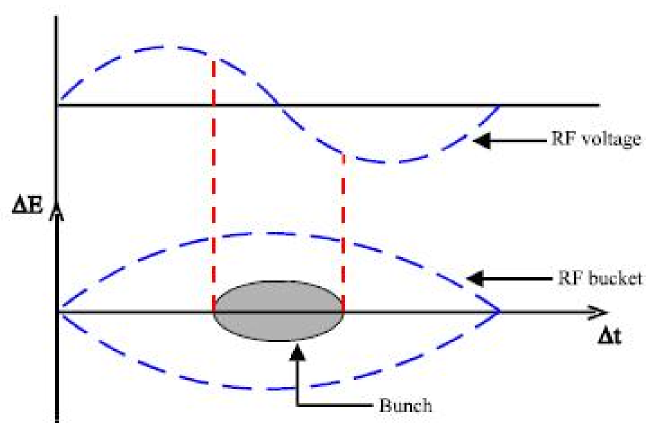

Fig. 3.3: Proton bunch capture onto RF bucket [10].

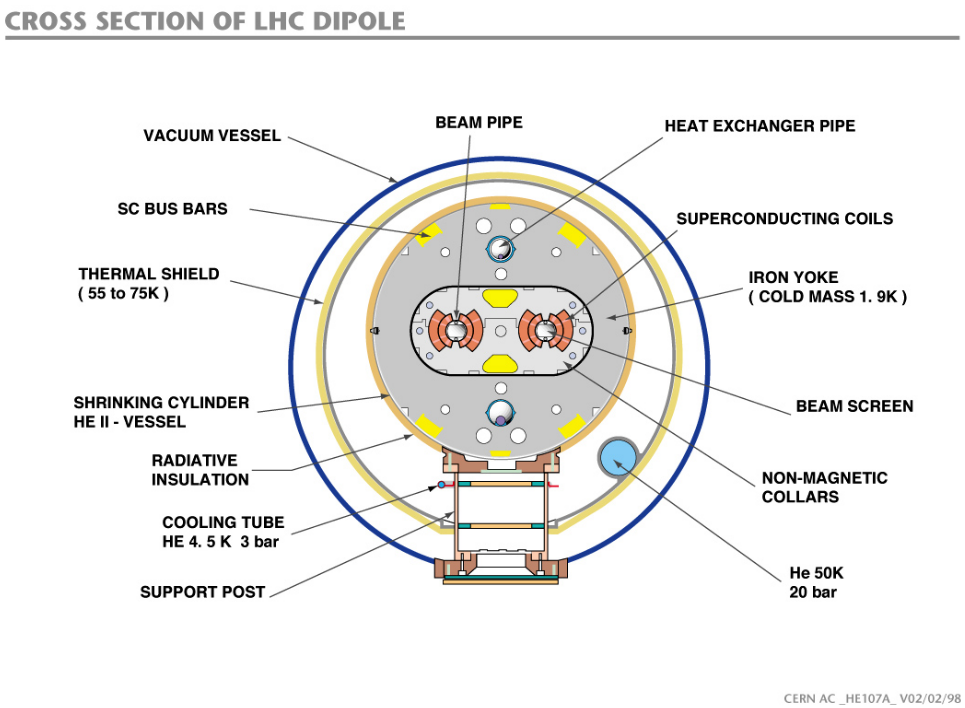

Fig. 3.4: Cross section of LHC dipole [17]

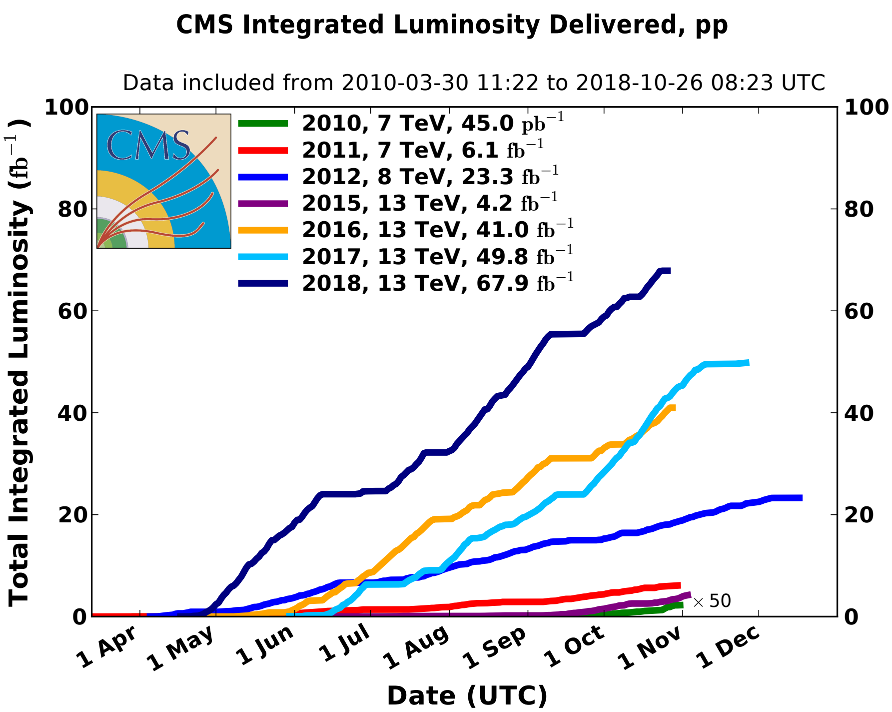

Fig. 3.5: Integrated luminosity delivered by the LHC to the CMS experiment each year from 2010-2018.

4. COMPACT MUON SOLENOID

About 100 meters below the town of Cessy, France at Point 5 is the Compact Muon Solenoid (CMS). The CMS is a general purpose detector weighing 14,000 tonnes with a length of 28.7 meters and a 15.0-meter diameter that was designed to accurately measure the energy and momentum of particles produced in the proton-proton or heavy-ion collisions at the LHC [24]. A perspective view of of the detector is shown in Figure 4.1. In order to get a full picture of what is being produced by the collisions the CMS detector must be able identify the resulting particles as well as accurately measure their energy and momentum. For this reason the detector was designed to be a collection of specialized sub-detectors, each of which contributes data used in the reconstruction of a collision.

At the heart of the CMS detector is a 3.8-Tesla magnetic field produced by a superconducting solenoid. Inside the 6-meter diameter solenoid are three layers of sub-detectors. These make up the inner detector and are, in order from innermost to outermost, the silicon tracker, the electromagnetic calorimeter (ECAL), and the hadronic calorimeter (HCAL). Outside the solenoid is the muon system. A transverse slice of the detector (Figure 4.2) shows the sub-detectors and how different types of particles interact with with them. Table 4.1 shows a summary of which sub-detectors are expected

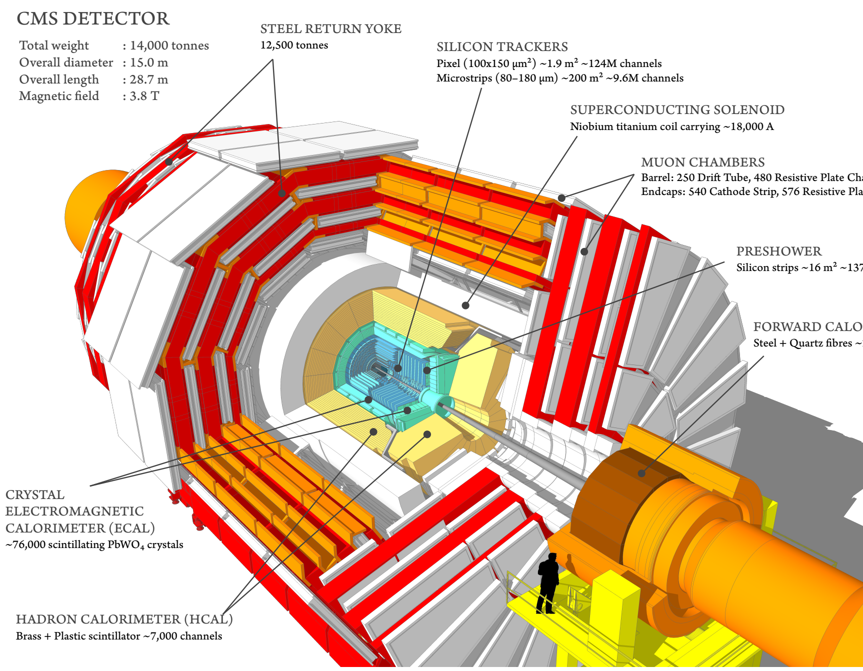

Fig. 4.1: Schematic of CMS detector [42]

to produce signals for different types of particles.

Particle	Tracker	ECAL	HCAL	Muon
Photons	No	Yes	No	No
Electrons	Yes	Yes	No	No
Hadrons (charged)	Yes	Yes	Yes	No
Hadrons (neutral)	No	No	Yes	No
Muons	Yes	Yes	Yes	Yes
Invisible (ν, SUSY, etc)	No	No	No	No

Tab. 4.1: Summary of signals expected for each particle type in each sub-detector.

4.1 Coordinate System

The origin of the coordinate system used by CMS is centered at the nominal collision point in the center of the detector. A right-handed Cartesian system

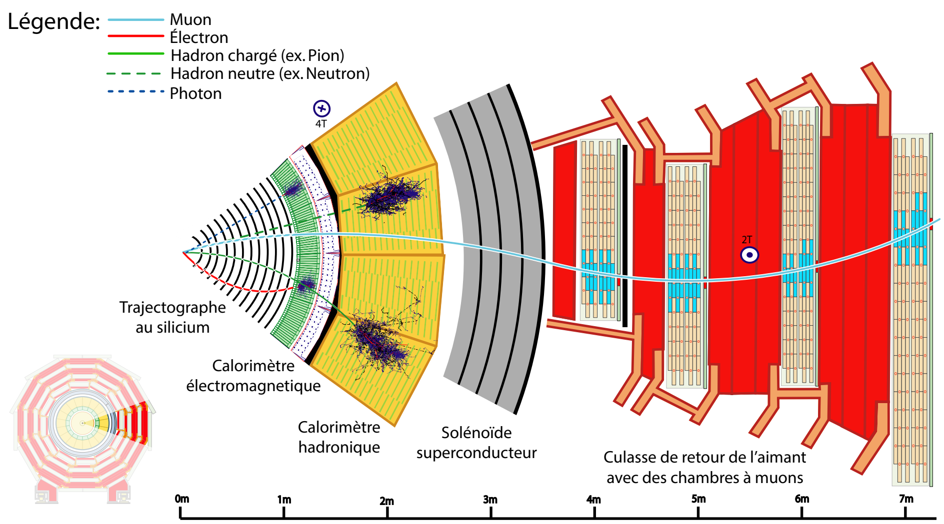

Fig. 4.2: Transverse slice of the CMS detector[11].

is used with the x-axis pointing radially inward toward the center of the LHC ring, y-axis pointing vertically upward, and the z-axis pointing tangent to the LHC ring in the counterclockwise direction as viewed from above. CMS also uses an approximately Lorentz invariant spherical coordinate system spanned by three basis vectors. They are the transverse momentum p_T, pseudorapidity η, and azimuthal angle ϕ. The transverse momentum and azimuthal angle translate to the Cartesian system in the following ways using the x and y-components of the linear momentum:

$$p_T = \sqrt{(p_x)^2 + (p_y)^2} \tag{4.1}$$

$$\phi = tan^{-1}\frac{p_y}{p_x} \tag{4.2}$$

while the pseudorapidity can be translated using the polar angle θ relative the positive z-axis as

$$\eta = -ln[tan\frac{\theta}{2}]. \tag{4.3}$$

4.2 Tracker

The innermost sub-detector in CMS is the silicon tracker. The tracker is used to reconstruct tracks and vertices of charged particles. In order to give precise reconstruction of charged particle trajectories it needs to be position as close as possible to the IP and have high granularity. The close proximity to the IP requires the materials to be tolerant to the high levels of radiation in that region. Being the innermost sub-detector it must also minimally disturb particles as they pass through it into the other sub-detectors. These criteria led to the design of the tracker using silicon semiconductors.

The silicon tracker is made up of two subsystems, an inner pixel detector and an outer strip tracker which are oriented in a cylindrical shape with an overall diameter of 2.4 m and length of 5.6 m centered on the interaction point. Both subsystems consist of barrel and endcap regions which can be seen in Figure 4.3.

4.2.1 Pixel Detector

The pixel detector is the innermost subsystem in the silicon tracker and spans the pseudorapidity range $|\eta| < 2.5$ and is responsible for small impact parameter resolution which is important for accurate reconstruction of secondary vertices [24]. In order to produce these precise measurements a

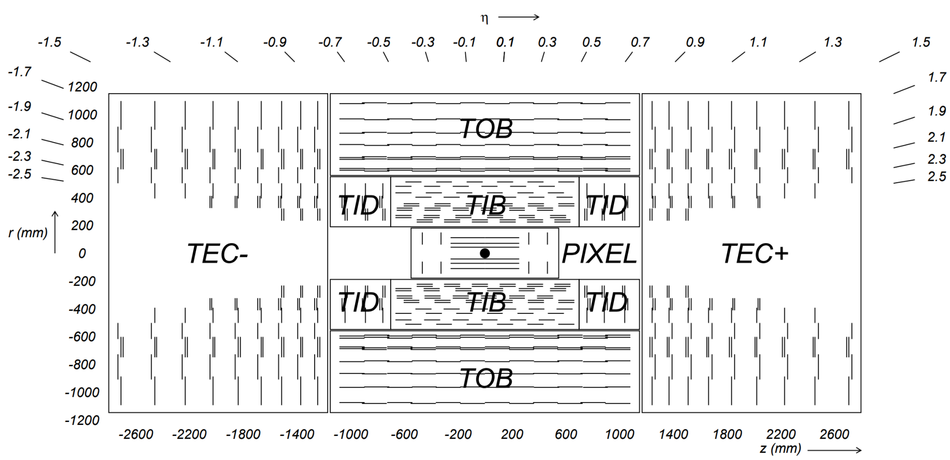

Fig. 4.3: Cross section (side) of CMS tracker prior to the Phase 1 upgrade during the year-end technical stop of 2016/2017. Each line represents a detector module while double lines indicate back-to-back strip modules. Surrounding the pixel tracker (PIXEL) is the strip detector, which is divided into the Tracker Inner Barrel (TIB), Tracker Outer Barrel (TOB), Tracker Inner Disks (TID), and Tracker Endcaps (TEC). Reprinted from Reference [23].

very high granularity is required. In addition to this the proximity to the IP means that one expects there to be high occupancy of the tracker. These constraints are met by using pixels with a cell size of 100 x 150 μm^2.

The original pixel detector was designed for operation at the nominal instantaneous luminosity of 10^{34} cm^{-2}s^{-1} with 25 ns between proton bunch crossings, resulting in on average about 25 proton-proton interactions occurring per bunch crossing or pileup [23]. During the LHC technical shutdown of 2016/17, the pixel detector underwent the scheduled Phase 1 upgrade which would allow operation at higher levels of instantaneous luminosity and pileup. Figure 4.4 shows a cross sectional view in the r-z plane. Prior to 2017 there were three barrel layers and two endcap layers on each side which provide three very precise space points for each charged particle. The upgrade decreased the radius of the innermost barrel layer from 4.4 cm to 3.0 cm and added a fourth barrel layer as well as adding third endcap layer to each side. Each of the endcap layers consisted of two half-disks populated with pixel modules whereas the upgraded endcap layers were split into inner and outer rings. [22]

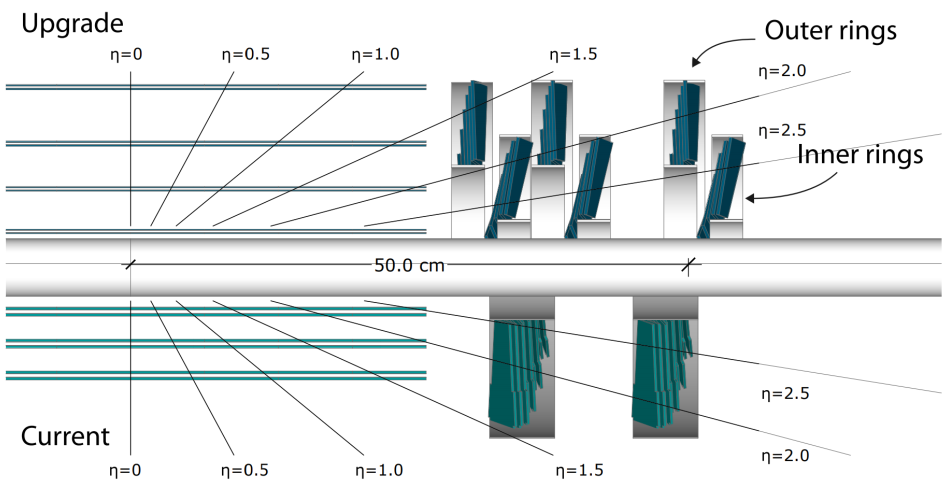

Fig. 4.4: Cross section (side) of pixel detector. The lower half , labeled "Current", shows the design prior to 2017 while the upper half, labeled "Upgrade", shows the design after the upgrade. Reprinted from Resource [22]

4.2.2 Strip Detector

The silicon strip detector surrounds the pixel detector and is comprised of four subsystems, the Tracker Inner Barrel (TIB), the Tracker Outer Barrel (TOB), the Tracker Inner Disks (TID), and the Tracker Endcaps (TEC), all of which can be seen in Figure 4.3 [24]. The TIB and TID both use 320 μm thick silicon micro-strip sensors oriented along z and r respectively. The TIB has four layers while the TID is composed of three layers. This geometry allows the TIB and TID to combine to provide up to four $r - \phi$ measurements on charged particle trajectories.

Surrounding the TIB and TID is the TOB, which extends between $z = \pm 118$ cm. This subsystem consists of six layers of 500 μm thick silicon micro-strip sensors with strip pitches ranging from 122 μm to 183 μm, providing six more $r-\phi$ measurements in addition to those from the TIB/TID subsystems. Beyond the z range of the TOB is the TEC. Each TEC is made up of nine disks. Each of the nine disks has up to seven concentric rings of micro-strip sensors oriented in radial strips with those on the inner four rings being 320 μm thick and the rest being 500 μm thick, providing up to nine ϕ measurements for the trajectory of a charged particle.

To provide additional measurements of the z coordinate in the barrel and r coordinate in the disks a second micro-strip detector module is mounted back-to-back with stereo angle 100 mrad in the first two layers of the TIB and TOB, the first two rings of the TID, and rings 1, 2, and 5 of the TEC. The resulting single point resolution is 230 μm in the TIB and 530 μm in the TOB. The layout of these subsystems ensures at least nine hits for $|\eta| < 2.4$ with at least four of hits yielding a 2D measurement.

4.3 Electromagnetic Calorimeter

The electromagnetic calorimeter (ECAL) lies just outside the tracker and is a hermetic homogeneous calorimeter designed to measure the energy deposited by electrons and photons. It consists of a central barrel (EB) with 61200 lead tungstate ($PbWO_4$) crystals which is closed by two endcaps (EE), each having 7324 crystals. Highly-relativistic charged particles passing through a crystal primarily lose energy by producing bremsstrahlung photons. Photons lose energy by producing $e^- - e^+$ pairs. In front of each EE is a preshower (ES) detector which acts as a two-layered sampling calorimeter. The crystals in the EB are instrumented with avalanche photodiodes (APDs) while the EE crystals are instrumented with vacuum phototriodes (VPTs). The ECAL design was strongly driven to be sensitive to the di-photon decay channel of the Higgs boson. This led to the design of a calorimeter that was fast, radiation-hard, and had good spatial and energy resolution.

4.3.1 Crystals

In order to provide a good spacial resolution it was necessary for the ECAL to have a fine granularity. The small Moliere radius (22 mm) and short radiation length (8.9 mm) of $PbWO_4$ allows for fine granularity while maintaining good energy resolution by containing nearly all of the energy from an EM shower without the need for a restrictively thick crystal layer. The $PbWO_4$ scintillation is also fast enough that approximately 80 percent of an EM shower is produced within 25 ns, which is the also the amount of time between bunch crossings at the LHC. These crystals have a Gaussian-shaped spectrum spanning from 360 nm to 570 nm with a maximum at approximately 440 nm. While $PbWO_4$ is relatively radiation-hard, the amount of ionizing radiation seen by the crystal leading up to the HL-LHC era of operations causes wavelength-dependent degradation in light transmission. The scintillation mechanism however is unchanged so this damage can be tracked and accounted for by injecting laser light near the peak wavelength of the emission spectrum into the crystals to monitor optical transparency.

Light produced in the crystal is transmitted along its length and collected at the rear by either an APD in the EB or a VPT in one of the EE. Light output is temperature dependent so the crystals are kept at 18°C at which the yield is about 4.5 photoelectrons per MeV. The EB and EB crystals, which have a truncated pyramidal shape to match the lateral development of the shower, along with their photosensors are shown in Figure 4.5.

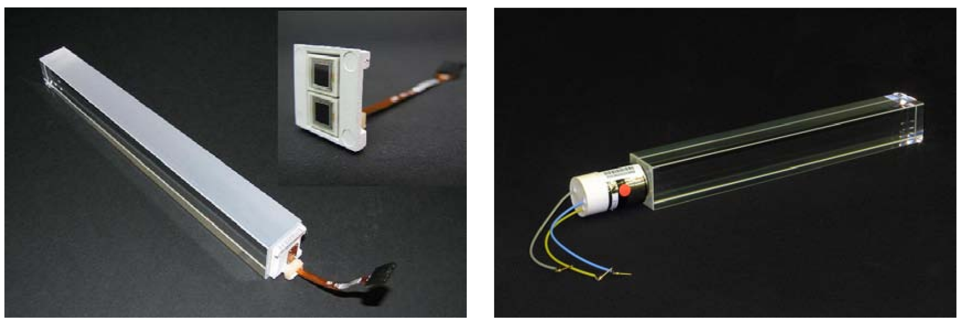

Fig. 4.5: $PbWO_4$ crystals. Left: EB crystal with APD. Right: EE crystal with VPT. Reprinted from [24]

4.3.2 Barrel and Endcaps

The EB covers the pseudorapidity range $|\eta| < 1.479$ and uses crystals that are 230 mm long, which corresponds to 25.8 radiation lengths. The front face of each crystal measures 22×22 mm^2 while the rear face measures 26×26 mm^2. These are grouped in 36 supermodules (SM), each comprised of 1700 crystals arranged in a 20×85 grid in $\phi \times \eta$. Each SM spans half the length of the barrel and covers 20° in ϕ. On the back face of each crystal is a pair of APDs (semiconductor diodes). APDs are compact, immune to the longitudinal 3.8 T magnetic field produced by the solenoid at this location, and resistant to the radiation levels expected in the EB over a ten year period. They also have high enough gain to counter to low light yield of the crystals. All of this makes them an ideal choice for use in the EB. Each APD has an active area of 5×5 mm^2 and are operated at a gain of 50 which requires a bias voltage between 340 and 430 V. As the gain of the APDs is highly dependent on the applied bias voltage and any gain instability would translate to degradation in energy resolution, very stable power supplies are used to maintain voltages within a few tens of mV.

The EE cover the pseudorapidity range $1.497 < |\eta| < 3.0$. The crystals in the EE have a 28.62×28.62 mm^2 front face cross section and 30×30 mm^2 rear face cross section. Each crystal is 220 mm long which corresponds to 24.7 radiation lengths and are grouped in 5×5 units called supercrystals (SCs). Two halves, called *Dees*, make up each EE. Each Dee contains 138 SCs and 18 partial SCs which lie along the inner and outer circumference. On the back of each crystal in EE is a VPT which is a conventional photomultiplier with a single gain stage. While not as compact as the APDs used in the EB, the VPTs are a more suitable for the more hostile environment at higher η. Each VPT has a 25-mm diameter and approximately 280 mm^2 of active area. Though the VPT gain and quantum efficiency are lower than that of the APDs this is offset by the larger active area allowing for better light collection. Figure 4.6 shows the orientation of the crystals, modules, and supermodules within the ECAL. [24]

4.3.3 Preshower layer

In front of each EE is a preshower (ES) detector. The main purpose of the ES is to identify photons resulting from $\pi^0 \to \gamma\gamma$ within the pseudorapidity range $1.653 < |\eta| < 2.6$, but it also aids in the identification of electrons against minimum ionizing particles (MIPs) and provides a spacial resolution of 2 mm compared to the 3 mm resolution of the EB and EE. The ES acts as a two-layered sampling calorimeter. Lead radiators make up the first layer. These initiate electromagnetic showers from incoming electrons or photons. The deposited energy and transverse profiles of these showers are then measured by the silicon strip sensors which make up the second layer.

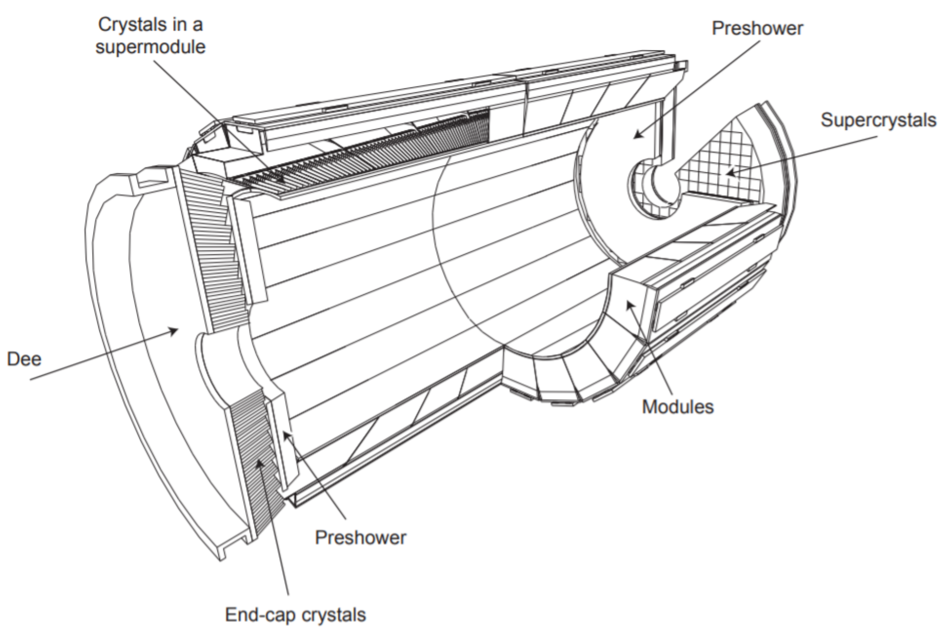

Fig. 4.6: Schematic of ECAL. Reprint from [24]

4.3.4 Performance

The energy resolution of the ECAL can be parameterized as

$$\frac{\sigma}{E} = \frac{S}{\sqrt{E}} \oplus \frac{N}{E} \oplus C \tag{4.4}$$

where S is the stochastic term characterizing the size of photostatistical fluctuations, N is the term characterizing the contributions of electronic, digital, and pileup noise, and C is a constant which accounts for crystal performance non-uniformity, intercalibration errors, and leakage of energy from the back of a crystal. The values for these terms, as measured in a beam test using 20 to 250 GeV electrons, are $S = 0.028$ GeV$^{1/2}$, $N = 0.12$ GeV, and $C = 0.003$. [24]

4.4 Hadronic Calorimeter

In the space between the bore of the superconducting magnet and the ECAL is the Hadronic Calorimeter (HCAL) [2]. The HCAL is a sampling calorimeter used for the measurement of hadronic jets and apparent missing transverse energy resulting from neutrinos or exotic particles. It is made up of alternating layers of plastic scintillator tiles and brass absorbers. EM showers are generated by charged/neutral hadrons in the brass absorber. Charged particles in the shower then produce scintillation light in the plastic scintillator. Wavelength-shifting optical fibers embedded in the scintillator collect and guide the scintillation light to pixelated hybrid photodiodes. A longitudinal cross-section view in Figure 4.7 shows the geometric layout of the

HCAL's barrel (HB), outer barrel (HO), endcap (HE), and forward (HF) sections. The HB is comprised of 17 scintillator layers extending from 1.77 to 1.95 m and covers the pseudorapidity range of $|\eta| < 1.4$. The HO lies outside the solenoid and is composed of only scintillating material. This increases the interaction depth of the calorimeter system to a minimum of $11\lambda_I$ for $|\eta| < 1.26$ and thus reduces energy leakage. Also located inside the solenoid are the two HE which cover pseudorapidities $1.3 < |\eta| < 3.0$ and provide a thickness of $10\lambda_I$. In the forward region is the HF. This is located 11.2 m away from the IP and covers the $2.9 < |\eta| < 5.2$. As the HF is exposed to the highest levels of particle flux, it uses quartz fibers embedded in steel absorbers rather than the materials used in the other parts of the HCAL. Showers initiated by the absorbers produce Cerenkov light in the quartz which transmits along to the fibers to photomultiplier tubes (PMTs).

The HCAL inherently has lower energy resolution than the ECAL. A large portion of the energy from hadronic showers is deposited in the absorbers and never makes it to the scintillation material. There are also the possibilities that showers can be initiated prior to the particles reaching HCAL or a charged particle could deposit energy in the ECAL through bremsstrahlung. The combined energy resolution of the ECAL and the HCAL barrels can be parameterized as

$$\frac{\sigma}{E} = \frac{S}{\sqrt{E}} \oplus C, \tag{4.5}$$

where E is the energy of the incident particle. Theses quantities were measured in a beam test using 2 to 350 GeV/c hadrons, electrons, and muons. The stochastic term is $S = 0.847$ GeV$^{1/2}$, and the constant term is $C = 0.074$ [6].

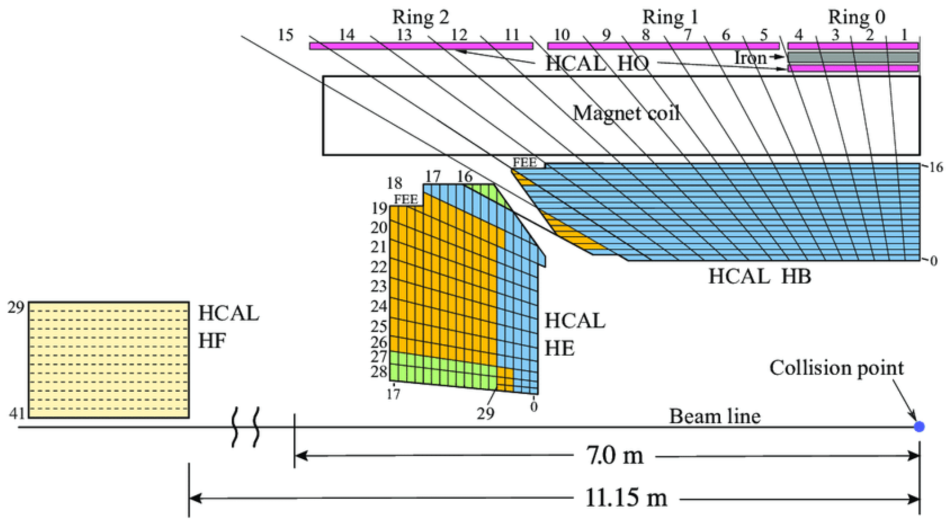

Fig. 4.7: Longitudinal view of HCAL [2]

4.5 Superconducting Solenoid

In between the HCAL barrel and outer barrel is the superconducting solenoid magnet. The magnet is 12 m long with a 6-m inner diameter and provides the bending power necessary to precisely measure the momentum of charged particles. While it is capable of producing a 4 T magnetic field, the magnet is typically operated at 3.8 T. This is done to prolong the lifetime of the magnet. The Niobium Titanium coils used to create the uniform 3.8-T magnetic field are suspended in a vacuum cryostat and cooled by liquid helium to a temperature of 4.5 K. The magnet has a stored energy or 2.6 GJ when operating at full current. There are five wheels in the barrel and three disks on each endcap that make up a 12,000 ton steel yoke which serves to return the magnetic flux. This, along with a mapping of the calculated field strength, can be seen in Figure 4.8. More details on the superconducting solenoid magnet can be found at [1]

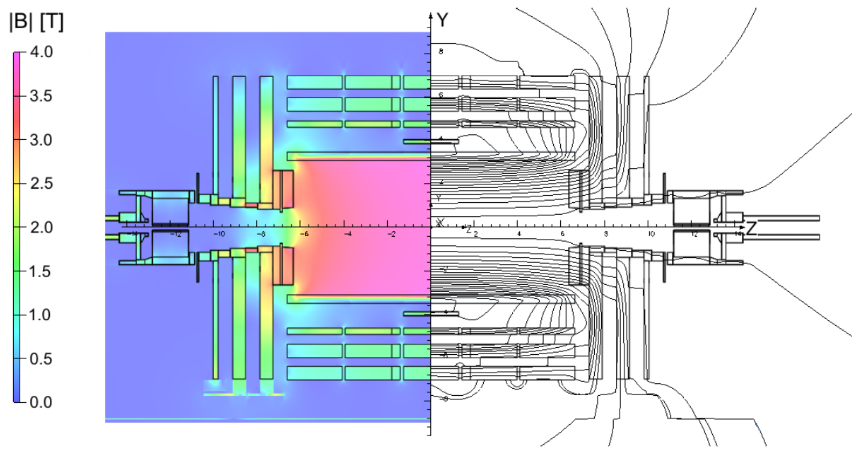

Fig. 4.8: Longitudinal slice of CMS detector while operating at 3.8-T central magnetic field. The right-hand side of the figure shows a mapping of the magnetic field lines while the left-hand side shows a mapping of the field strength. Reprint from [19]

4.6 Muon System

Embedded in magnet return yoke and encapsulating all of the other subdetectors is the muon system. The muon system is the outermost layer because muons don't interact via the strong force and electromagnetic interactions alone are not enough stop them due to their large mass, therefore the only particles that are capable of making it to the muon system are muons and weakly-interacting particles such as neutrinos. The muon sys-

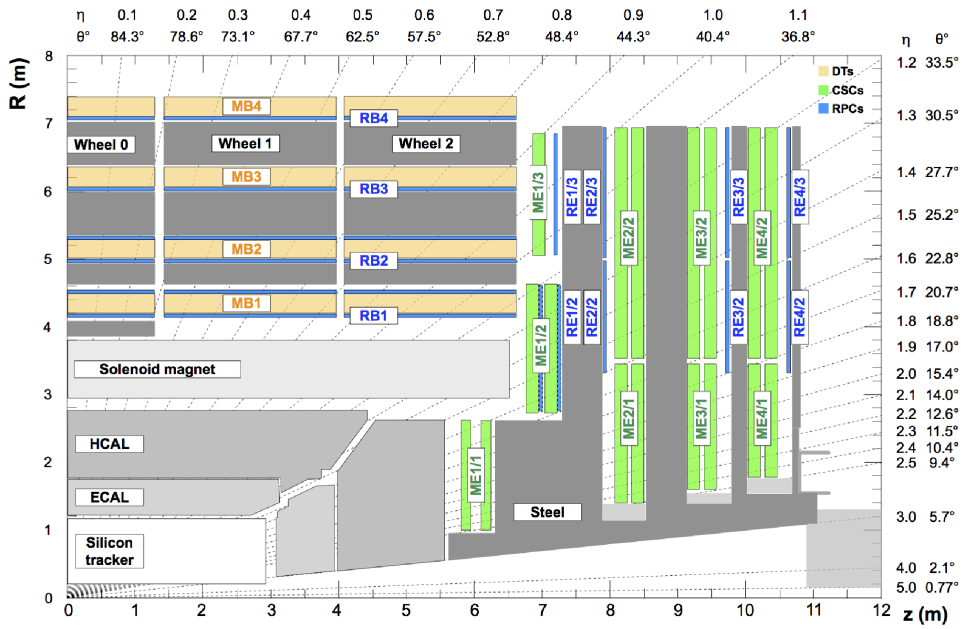

Fig. 4.9: Cross-section of one quadrant of the CMS detector. The DTs are labeled as ”MB” (Muon Barrel) and the CSCs are labeled as ”ME” (Muon Endcap). The RPCs are ”RB” for those in the barrel and ”RE” for those in the endcap. Reprint from [45].

tem is comprised of three different types of detectors. These are drift tube (DT) chambers, cathode strip chambers (CSC), and resistive plate chambers (RPC). A cross-sectional view of the muon system along with the rest of the CMS detector is shown in Figure 4.9.

The DT chambers are used barrel region for $|\eta| < 1.2$. Each chamber is comprised of three superlayers which are made up of four staggered layers of rectangular drift cells. Each of these drift cells contains a mixture of Ar and CO_2 gases. An anode wire, located at the center of each tube, is made of gold-plated stainless steel and is held at 3.6 kV. The gas is ionized when a charged particle passes through and the resulting free electrons are attracted to the anode wire. As these electrons pass through the gas they cause further ionization which results in an electron avalanche. The layers of drift cells are oriented in such a way that two of the three superlayers give the muon position in the ϕ-direction and one gives the position in the z-direction. The result is a spacial resolution of 77-123 μm along the ϕ direction and 133-193 μm along the z direction for each DT chamber [25].

On the endcaps, covering the pseudorapidity range of $0.9 < |\eta| < 2.4$, are the CSCs. In this region there is a higher muon flux as well non-uniform magnetic fields so this portion of the muon system must have higher granularity provided by the CSCs. Each of these chambers contain panels that divide it into six staggered layers. The cathode strips are oriented along the r-direction to give position measurements in the ϕ-direction while anode wires run perpendicular in between the panels to give r-direction position measurements. The spacial resolution provided by the CSCs is 45-143 μm [45].

Both the endcap and barrel regions, spanning $|\eta| < 1.6$, contain RPCs to provide more precise timing measurements. Each RPC is a gaseous parallel-plate detector. High voltage is applied to two large plates which have a layer of gas between them. Outside the chamber is an array of cathode strips which is used to detect electron cascades resulting from muons passing through and ionizing the gas. Where the DTs and CSCs provide precise position information, the RPCs have a very fast response time which gives a time resolution better than 3 ns [45]. This allows for the RPCs to be used as a dedicated muon trigger that can insure each muon is assigned to the correct bunch crossing.

5. CMS TRIGGER SYSTEM

When operating at nominal luminosity the LHC produces over 1 billion proton-proton collisions per second. Finite computing speed and storage capacity limit the rate at which CMS can record events to be about 1 kHz [16]. Decreasing the rate from 1 GHz to 1 kHz is accomplished by using a two-level trigger system to quickly decide which events will be discarded and which will be recorded. The first stage is a hardware-based Level 1 (L1) trigger and the second stage is software-based High Level Trigger (HLT).

5.1 L1 trigger

The L1 trigger decreases the rate by about six orders of magnitude from 1 GHz to 100 kHz by performing rough calculations on information from the ECAL, HCAL, and muon subsystems using field-programmable gate arrays (FPGAs). The L1 trigger can be divided further into the calorimeter and muon triggers. The schematic of the L1 trigger system in Figure 5.1 shows both the calorimeter and muon triggers. The calorimeter trigger trigger uses information from the ECAL and HCAL subdetectors to construct photon, electron, and jet candidates in addition to quantities such as missing transverse momentum and total hadronic activity. The muon trigger uses information from all three muon subsystems to construct muon candidates.

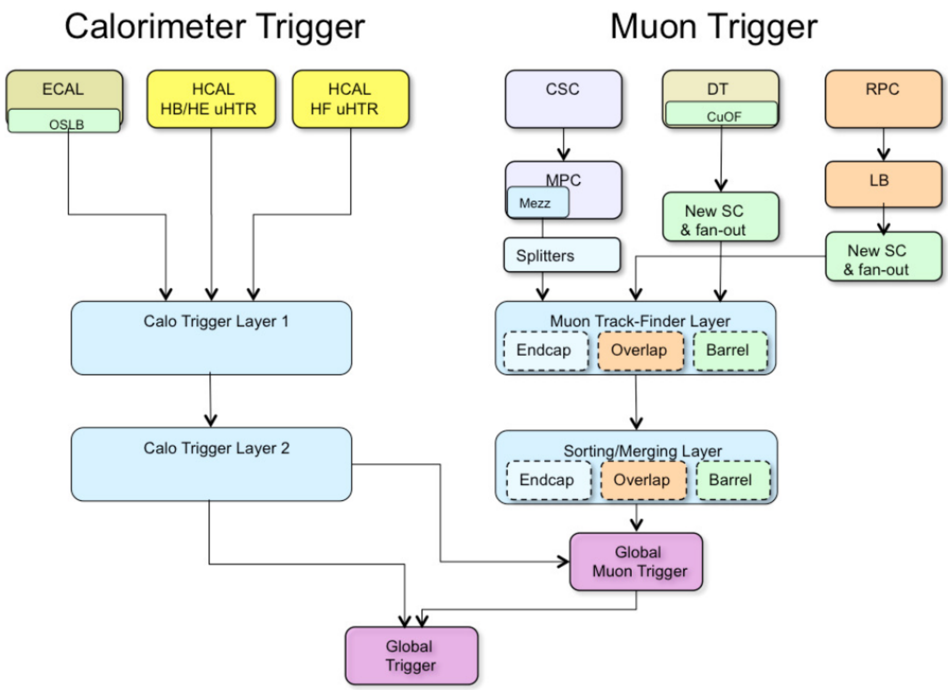

Fig. 5.1: L1 trigger system. Reprint from [3]

The outputs from the calorimeter and muon triggers goes into the Global Trigger (GT) which decides which events should be recorded and which are to be discarded [49].

5.1.1 Calorimeter trigger

Trigger Primitives (TP) are the raw inputs from the ECAL and HCAL for the calorimeter trigger. The TP, which contain information regarding the energy deposits in the calorimeters, are passed to the first layer of the calorimeter trigger. This first layer consists of several FPGA cards that receive data from several bunch crossings, but are each mapped to a section of the detector. This data is then passed on to the second layer in such a way that each FPGA in this layer will receive data for the entire calorimeter for each bunch crossing. Candidate objects are then constructed and organized into a sorted list according to transverse momentum and passed on to the GT and the global muon trigger.

5.1.2 Muon trigger

TP for the muon trigger come from the three muon detectors, the CSCs, DTs, and RPCs. These are then passed on to the first layer of the muon trigger (Muon Track-Finding Layer) where the TP are combined to reconstruct muon tracks for sections of ϕ for different regions of $|\eta|$. The barrel track-finder for $|\eta| < 0.83$, the endcap track-finder for $|\eta| > 1.24$, and the overlap track-finder for $0.83 < |\eta| < 1.24$. This data is passed on to the second layer where the sections of ϕ are merged and subsequently passed on to the global muon trigger where it is combined with the output from Calo Trigger Layer 2 to compute isolation. The global muon trigger then combines the η regions and passes a list of the top eight muon candidates to the GT.

5.1.3 Global Trigger

Final processing of the reconstructed objects and quantities constructed by the calorimeter and muon triggers is carried out by the GT. L1 algorithms or ”seeds” are implemented by the GT using these objects. A full set of L1 seed is called a L1 menu and can be adjusted to meet the requirements of the CMS physics program. Each L1 seed can be given a ”prescale”, which is an integer value N that can be used to reduce the rate of a particular trigger path. This is done by only applying the trigger to one out of N events and can be used to take advantage of the current LHC running conditions.

5.2 High Level Trigger

Events that are accepted by the L1 trigger are passed on to the HLT which is based in software and is therefor capable of analyzing events with a higher degree of sophistication. The HLT has access to information from the full detector and implements ”paths” to select events of interest from those passing the L1 trigger. Each HLT path is a set of criteria that is used to either accept or reject an event. The full set of HLT paths is the HLT menu. Each HLT path is ”seeded” by one or more L1 seeds in order to decrease computing time. That means that a given HLT path will only be processed if the L1 bits associated with its seed or seeds fire. Each HLT path is assigned to a primary dataset depending on its general physics signature. In the case of this analysis, the primary dataset used for signal events was DoubleEG for years 2016 and 2017. This was merged into the EGamma dataset for 2018. A list of the primary HLT used for each year along with its associated primary dataset is listed in Table 5.1. The HLT path for 2016 is different because HLT_DoublePhoton70 was not a part of the HLT menu until 2017.

Tab. 5.1: Primary HLT

Year	HLT path	Primary dataset
2016	HLT_DoublePhoton60	DoubleEG
2017	HLT_DoublePhoton70	DoubleEG
2018	HLT_DoublePhoton70	EGamma

6. CMS PARTICLE AND EVENT RECONSTRUCTION

After an event is chosen to be stored by the trigger system, the output from all of the sub-detectors is saved and recorded to disk as ”RAW” data. These data contain information about the response of each sub-detector, such as tracker hits and energy deposition in the calorimeters. As was mentioned in Chapter 4, shown in Table 4.1 and Figure 4.2, the CMS was designed such that each type of particle resulting from the *pp* collisions at the IP would leave a distinct signature in the sub-detectors. This allows for the information to be reconstructed into lists of physics object candidates such as photons, electrons, muons, etc and quantities such as missing transverse momentum. The particle flow (PF) algorithm performs this reconstruction by first building tracks and calorimeter clusters. These two elements are the inputs to the reconstruction of the aforementioned physics object candidates using a ”link” algorithm.

6.1 Tracks

A combinatorial track finder algorithm based on the Kalman filtering technique uses the hits in the silicon tracker to reconstruct tracks of charged particles [30]. Each iteration of the algorithm is comprised of three steps:

- Seed generation: Find a seed consisting of two to three hits that is compatible with a track from a charged particle.

- Track finding: Use pattern recognition to identify any hits that are compatible with the trajectory implied by the seed generated in the first step.

- Track fitting: Determine the properties of the track, such as origin, trajectory, and transverse momentum by performing a global χ^2 fit.

The first iteration uses stringent requirements on the seeds and the χ^2 of the track fit to pick out isolated jets which have very high purity. The hits associated with these high purity tracks are then removed to reduce the combinatorial complexity for subsequent iterations. This allows successive iterations to identify less obvious tracks by progressively loosening criteria while the removal of previously associated hits mitigates the likelihood of fake tracks being built.

6.2 Calorimeter clusters

Calorimeter clusters are constructed using energy deposition information from the calorimeters. Clusters are formed by first identifying the seed cell (ECAL crystal or HCAL scintillating tile) that corresponds to the local maxima of an energy deposit that is above a given threshold. Neighboring cells are then aggregated to grow topological clusters if their signals are above twice the standard deviation of the level of electronic noise.

6.3 Object identification

At this point the tracks and calorimeter clusters are linked to form a PF block. This linkage is done with an algorithm that quantifies the likelihood that a given track and cluster were results of the same particle. As PF blocks are identified as object candidates they are removed from the collection prior to each subsequent iteration until all tracks and clusters have been assigned to a PF object candidate. The following sections will outline how each of these PF objects is identified.

6.3.1 Muons

Muons are the easiest particle to identify, so they are the first objects reconstructed in the CMS. PF Muons are classified in three categories depending on how their tracks are reconstructed:

- Tracker muons: Tracks reconstructed from the inner tracker having $p_T > 0.5$ GeV and $|\vec{p}| > 2.5$ GeV that, when propagated to the muon system, match at least one hit in the muon chambers.
- Stand-alone muons: Tracks reconstructed only using hits in the muon system.
- Global muons: Stand-alone muons that coincide with a track from the inner tracker.

After a muon is reconstructed it is given an identification or ID based on observables such as the χ^2 of the track fit, how many hits were recorded per track, or how well the tracker and stand-alone tracks matched. These

IDs represent different working points (loose, medium, and tight) which correspond to increasing purity but decreasing efficiency as you move from loose toward tight.

6.3.2 Electrons

The next objects reconstructed in the CMS are electrons. Bremsstrahlung in the tracker layers causes substantial energy loss and changes in momentum which requires the use of a dedicated tracking algorithm. In place of the Kalman filtering technique, a Gausian-sum filter (GSF) algorithm is used. This algorithm uses a weighted sum of Gaussian PDFs which does a better job of modeling the Bremsstrahlung effects than the Kalman filtering technique which uses a single Gaussian PDF.

PF ECAL clusters are regrouped by identifying a seed cluster then associating and adding clusters from Bremsstrahlung photons to form superclusters. The schematic in Figure 6.1 shows how the Bremsstrahlung photons are emitted in directions tangent to the trajectory of the electron. Electrons bending in the magnetic field causes spreading of PF ECAL clusters to typically occur along the ϕ-direction. Two approaches are used to associate the superclusters to GSF tracks. One is the ECAL-driven method, which uses superclusters with $p_T > 4$ GeV as seeds for the GSF track finding algorithm. This works well for high-p_T isolated electrons because the bend radius is less severe which decreases the spread of the PF ECAL clusters. This results in more of the Bremsstrahlung radiation being recovered and correctly assoiated with an electron candidate. The second approach is the tracker-driven method which uses tracks with $p_T > 2$ GeV as seeds that are propagated out to the surface of the ECAL and used for clustering. This method works best with soft electrons like those in jets because it relies on the high granularity of the tracker to disentangle overlapping energy deposits in the ECAL. [41]

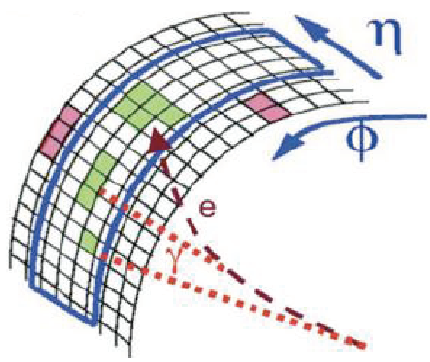

Fig. 6.1: The Bremsstrahlung photons continue along a straight trajectory while the electron path is bent by the magnetic field. This results in energy deposited in the calorimeter for such electrons to be spread out along the ϕ-direction.

As a final step, a boosted decision tree (BDT) is used to discriminate between real and fake electrons. The BDT is given variables associated with track-cluster matching, shower shape, and tracking. The output score of the BDT is used to classify electrons into loose, medium, and tight working points which exhibit to the same purity and efficiency trends as the muon working points.

6.3.3 Photons

Unlike electrons, photons typically deposit most of their energy in the ECAL without interacting with the tracker therefore their reconstruction is seeded from ECAL superclusters that do not have any GSF tracks associated with them. When photons interact with the tracker material they convert into electron-positron pairs which follow bent trajectories due to the magnetic field prior to entering the ECAL. This causes a spread of the energy deposition along the ϕ-direction. The goal of the clustering algorithm for photon reconstruction is to include all of the energy deposits of electrons resulting from photon conversions. As with the calorimeter clustering algorithm, the photon clustering starts by identifying a local energy maxima as a seed crystal. In the EB a cluster is made up of several parallel strips of crystals 5×1 in $\eta \times \phi$. The first strip has the seed crystal at its center. Neighboring strips in the ϕ-direction are added if they have energy above a threshold of 10 GeV but less than that of the subsequent strip with a maximum of 17 strips in a cluster. In the EE, the seed cluster is 5×5 with adjacent 5×5 clusters being added if they meet the minimum energy requirement.

Converted and unconverted photons can be differentiated by looking at how the energy is distributed in a supercluster. The variable R_9 is used for this purpose. It is defined as the ratio of the energy in a 3×3 crystal array to the energy in the entire supercluster. As the energy deposits resulting from converted electrons is more spread out they result in a lower R_9 value than unconverted photons. A photon is candidate is considered to be unconverted when $R_9 > 0.93$.

An important point regarding the clustering algorithm is that it does not differentiate between showers resulting from photons and those resulting from electrons. This allows for electron from $Z \rightarrow ee$ events to be used as high purity samples to study analysis inputs and for defining control regions using electron in place of photons.

6.3.4 Jets

When quarks or gluons are produced they hadronize to make cone-shaped, collimated collections of particles called jets. The jet clustering algorithm aims to combine these particles in order to accurately measure the kinematics of the initial gluon or quark. The algorithm uses the two distance parameters

$$d_{ij} = min(k_{T_i}^{2p}, k_{T_j}^{2p})\frac{\Delta R_{ij}^2}{R^2} \tag{6.1}$$

$$d_{iB} = k_{T_i}^{2p} \tag{6.2}$$

where d_{ij} is the distance between objects i and j and d_{iB} is the distance between object i and the beam B. The transverse momentum of the object is k_T. The parameter p is set as either -1, 0, or +1 to specify whether the anti-k_T, Cambridge/Aachen, or k_T algorithm is used, respectively. The difference between these three algorithms is which object pairs to combine first. The Cambridge/Aachen algorithm clusters starts by clustering particles with the smallest angles between their 4-vectors. The k_T algorithm clusters soft particles first. And the anti-k_T algorithm clusters hard particles first. A comparison of these algorithms in Figure 6.2 shows that both the k_T and Cambridge/Aachen algorithms result in irregular clustering of partons while the anti-k_T algorithm results in more regular, circular jet shapes. The value of ΔR_{ij}^2 is defined as $(\eta_i - \eta_j)^2 + (\phi_i - \phi_j)^2$ and R is the distance parameter that defines the radius or cone size of the jet.

This analysis uses jets reconstructed from PF candidates using the anti-k_T algorithm with the cone size set to $R = 0.4$, also known as AK4PFJets or just PFJets. The algorithm goes through the following steps:

1. The smallest values of d_{ij} and d_{iB} are computed for all objects in the event.
2. Objects i and j are merged into a single object if $d_{ij} < d_{iB}$.
3. Object i is labeled as a jet and removed from the list if $d_{iB} < d_{ij}$.
4. This is repeated until there are no more objects.

After clustering, a series of jet energy corrections (JEC) are sequentially applied to the jets in order to improve calibration and energy resolution. We define the jet p_T response as

$$\mathcal{R} = \frac{p_T}{p_T^{gen}} \tag{6.3}$$

where p_T is the measured or reconstructed transverse momentum of a jet and p_T^{gen} is the generator-level value. Ideally the distribution of $\mathcal{R}$ would have $\langle\mathcal{R}\rangle = 1$, but this is not the case which is where the JEC come in. The first stage of the correction process is a flat correction to remove pileup contributions from the measured jet energy. A description of what pileup is and the mitigation process is available in Section 6.5. The next correction is a detector response correction derived from simulation in bins of η and p_T which is derived by comparing the measured and generator-level p_T in each bin. Next is a residual correction for differences between data and detector simulation. This step exploits momentum conservation in the transverse plain by using dijet, $Z \rightarrow \mu\mu$+jet, and γ+jet data events to derive correction factors. The result can be summarized as

$$\vec{p}_{corr} = C \cdot p_T^{raw} \tag{6.4}$$

$$= C_{PU}(p_T^{raw}, \eta) \cdot C_{sim}(p_T', \eta) \cdot C_{res}(p_T'', \eta) \cdot \vec{p}_{raw} \tag{6.5}$$

where each of correction is applied sequentially such that p_T' is the transverse momentum after application of C_{PU} and p_T'' is after the all subsequent correction have been applied. Once the JEC has been applied the mean of the jet response distribution should be very close to 1 and the width gives the jet energy resolution (JER).

6.4 Missing transverse momentum

The missing transverse momentum $\vec{p_T}$ is defined as the negative vector sum of transverse momentum over all PF objects and can be written as

$$\vec{p_T}^{miss} = -\sum_i \vec{p_T}_i. \tag{6.6}$$

We call the magnitude of this quantity the missing transverse energy E_T^{miss}. For reasons described in Section 7.6.1 a similar variable called the Hard E_T^{miss} is used in which only objects with $p_T > 30$ GeV are used so we have

$$HardE_T^{miss} = |-\sum_i \vec{p_T}_i \cdot \Theta(30 - p_{Ti})| \tag{6.7}$$

where the p_T is measured in units of GeV and Θ is a Heaviside function.

6.5 Pileup mitigation

Multiple interactions occurring in each bunch crossing is referred to as pileup (PU) and can affect reconstruction performance. The number of PU interaction, μ, is simply the number of of interactions in a bunch crossing. It's calculated using Equation 6.8 where L_{inst} is the instantaneous luminosity, σ_{in}^{pp} is the total proton-proton inelastic cross section, and f_{rev} is the LHC orbit frequency.

$$\mu = L_{inst} \frac{\sigma_{in}^{pp}}{f_{rev}} \tag{6.8}$$

Figures 6.3, 6.4, and 6.5 show the distributions of PU interactions during each year of datataking used in this analysis.

When analyzing an *event* we are looking at a single hard-scatter vertex in a bunch crossing. In order to do this, the PF algorithm must mitigate effects associated with additional PU vertices. Charged particles have track information from the silicon tracker and can be removed if they are associated with one of the additional PU vertices on an object-by-object basis, but this is not the case for neutral particles such as photons and neutral hadrons. These effects are instead removed from the event on average. Particular care must be taken to correct isolation variables, which take sum energy deposited within a specified cone of a target object. For example, an isolation variable for photons would sum the energy deposited from different object types (like charged hadrons, neutral hadrons, etc) in the vicinity of a target photon. For isolation variables the PU corrections are given by ρA_{eff}

where ρ is the event-specific energy density per unit area in $\eta \times \phi$ and A_{eff} is an effective area specific to the type of isolation. The corrected isolation variable would then be given by

$$I_{corrected} = max(I - \rho A_{eff}, 0) \tag{6.9}$$

, with I being the uncorrected isolation, and is referred to as the ρ-corrected isolation.

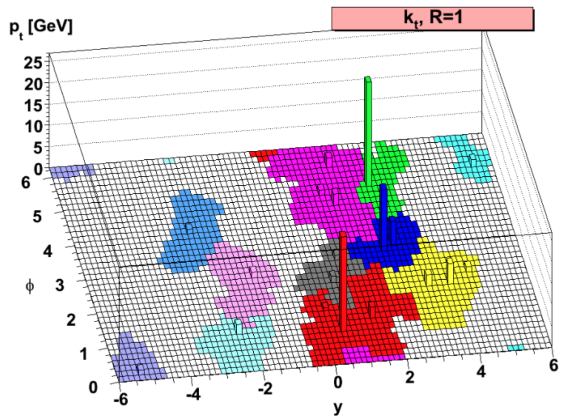

(a) k_T jet clustering algorithm.

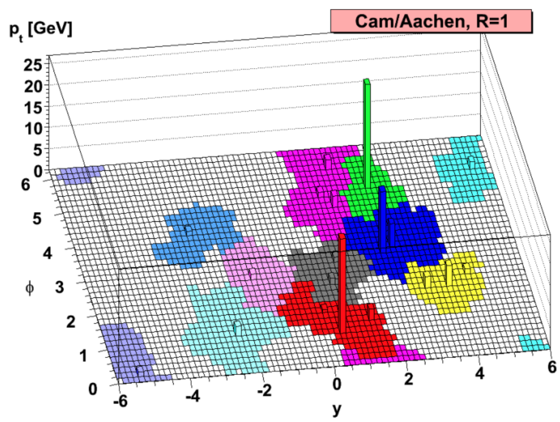

(b) Cambridge/Aachen jet clustering algorithm

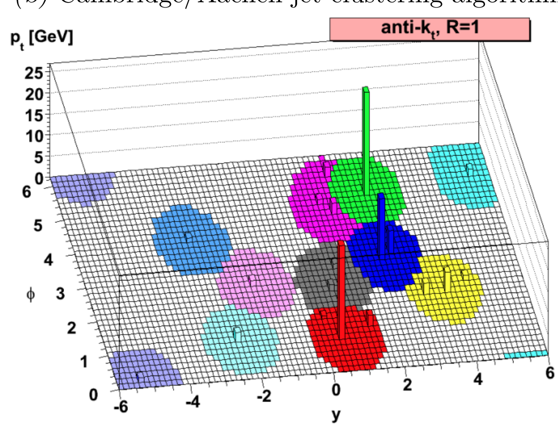

(c) Anti-k_T jet clustering algorithm

Fig. 6.2: Comparison of the k_T, Cambridge/Aachen, and anti-k_T jet clustering algorithms with the distance parameter set to $R = 1$. This is a sample parton-level event upon which each algorithm was applied. Of the three, the anti-k_T algorithm gives the most regularly shaped jets. Reprint from [15]

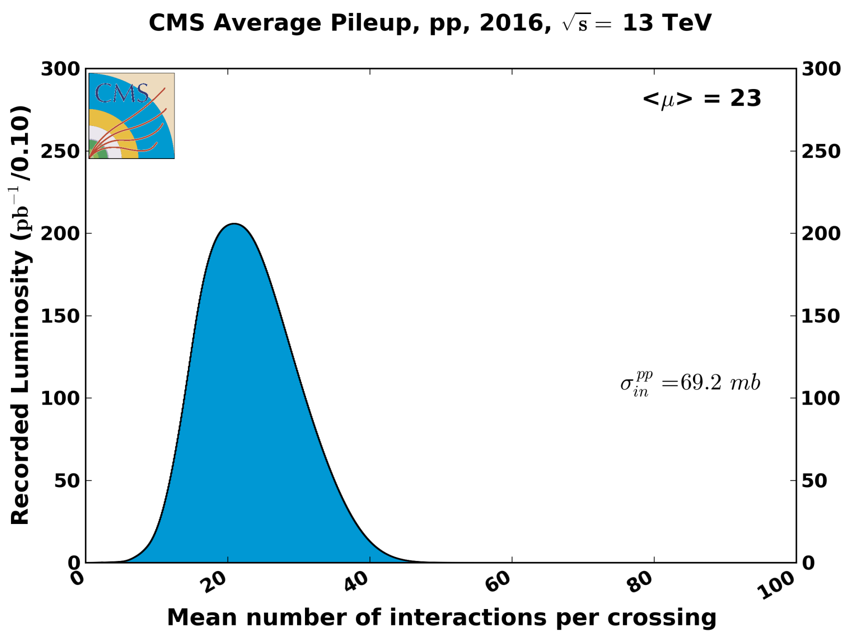

Fig. 6.3: Pileup distribution for 2016

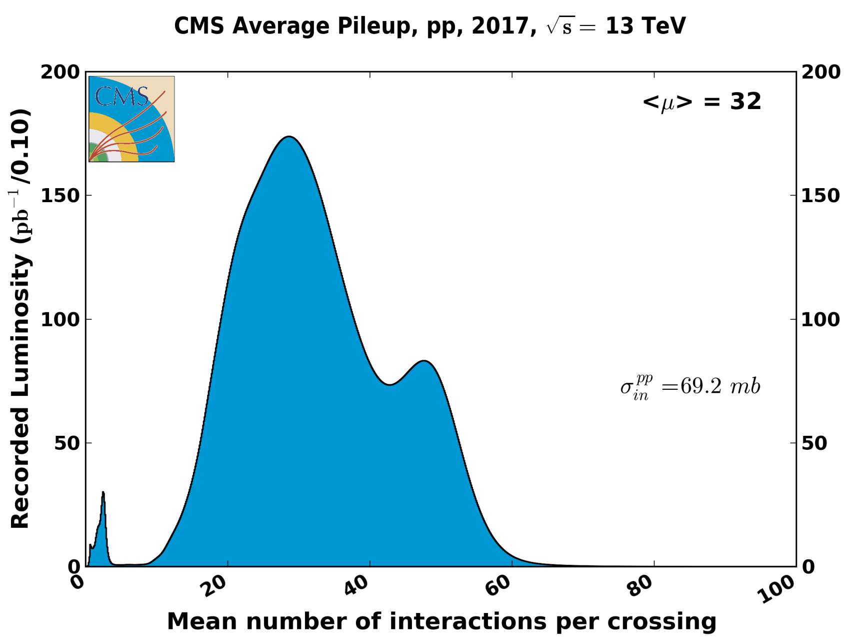

Fig. 6.4: Pileup distribution for 2017.

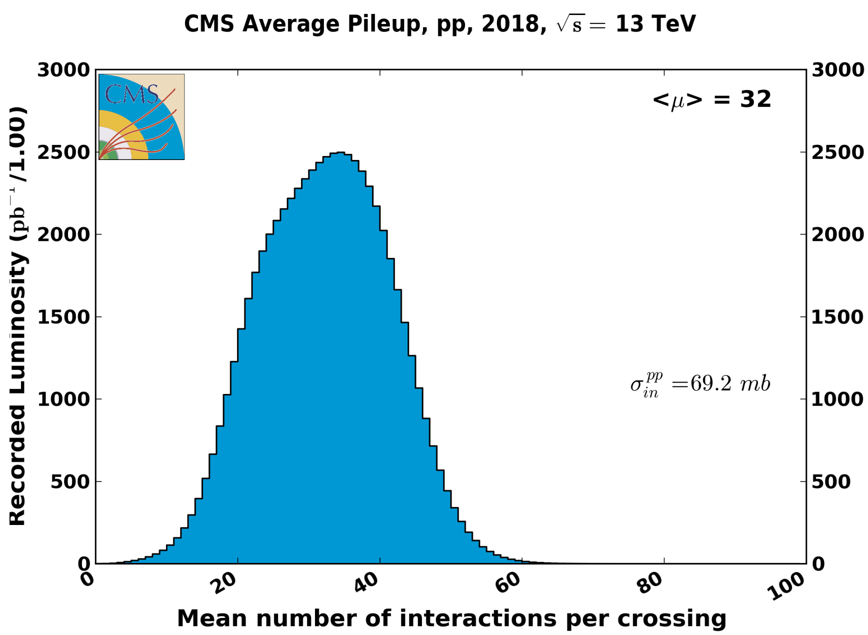

Fig. 6.5: Pileup distribution for 2018.

7. DATA ANALYSIS

7.1 Overview

This analysis is motivated by the GGM supersymmetry breaking scenario in which the strong production of either gluinos or squarks result in a final state containing two photons, jets, and missing transverse momentum. Two example topologies are shown in Figure 7.1. In the T5gg model, each of the produced gluinos decays to a neutralino which then decays to a photon and a gravitino. Similarly, the T6gg model has each of the produced squarks decays to a neutralino which then decays to a photon and a gravitino. In both cases the gravitino escapes the CMS without detection which manifests as missing transverse momentum.

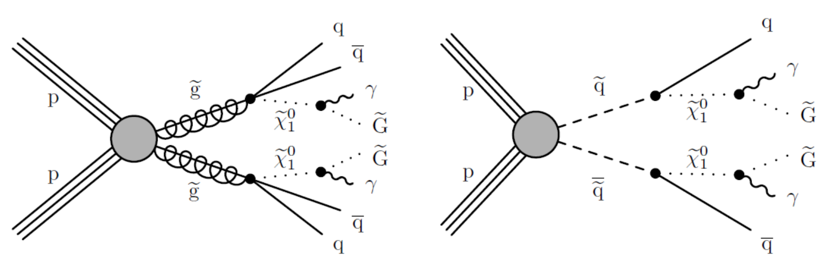

Fig. 7.1: Two examples of GGM supersymmetry breaking processes resulting in final states conaining two photons and missing transverse momentum. The T5gg model (left) shows gluinos produced from $p-p$ collisions which subsequently result in two neutralinos, each decaying to a photon and a gravitino. The T6gg model (right) shows squarks produced from $p-p$ collisions following a similar decay chain.

7.2 Data

This analysis was performed using 137 fb^{-1} of data collected from the CMS detector during the time period commonly referred to as Run 2 which spans from 2016 to 2018. The complete list of the datasets used can be found in Table 7.1. The JSON files used to identify events passing all of the CMS offline data quality monitoring requirements are:

```
Cert_271036 284044_13TeV_23Sep2016ReReco_Collisions16_JSON.txt
Cert_294927 306462_13TeV_EOY2017ReReco_Collisions17_JSON_v1.txt
Cert_314472 325175_13TeV_PromptReco_Collisions18_JSON.txt
```

Tab. 7.1: Data Samples

/DoubleEG/Run2016B-17July2018-ver2-v1
/DoubleEG/Run2016C-17July2018-v1
/DoubleEG/Run2016D-17July2018-v1
/DoubleEG/Run2016E-17July2018-v1
/DoubleEG/Run2016F-17July2018-v1
/DoubleEG/Run2016G-17July2018-v1
/DoubleEG/Run2016H-17July2018-v1
/DoubleEG/Run2017B-31Mar2018-v1
/DoubleEG/Run2017C-31Mar2018-v1
/DoubleEG/Run2017D-31Mar2018-v1
/DoubleEG/Run2017E-31Mar2018-v1
/DoubleEG/Run2017F-31Mar2018-v1
/EGamma/Run2018A-17Sep2018-v2
/EGamma/Run2018B-17Sep2018-v1
/EGamma/Run2018C-17Sep2018-v1
/EGamma/Run2018D-22Jan2019-v2

7.3 Monte Carlo samples

Monte Carlo (MC) simulation were used to validate performance of the analysis on backgrounds, model background contributions, constructing a multivariate discriminant, and determining signal efficiencies. The distribution of pileup (PU) interactions produced in simulated events differs from data. Since the presence of additional PU interactions affects many aspects of reconstruction, it's important for the PU to be properly simulated. To correct for these differences between MC and data the simulated events are reweighted so that the PU profile in MC matches the profile in data. In MC the PU is number of simulated vertices in an event while the PU in data is calculated by the method discussed in Section 6.5.

7.4 Object definitions

The object candidates that are identified by the reconstruction algorithms are subject to further scrutiny in order to achieve optimal purities in the offline analysis.

7.4.1 Photons

Photons are required to have $p_T > 80$ GeV and meet the criteria prescribed by loose ID cuts derived by the e/γ Physics Object Group (EGM POG). The cut variables used to determine the photon ID are:

- H/E - The ratio of the energy deposited in the HCAL tower that is directly behind the ECAL supercluster associated with the photon to the energy deposited in the ECAL supercluster.

- $\sigma_{i\eta i\eta}$ - The log-fractional weighted width of a shower in $i\eta$-space. This variable is used to describe the shower shape or more specifically it provides a measure of the spread of the shower in the η-direction. The log-fractional weight is the log of the ratio of energy deposited in a specific ECAL crystal versus the energy deposited in the associated 5×5 supercluster.

- Particle Flow Charged Isolation - Sum of the p_T of charged hadrons associated with the primary vertex within a cone of $0.02 < \Delta R < 0.3$ of the supercluster.

- Particle Flow Neutral Isolation - Sum of the p_T of neutral hadrons associated with the primary vertex within a cone of $\Delta R < 0.3$ of the supercluster.

- Particle Flow Photon Isolation - Sum of the p_T of photons within a cone of $\Delta R < 0.3$ of the supercluster.

All of the isolation variables listed above are corrected in order to remove pileup as described in Section 6.5. Table 7.2 gives a summary of the pileup-corrected requirements for a loose ID photon. The loose ID working point has an efficiency (background rejection) of 90.08% (86.25%) in the barrel and 90.65% (76.72%) in the end caps. In addition to the p_T and loose ID requirements, a photon must also pass a pixel seed veto (PSV). This means that there is no pixel seed in the tracker matched to the photon.

Photon ID efficiencies differ between data and MC, so when using a photon ID in MC samples we scale them by a ”scale factor” (SF) in order to

Tab. 7.2: Summary of loose ID photons cuts

Variable	Cut Value (Barrel)	Cut Value (Endcap)
H/E	0.04596	0.0590
$\sigma_{i\eta i\eta}$	0.0106	0.0272
Charged Iso	1.694	2.089
Neutral Iso	$24.032 + 0.01512 p_{T\gamma} + 2.259 \times 10^{-5} p_{T\gamma}^2$	$19.722 + 0.0117 p_{T\gamma} + 2.3 \times 10^{-5} p_{T\gamma}^2$
Photon Iso	$2.876 + 0.004017 p_{T\gamma}$	$4.162 + 0.0037 p_{T\gamma}$

replicate detector efficiencies for that that particular ID. The loose photon ID efficiency is measured using the tag-and-probe method on $Z \to ee$ events in both data and MC. The probe is chosen to be one of the electrons while the other electron is used as the tag. The ratio of how many probes pass the loose photon ID requirements and the total number of tag and probe pairs gives the efficiency ϵ for the loose photon ID. We then define the SF as the data efficiency divided by the efficiency in MC or $SF = \frac{\epsilon_{data}}{\epsilon_{MC}}$. Applying the SF to MC events essentially removes the MC efficiency and replaces it with the real detector efficiency to give

$$N_{obs} = N_{gen} \cdot \epsilon_{MC} \cdot SF = N_{gen} \cdot \epsilon_{MC} \cdot \frac{\epsilon_{data}}{\epsilon_{MC}} = N_{gen} \cdot \epsilon_{data}. \tag{7.1}$$

Since this analysis requires two loose ID photons, the scale factor SF is given by the product of scale factors for each of the two loose photons, $SF = SF_{\gamma 1} \cdot SF_{\gamma 2}$. The scale factors for each year are shown in Figures 7.2, 7.3, and 7.4 in bins of photon p_T and η [21].

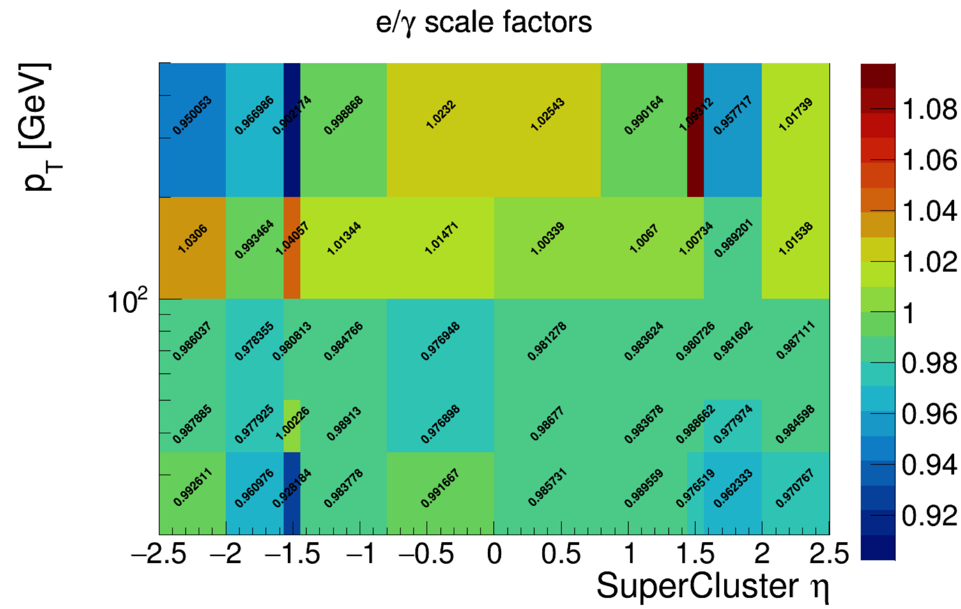

Fig. 7.2: The loose photon ID scale factors for 2016 in bins of photon p_T and η

7.4.2 Electrons

As mentioned earlier, the clustering algorithm doesn't differentiate between showers from photons and those from electrons. In this analysis an electron is defined as an object that passes all of the photon requirements except for the PSV. Inverting the pixel seed requirement while using the same ID criteria ensures that we have orthogonal selections while minimizing the bias potentially introduced by using control regions with electrons to model diphoton signal regions. This essentially allows us to group photons and electrons together to be treated as electromagnetic objects and then splitting those objects into photon and electron objects depending on whether or not there is a pixel seed associated with it.

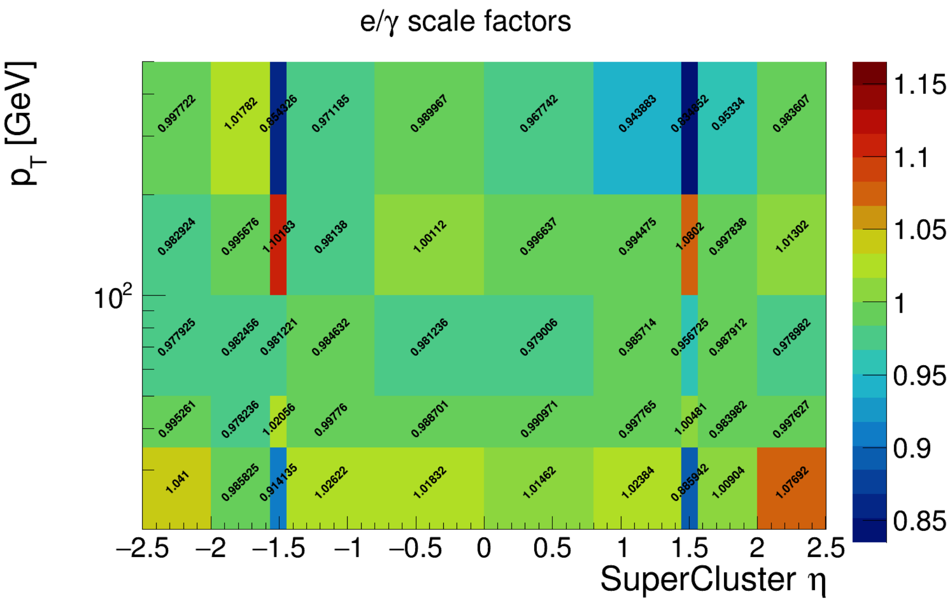

Fig. 7.3: The loose photon ID scale factors for 2017 in bins of photon p_T and η.

7.4.3 Muons

Muons are required to have $p_T > 30$ GeV, $|\eta| < 2.4$, and pass the medium ID requirements listed below [45]:

- Must be identified by PF algorithm as either a tracker or a global muon.
- At least 80% of the inner tracker layers traversed by a track must have recorded hits.
- If it's only reconstructed as a tracker muon, the muon segment compatibility must be > 0.451.
- If it's reconstructed as both a tracker and a global muon:
  - the muon segment compatibility must be > 0.303

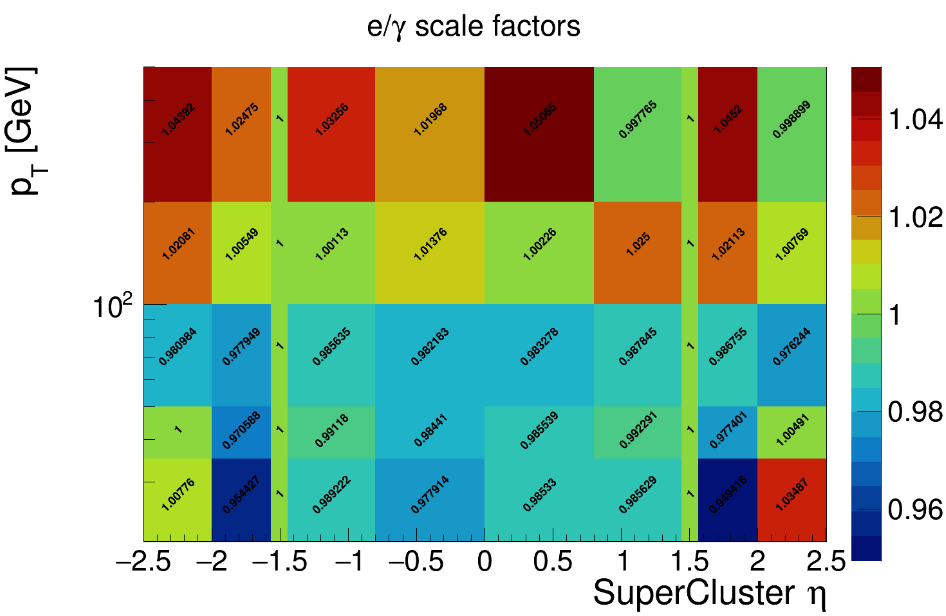

Fig. 7.4: The loose photon ID scale factors for 2018 in bins of photon p_T and η.

- the global fit must have a goodness-of-fit per degree of freedom $(\chi^2/\text{dof}) < 3$
- the χ^2 of the position match between standalone muon and the tracker muon must be < 12
- the kink-finding algorithm must give a maximum χ^2 that is < 20

The types of muons (global, tracker, and standalone) are those described in Chapter 6.3.1. The medium ID criteria results in an efficiency of $> 98\%$ for muons with $p_T > 20$ GeV [18].

7.4.4 Jets

Jets are reconstructed using the anti-k$_T$ algorithm described in Chapter 6.3.4 within a cone having radius $R = 0.4$. The nature of this reconstruction also labels the previously mentioned objects (photons, electrons, and muons) as jets so these need to be removed from the jet collection in order to leave us with only hadronic jets. This process is called ”cleaning” the jets which consists of insuring that there are no isolated photon, electrons, or muons within the area of the jet cone. It’s important to point out that jets can have things like photons in them, but since those things would not pass the isolation criteria required to be reconstructed, that jet would remain as a hadronic jet.

7.5 Event selection

Candidate events are required to pass the following requirements:

- Number of loose photons without a pixel seed requirement ≥ 2
- Number of hadronic jets ≥ 2
- Hard $E_T^{miss} \geq 130$ GeV
- Pass HLT
- Pass relevant event filters recommended by various POGs

The event filters mentioned above are designed to reject events with instrumental anomalies such as noise and beam backgrounds. These filters are:

- globalSuperTightHalo2016Filter
- HBHENoiseFilter
- HBHEIsoNoiseFilter

- eeBadScFilter
- BadChargedCandidateFilter
- BadPFMuonFilter
- CSCTightHaloFilter
- EcalDeadCellTriggerPrimitiveFilter
- ecalBadCalibReducedExtraFilter
- ecalBadCalibReducedFilter
- Good vertex filter (requiring at least one good reconstructed vertex)

7.6 Backgrounds

The sources of background in this analysis can be grouped into three categories. In order of decreasing contribution they are mismeasured hadronic activity, electrons misidentified as photons, and standard model processes having final states with neutrinos and two photons. In events with multiple jets, limitations on the jet energy resolution can give rise to an apparent imbalance in p_T as is shown in Figure 7.5. Such events are usually from quantum chromodynamics (QCD) processes. In these cases jets can be misidentified as photons or there can be real photons being produced. In both cases the result is the appearance of two photons accompanied by E_T^{miss} which mimics our signal. Given the large cross-section for QCD, this is the most significant background in this analysis. The next background,

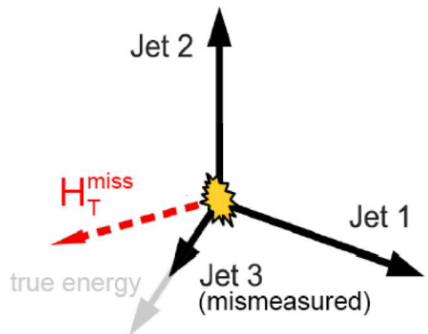

Fig. 7.5: Mismeasurement of Jet3 results in an imbalance in the events transverse momentum.

resulting from the misidentification of electrons as photons, comes from electroweak (EWK) processes, in particular $W\gamma$ events where $W \rightarrow e\nu$. Here the neutrino contributes real E_T^{miss} while the fake photon allows this event to fulfill the diphoton requirement. The final background is from $Z\gamma\gamma \rightarrow \nu\nu\gamma\gamma$ events, which exactly mimic our signal, and is modeled using simulation as it is irreducible.

7.6.1 Instrumental background

The instrumental background is the contribution from events with spurious E_T^{miss} due to mismeasured hadronic activity. The vast majority of interactions produced from proton-proton collisions at the LHC are hadronically rich QCD events. Aside from some very rare final states with heavy-flavor jets, these events do not include neutrinos, which are the only stable particles in the SM that pass through the CMS detector unobserved, and therefore exhibit little or no E_T^{miss} at the parton level. However, the measurements of final-state particles are made using the tracker and calorimeters which have finite energy and momentum resolution. These limitations propagate into the calculation of E_T^{miss} leading to an inequality between the real, parton level E_T^{miss} in an event and the measured E_T^{miss}. Since most of this background is comprised of QCD events, it is commonly referred to as the "QCD background" and those terms are used interchangeably in this thesis. Modeling of this background was done using the Rebalance and Smear technique while a multivariate discriminant was constructed to improve the efficiency of identifying events with fake E_T^{miss}.

Rebalance and Smear

To estimate the QCD background, the Rebalance and Smear method is used. The first step in this method is to *rebalance* events such that the E_T^{miss} is removed from the event to create a set of seed event. In the second step all of the jets are *smeared* with the full jet response function, which is obtained from the jet response discussed in Section 6.3.4. This creates a set of seed events which are used in the second step to *smear* all of the jets with the full jet response function to create events that model the detector response to multi-jet final states. Figure This method has been developed in the context of QCD background estimation for several previous SUSY searches in the all-hadronic channel [32], [43]. It has been developed here to accommodate the presence of photons and other particles in the event who's energy is measured more accurately than that of jets. This was done by fixing the 4-vectors of all of these particles during both the rebalance and smear steps so that only the jet energies are allowed to float in the maximization.

The rebalancing in the first step is performed based on a kinematic

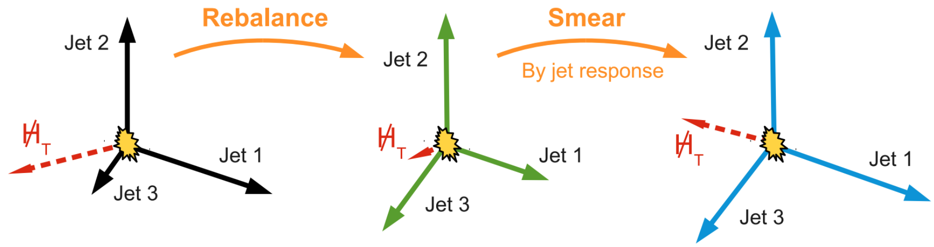

Fig. 7.6: Summary of the steps in the Rebalance and Smear method. The diagram shown here is for an all-hadronic final state and therefore uses hadronic missing transverse energy $\not{H}_T$ which is synonymous with E_T^{miss} in this case[32].

fit [27], which is a least-square fit of the jet energies in the event while taking into account the jet response function. When performing the fit, it is assumed that in each event the kinematic constraints of conservation momentum are fulfilled, i.e. the total $\vec{p_T}$ in the event is balanced. Figure 7.7 shows a comparison of the jet energy response $\mathcal{R} = \frac{p_T}{p_T^{gen}}$ between leading jets in QCD MC events having $E_T^{miss} > 120$ GeV before and after rebalancing of the event. We see that rebalancing has the effect of improving the jet energy resolution, which is the width of this distribution as discussed in 6.3.4, and also recovering some of the energy that was lost in the original jet reconstruction.

In the next step, the seed events obtained through rebalancing are smeared in order to simulate the expected detector-level measurement of each jet. The smearing is done by scaling the p_T of each jet by a random factor sampled from the full pre-rebalanced jet response distribution described in Section 6.3.4. The smear step was performed 50 times on each seed event in order to probe more of the response distribution and improve prediction stability by decreasing the effect of statistical fluctuations.

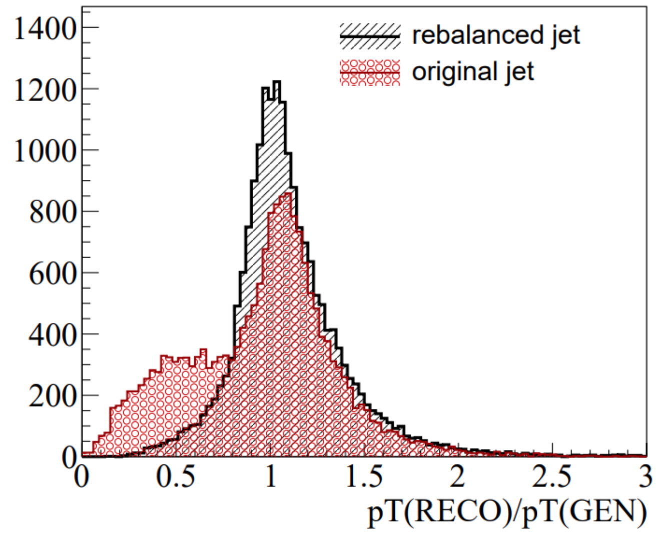

Fig. 7.7: Energy response for the leading jet in QCD MC events with $E_T^{miss} > 120$ GeV before and after being rebalanced. The original jet collection is shown shaded in red while the rebalanced collection is shaded in black. The jet energy response is defined as the ratio of the reconstructed jet p_T and the generator-level jet p_T as described in Section 6.3.4. Rebalancing improves the jet energy resolution and recovers some of the energy that was lost in original reconstruction of the jet.

The result of this process is that we are able to take events from real data, rebalance them to closer to the true value, and then use those rebalanced events as seeds to generate multiple detector-level events. Figure 7.8 shows that the Hard E_T^{miss} spectrum before and after going through this process are in agreement. This method has been proven effective in all-hadronic final states, but in this case it is being used in the presence of two photons also in the final state. As the photon p_T values in the seed events are not smeared like the jets to create these new detector-level events, there is a danger that the photon p_T spectrum could be distorted. This was checked using simulated di-photon events from QCD MC requiring two loose ID photons and Hard $E_T^{miss} > 120$ GeV. The results in Figures 7.9 and 7.10 show that there is no significant distortion of either the leading or next-to-leading photon p_T spectra.

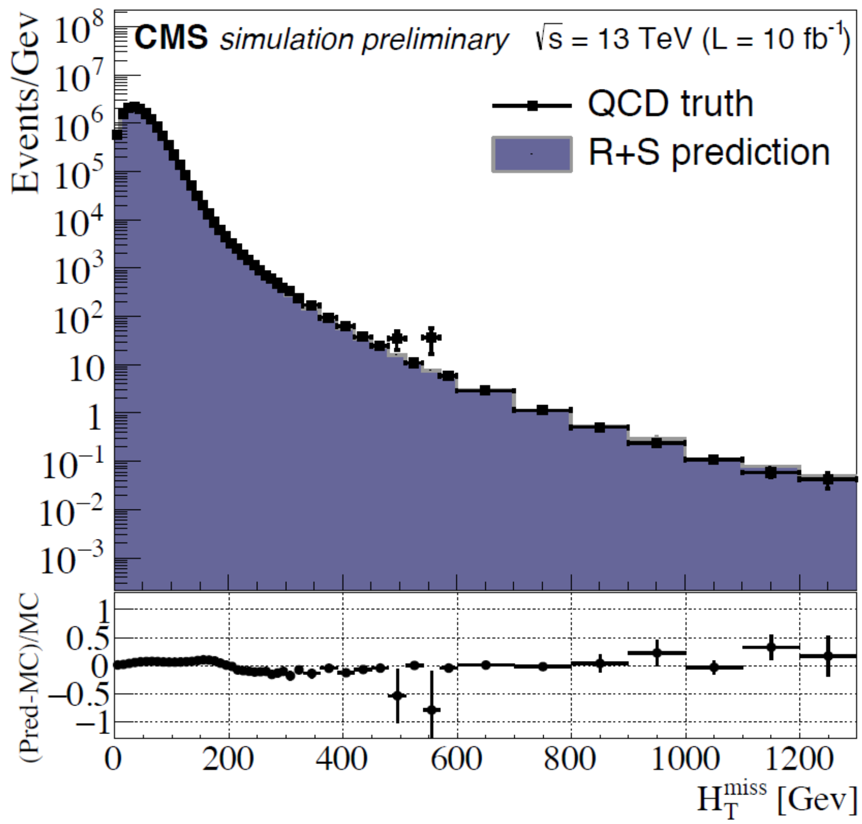

Fig. 7.8: This shows a comparison of the Hard E_T^{miss} distribution for QCD MC events before and after being Rebalanced and Smeared. The data points are taken directly from the QCD simulation while the blue shaded area shows the distribution after application of Rebalance and Smear.

Multivariate discriminant

A boosted decision tree (BDT) was used to develop a discriminating variable for identifying events with real E_T^{miss}. A decision tree is a classifier

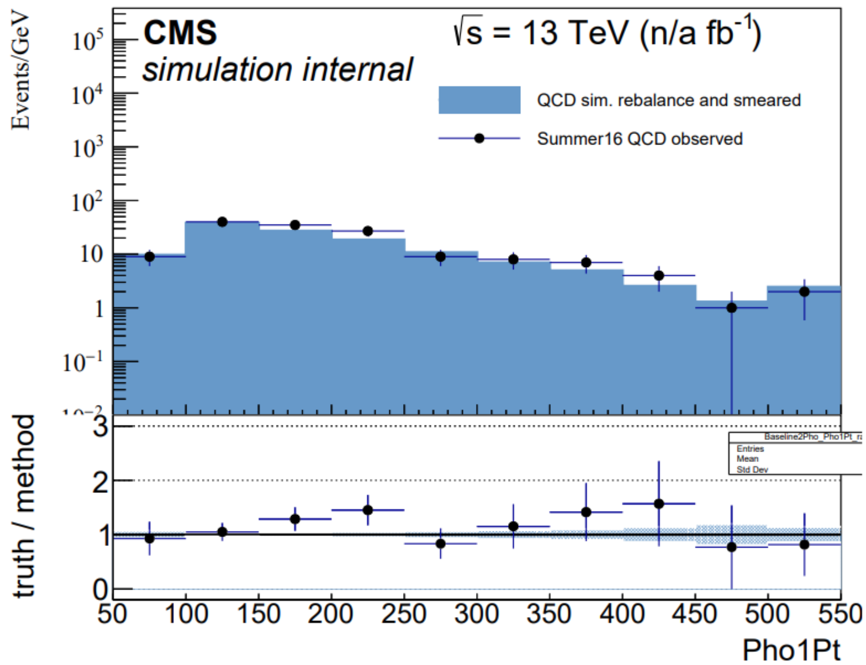

Fig. 7.9: This shows a comparison of the p_t distribution for the leading photons in di-photon QCD MC events before and after being Ralanced and Smeared. These events were required to have two loose ID photons and Hard $E_T^{miss} > 120$ GeV. The data points are taken directly from the QCD simulation while the blue shaded area shows the distribution after application of Rebalance and Smear. We see here that the Rebalance and Smear method causes no significant distortions to the leading photon p_T spectrum in di-photon events.

with a binary tree structure that recursively partitions data or samples into classifications of either signal or background. Figure 7.11 shows an example schematic of a single decision tree. Each splitting of the data takes place at a *node*. Each node uses a single input variable to make a decision regarding classification. This process begins at a *root* node and continues until the final node in the tree is reached, which is referred to as a *leaf* node. The number of layers of nodes is what we call the *depth* of a tree. *Training* is the process of building or growing a tree. The training process begins by

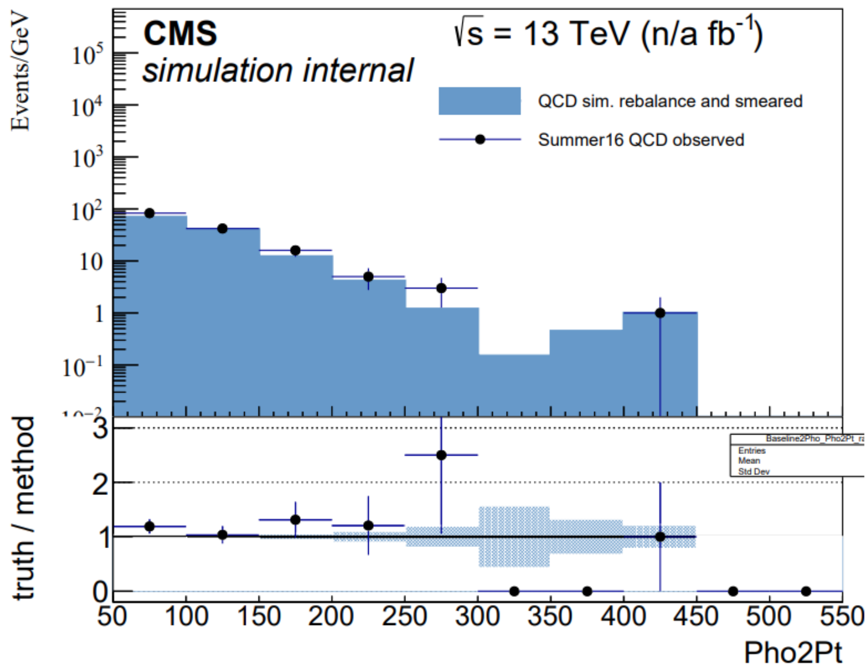

Fig. 7.10: This shows a comparison of the p_t distribution for the next-to-leading photons in di-photon QCD MC events before and after being Ralanced and Smeared. These events were required to have two loose ID photons and Hard $E_T^{miss} > 120$ GeV. The data points are taken directly from the QCD simulation while the blue shaded area shows the distribution after application of Rebalance and Smear. We see here that the Rebalance and Smear method causes no significant distortions to the next-to-leading photon p_T spectrum in di-photon events.

setting an initial splitting criteria at a root node. The root node splits the training data, which consists a set of background samples and a set of signal samples, into two subsets which each go to different node where this same process is repeated until the entire tree is built. The splitting criteria at each node is determined by finding which variable and cut value on said variable results in the best separation between signal and background. The amount of separation is quantified by a separation index known as the Gini

Index, which is defined by $p(1-p)$ where is p is the purity of the resulting subsets. Once the entire tree is built, the leaf nodes are identified as either signal or background depending on whether the majority of the events they contain are from the signal or background training samples.

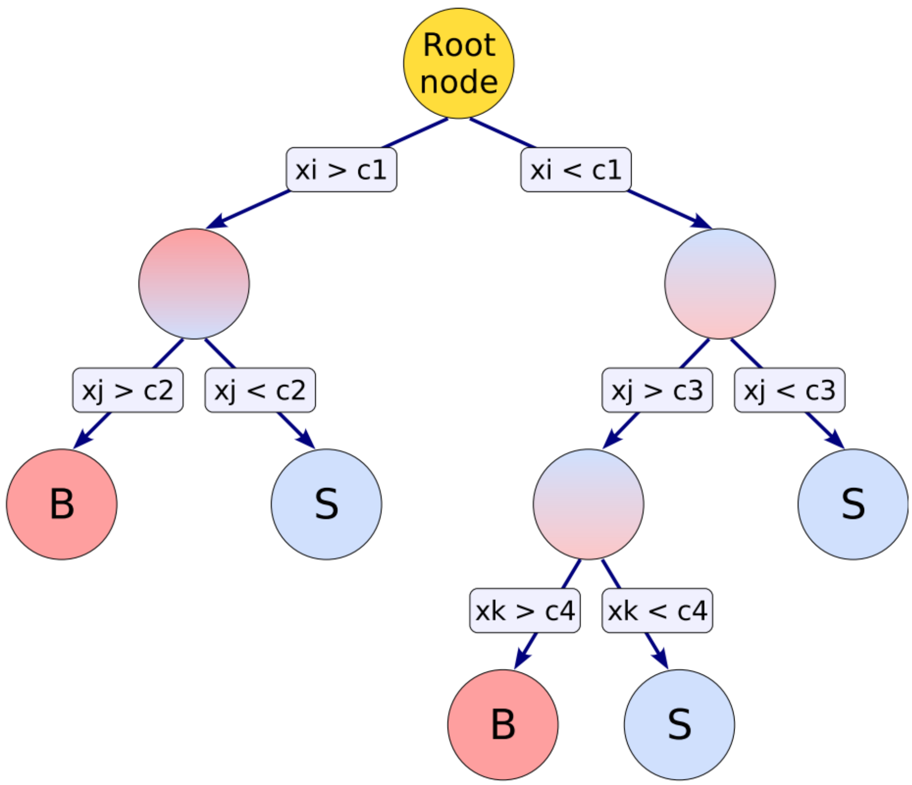

Fig. 7.11: This is a schematic view of a decision tree. Reprint from [36]

Extending this process to many trees, which we call a *forest*, allows us to enhance the classification performance by applying a *boosting* algorithm. For this analysis the AdaBoost (adaptive boost) algorithm was used. The AdaBoost algorithm gives added weight (boost weight) to events in the training sample that misidentified as either signal or background and then uses these reweighted events as the training sample for growing the next tree. The boost weight is given as

$$\alpha = \frac{1 - \epsilon}{\epsilon} \tag{7.2}$$

where ϵ is the misclassification rate of the previous tree. The same α is applied to every event that was misclassified in the training sample. The boosted classification, or BDT score, is then given by

$$BDT_{score}(x) = \frac{1}{N_{trees}} \cdot \sum_{i}^{N_{trees}} \ln(\alpha_i) \cdot h_i(x) \tag{7.3}$$

where x is the set of input variables, and $h(x) = 1$ if the event falls into a signal leaf and -1 if it is in a background leaf. The result is a BDT_{score} that ranges between -1 (background-like) and +1 (signal-like).

Training and testing of the BDT was performed in ROOT using the Toolkit for MultiVariate Analysis (TMVA). The signal samples used for both training and testing are comprised of a combination of different mass points from the T5Wg and T6Wg MC samples. The mass points used were chosen to represent a wide range of mass differences between gluino/squark and neutralino masses. This was done by using the bands of gluino/squark masses shown in Figure 7.12. In order to minimize any bias in the BDT response to model-dependent parameters like the difference between gluino/squark and neutralino masses, the training events used from each mass point were weighted by a factor of one over the number events generated for that particular model. This ensures that each mass point in the mass band is equally represented in the training sample for the BDT. The location of the mass bands were chosen to be near the edge of the exclusion region to target the phase space not yet ruled out by previous analyses. The background samples use for training and testing of the BDT were GJets MC samples that had been Rebalanced and Smeared to increase statistics. These simulate Standard Model processes resulting in final states containing jets and at least one photon which is the source of the fake E_T^{miss} background. The full list of MC samples used in the BDT training can be seen in Table 7.3. As mentioned in Section 4.2.1, there was a substantial upgrade to the pixel detector in between 2016 and 2017 which separates Run 2 into Phase 0 (2016) and Phase 1 (2017 and 2018). In order to remove any effects on the BDT due to different detector response before and after the upgrade, a separate BDT was trained and applied for each of these two phases. For events from these samples to be included in the training or testing of the BDT, they were required to have

- At least two photons without associated pixel seeds as described in Section 7.4.1.
- At least one of those photons is in the EB ($|\eta| < 1.44$)
- Both photons within the range of tracker acceptance ($|\eta| < 2.4$)
- At least two jets as described in Section 7.4.4.
- Hard $E_T^{miss} > 130$ GeV

The input variables used by the BDT are listed below. All energy and momentum variables were normalized to the scalar sum of all of the p_T in

Tab. 7.3: List of MC samples used for training and testing BDT

Signal Samples
SMS-T5Wg_TuneCUETP8M1_13TeV-madgraphMLM-pythia8
SMS-T6Wg_TuneCUETP8M1_13TeV-madgraphMLM-pythia8
Background Sample
GJets_DR-0p4_HT-100To200_TuneCUETP8M1_13TeV-madgraphMLM-pythia8
GJets_DR-0p4_HT-200To400_TuneCUETP8M1_13TeV-madgraphMLM-pythia8
GJets_DR-0p4_HT-400To600_TuneCUETP8M1_13TeV-madgraphMLM-pythia8
GJets_DR-0p4_HT-600ToInf_TuneCUETP8M1_13TeV-madgraphMLM-pythia8

the event $S_T = \sum_{\gamma,jets} |\vec{p}_{T_i}|$ in order to encourage the BDT to focus more on how the energy and momentum was distributed in an event rather than simply the scale of the energy or momentum. Distributions of the input variables for both signal and background are shown in Figure 7.13, 7.14, and 7.15.

- $S_{T_{jets}} = \sum_{jets} |\vec{p}_T|$
- $p_{T_{jets}} = \sum_{jets} \vec{p}_T$
- $p_{T_{\gamma\gamma}} = \vec{p}_{T_{\gamma_1}} + \vec{p}_{T_{\gamma_2}}$
- $HardE_T^{miss} = |-\sum_i \vec{p_{T}}_i \cdot \Theta(30 - p_{Ti})|$
- $\Delta\Phi_{\gamma\gamma} = \Delta\Phi(\vec{p}_{T_{\gamma_1}}, \vec{p}_{T_{\gamma_2}})$
- $\Delta\Phi_{min} = min[\Delta\Phi(\vec{p}_{T_{HardE_T^{miss}}}, \vec{p}_{T_{jet_i}})]$
- $\Delta\Phi_1 = \Delta\Phi(\vec{p}_{T_{HardE_T^{miss}}}, \vec{p}_{T_{jet_1}})$
- $\Delta\Phi_2 = \Delta\Phi(\vec{p}_{T_{HardE_T^{miss}}}, \vec{p}_{T_{jet_2}})$
- $\Delta\Phi_{\gamma\gamma,HardE_T^{miss}} = \Delta\Phi(\vec{p}_{T_{HardE_T^{miss}}}, \vec{p}_{T_{\gamma\gamma}})$

- $\Delta R_{jet_n \gamma_m} = \Delta R(jet_n, \gamma_m)$ for $n = 1, 2$ and $m = 1, 2$

Events in both the signal and background samples are randomly split into either a test or training categories. A substantial difference between the test and training distributions of the BDT response implies that the BDT is not drawing reliable conclusions as to whether an event is signal-like or background-like. A grid search over different combinations of hyperparameters (the maximum depth of a tree and the number of trees) was performed to maximize separation between the signal and background BDT response distributions while maintaining good agreement between the training and test samples. Using 200 trees with a maximum depth of 4 was found to be the optimal choice as increasing either or both of those parameters resulted in over-training with minimal gains in separation of signal and background. The comparison of BDT scores between signal and background events is shown in Figures 7.20 and 7.21 for the Phase 0 and Phase 1 BDTs respectively. Comparisons of training and test samples for Phase 0 are shown in Figures 7.16 (background) and 7.17 (signal). The comparisons for Phase 1 are shown in Figures 7.18 (background) and 7.19 (signal). The training and test samples comparisons don't show any significant deviations while there is good separation between signal and background BDT responses.

Using the BDT we created one control region (low BDT score) and two signal regions (medium and high BDT scores) by defining two BDT score thresholds. The low threshold corresponds to the minimum BDT score with at least 90% acceptance of every signal model or mass point in signal MC samples. Figures 7.22 and 7.23 show the BDT cuts that resulted in 90%

acceptance at each mass point for the T5gg and T6gg models respectively. In both models the value of this BDT cut is always greater than -0.13 so this was chosen as the value separating the low-BDT control region and the medium-BDT signal region. The threshold for the high-BDT region is chosen such that 90% of the fake E_T^{miss} background from the GJets MC is excluded. The BDT response for Rebalanced and Smeared events in this sample for each year is shown in Figures 7.24, 7.25, and 7.26 where over 90% of the events have a score less than 0.03. This puts the threshold for the high-BDT signal region at a BDT score of 0.03. With these three regions we have a very background-pure control region ($BDT \leq -0.13$) and two signal regions, one very pure in signal ($BDT > 0.03$) and one intermediate ($-0.13 < BDT \leq 0.03$), which combined have at least 90% acceptance for all mass points.

7.6.2 Electroweak background

The electroweak background is dominated by events with $W \rightarrow e\nu$ where the electron is misidentified as a photon. Unlike the QCD background these events have real E_T^{miss} due to the presence of a neutrino. The key to estimating this background is determining the rate at which electrons get incorrectly labeled as photons in the signal region. This is done using a tag-and-probe method where the tag is an electron (a loose ID photon that fails the PSV) and the probe is categorized as either a photon or an electron. The result is an electron-electron region (ee) and an electron-photon region ($e\gamma$) that are selected from the data. As both of these regions contain $Z \rightarrow ee$ decays, fits are applied in each of the samples to the invariant mass spectra m_{ee}

and $m_{e\gamma}$ as seen in Figure 7.27. The integrals of these fits are calculated over the range of the Z mass peak to give the number of events in each category, $N_{e\gamma}$ and N_{ee}. The rate that an electron fakes a photon is given by the ratio $N_{ee}/N_{e\gamma}$. These values for each year are listed in Table 7.4. These fake rates are used to perform a data-driven estimation of the electroweak background by rescaling $e\gamma$ events in data by the rate at which electrons are falsely identified as photons.

Tab. 7.4: Summary of the rate at which an electron fakes a photon.

Year	Rate(e fakes γ)
2016	2.02% ±0.05%
2017	4.52% ±0.18%
2018	4.65% ±0.04%

7.6.3 Irreducible background

The irreducible $Z\gamma\gamma \to \nu\nu\gamma\gamma$ background produces two photons and has inherent E_T^{miss} via the neutrinos. There is no easy way to separate these events from our signal so it is estimated using MC simulation. The prediction of this background is given by $N_{pred} = N_{MC} \cdot R$ where R is an overall simulation-to-data normalization factor obtained by comparing $Z\gamma\gamma \to LL\gamma\gamma$ MC samples to $Z\gamma\gamma \to \mu\mu\gamma\gamma$ and $Z\gamma\gamma \to ee\gamma\gamma$ events in data. The event selection criteria, relaxed from the baseline version in order to maximize statistics, was

- 2 looseID photons with $p_T > 30$ GeV and no pixel seed
- 2 like-flavored leptons with $p_T > 30$ GeV

  2 mediumID muons or

2 electrons (looseID photons with pixel seeds).

The resulting dilepton invariant mass spectra for 2016 MC and data are shown in Figure 7.28. The number of events with dilepton mass within 10 GeV of the Z boson mass is shown in Table 7.5. The ratio of data events to MC events gives the normalization factor R factor which was applied to the $Z\gamma\gamma \to \nu\nu\gamma\gamma$ MC to give the background prediction for this process.

Tab. 7.5: Summary of $Z\gamma\gamma \to \nu\nu\gamma\gamma$ model validation

Year	Data Events	MC Events	$R = \frac{data}{MC}$
2016	$10.0^{+4.78}_{-3.05}$	10.54 ±0.54	$0.95^{+0.46}_{-0.29}$
2017	$14.0^{+5.32}_{-3.65}$	10.15 ±0.56	$1.38^{+0.53}_{-0.37}$
2018	$15.0^{+5.43}_{-3.79}$	14.83 ±0.83	$1.01^{+0.36}_{-0.26}$

7.7 Signal and control regions

The background estimation methods are validated in various data control regions.

The first such region is the ee region in which the pixel seed veto requirements are inverted, resulting in events with two electrons. This region is primarily composed of $t\bar{t}$, which is a source of real E_T^{miss}, and Drell-Yan (DY) with $Z \to ee$. As the DY background is comprised of multi-jet events with two electrons (photos with inverted pixel seed requirements), this is a source of fake E_T^{miss} that is very similar yet orthogonal to our expected signal which consists of multi-jet events with two photons. Applying Rebalance and Smear on these events results in an estimation of the DY background. Looking at the invariant mass distribution of the two electrons, we see in Figure 7.29 that the Rebalance and Smear DY estimation, which is fake

E_T^{miss}, dominates on the Z mass peak. Looking at the Hard E_T^{miss} distribution in events where the invariant mass is within 10 GeV of the Z mass peak gives a very pure fake E_T^{miss} region shown in Figure 7.30 that shows good agreement between data and prediction.

The BDT output is used to define the data control region and signal region having two photons, as mentioned in Section 7.6.1. The regions are also binned in Hard E_T^{miss}. The results are shown in Figure 8.1. Interpretations of these results is discussed in the next chapter.

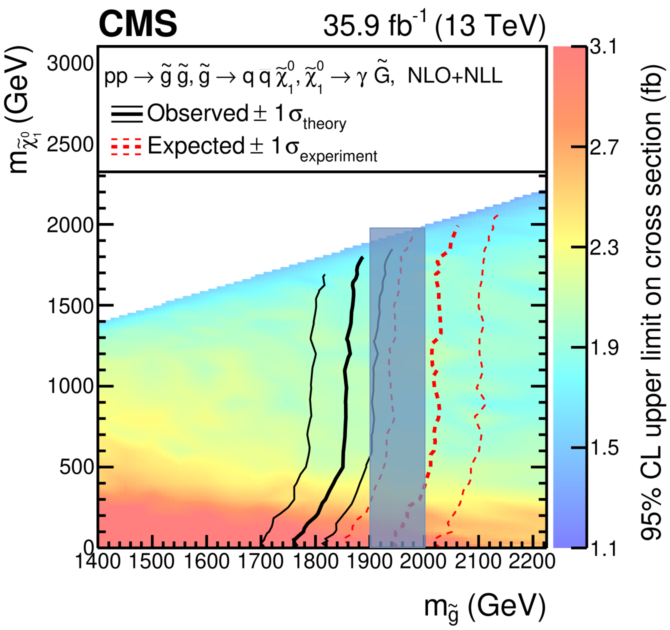

(a) Cross-section upper limits for gluino pair production

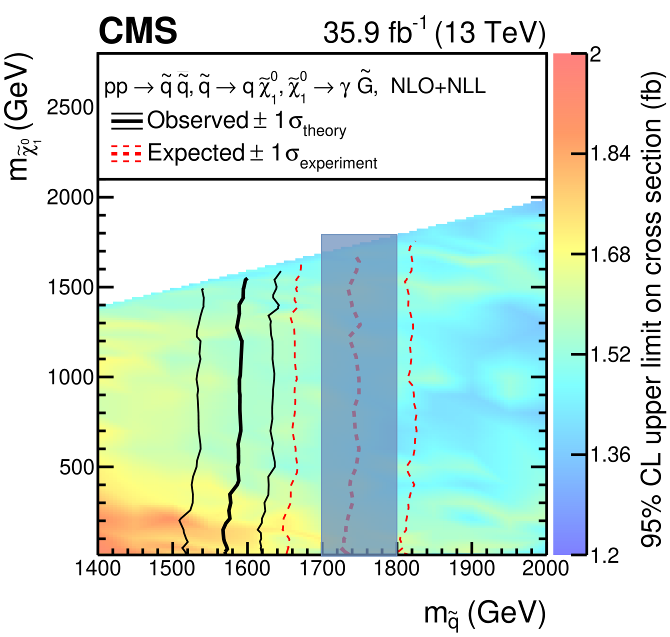

(b) Cross-section upper limits for squark pair production

Fig. 7.12: The 95% confidence level upper limits on the pair production cross sections for gluinos (7.12a)and squarks (7.12b)as a function of gluino/squark and neutralino masses as reported in [44]. The shaded vertical bands show the mass bands used in the BDT training.

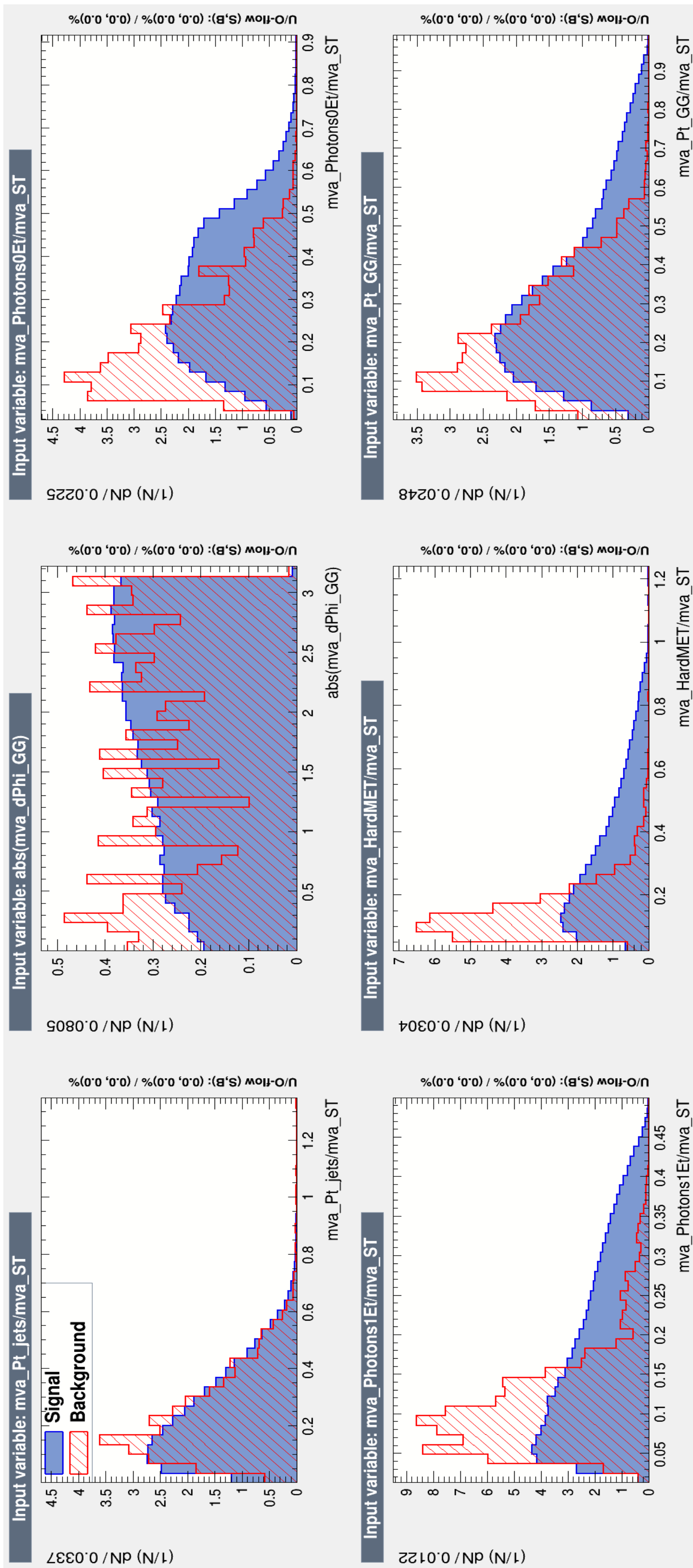

Fig. 7.13: Signal and background input variable distributions for the BDT. The red distribution represents the background while the blue is signal.

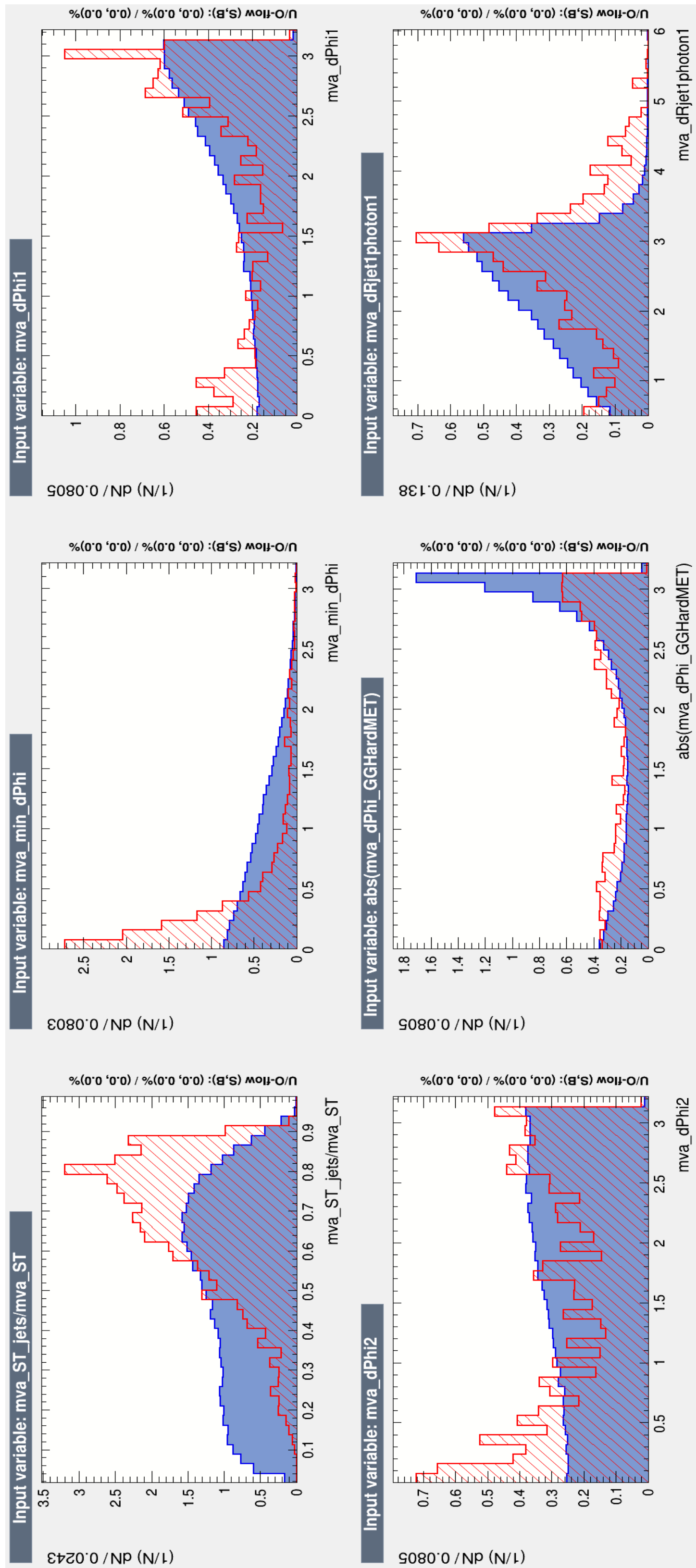

Fig. 7.14: More signal and background input variable distributions for the BDT. The red distribution represents the background while the blue is signal.

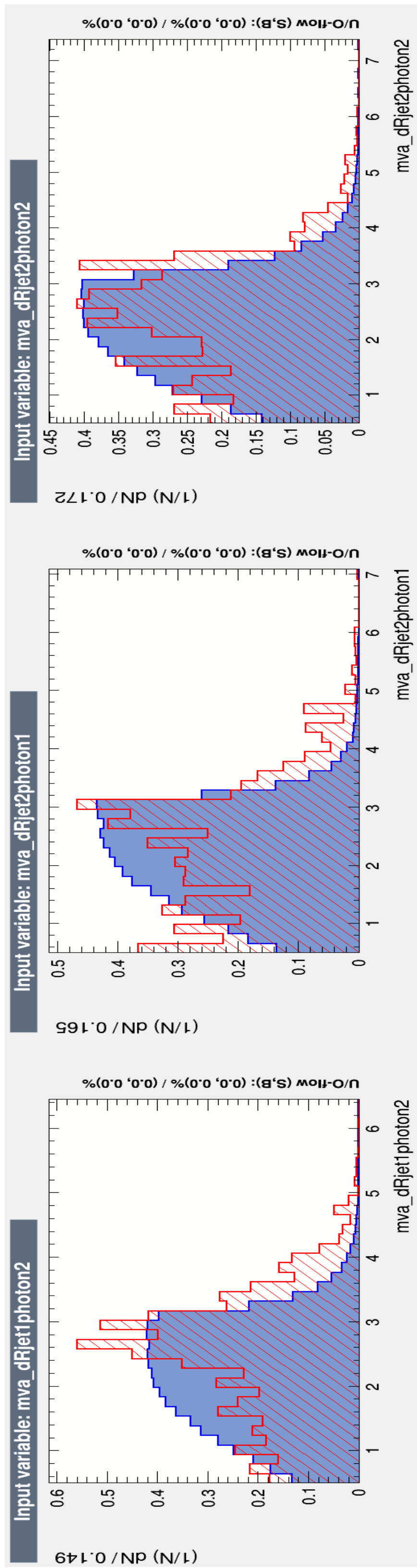

Fig. 7.15: More signal and background input variable distributions for the BDT. The red distribution represents the background while the blue is signal.

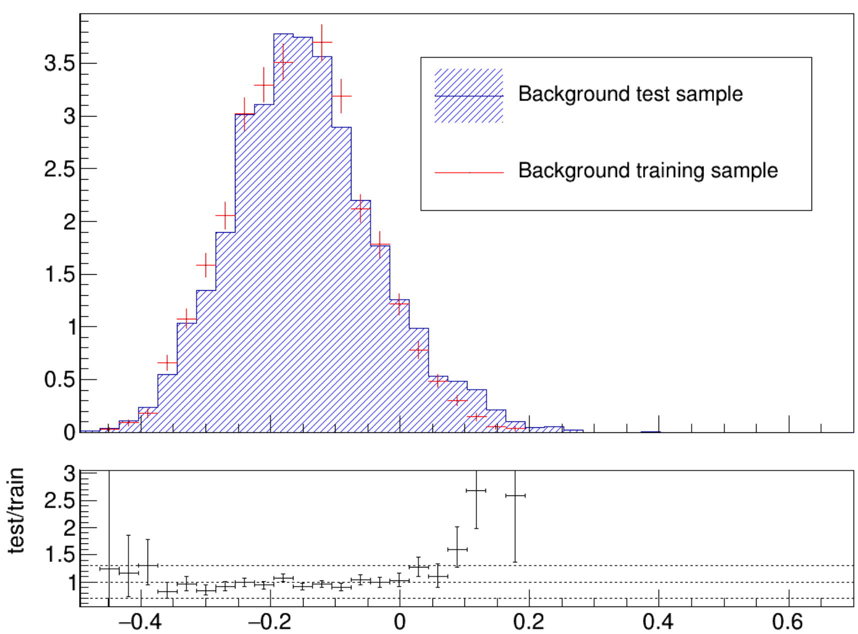

Fig. 7.16: Overtraining check for background samples in Phase 0 BDT. The BDT score distributions for the training (red) and testing (blue) samples are plotted on the same graph.

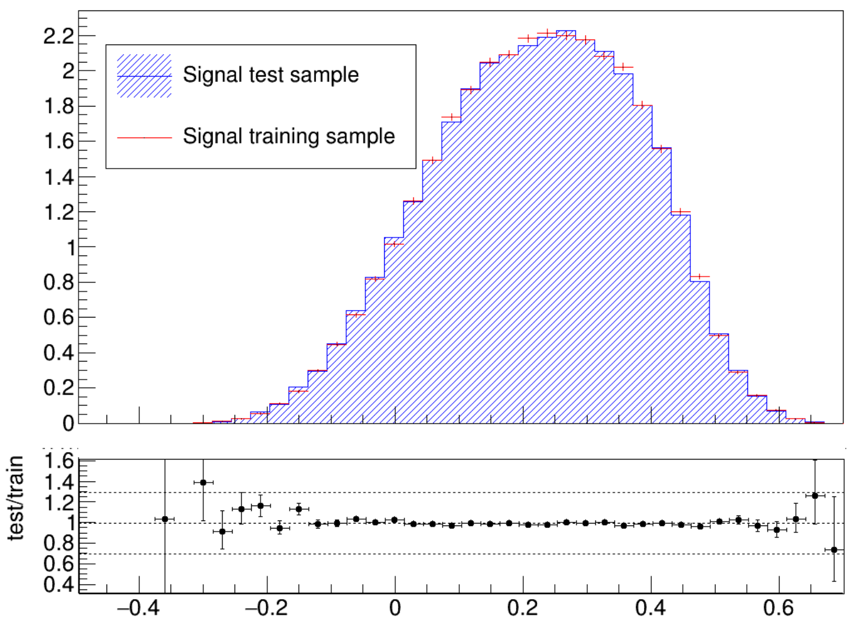

Fig. 7.17: Overtraining check for signal samples in Phase 0 BDT. The BDT score distributions for the training (red) and testing (blue) samples are plotted on the same graph.

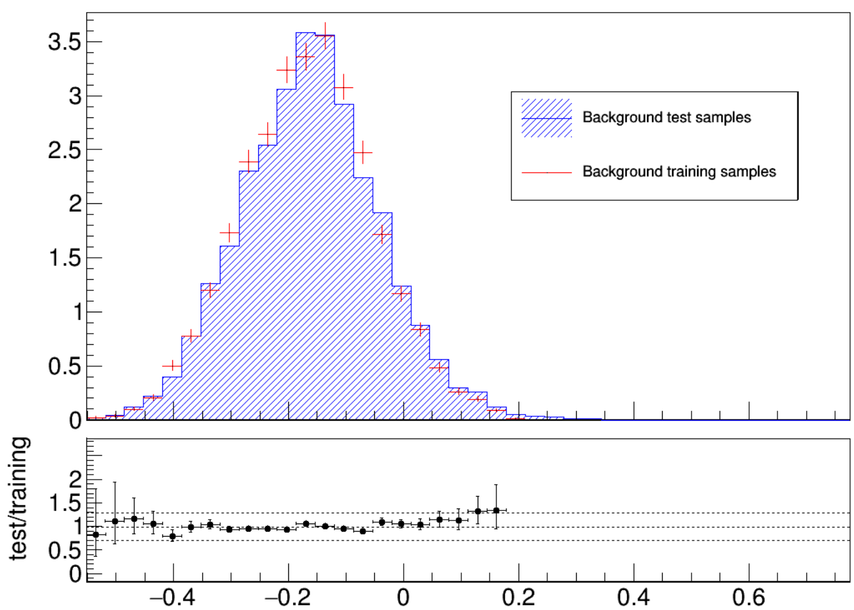

Fig. 7.18: Overtraining check for background samples in Phase 1 BDT. The BDT score distributions for the training (red) and testing (blue) samples are plotted on the same graph.

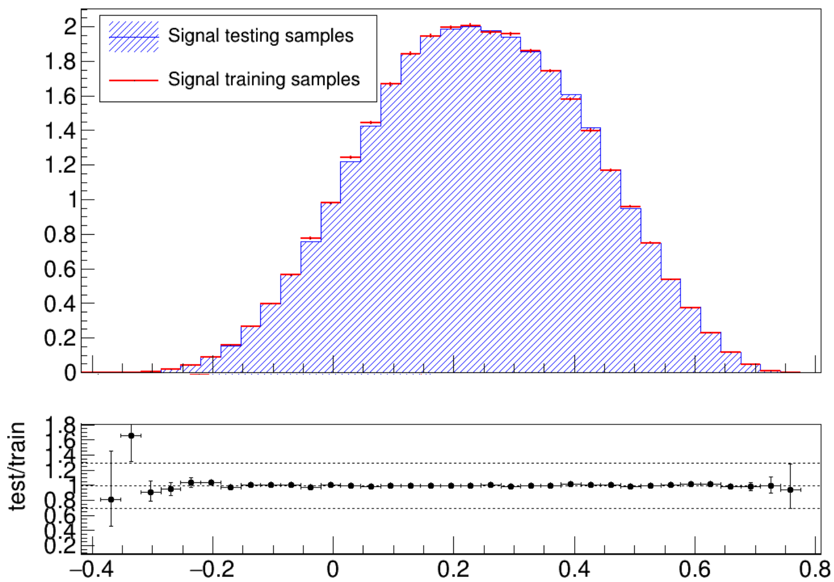

Fig. 7.19: Overtraining check for signal samples in Phase 1 BDT. The BDT score distributions for the training (red) and testing (blue) samples are plotted on the same graph.

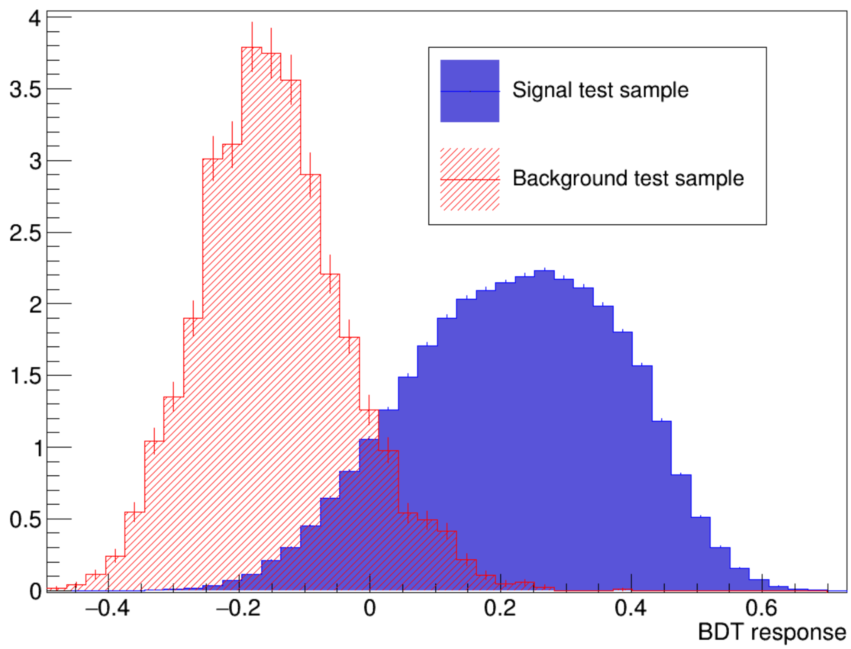

Fig. 7.20: Phase 0 BDT response for signal (blue) and background (red)

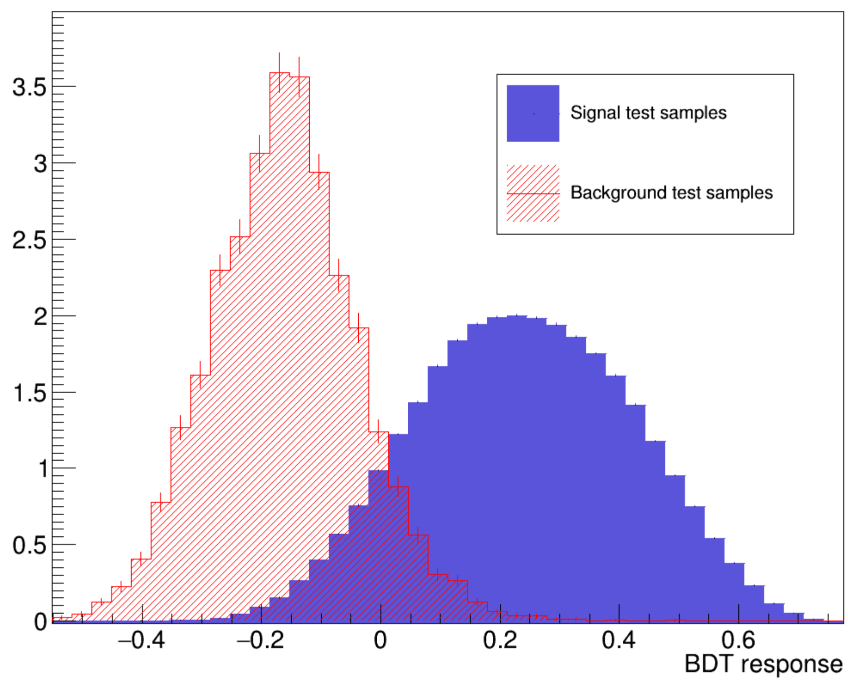

Fig. 7.21: Phase 1 BDT response for signal (blue) and background (red)

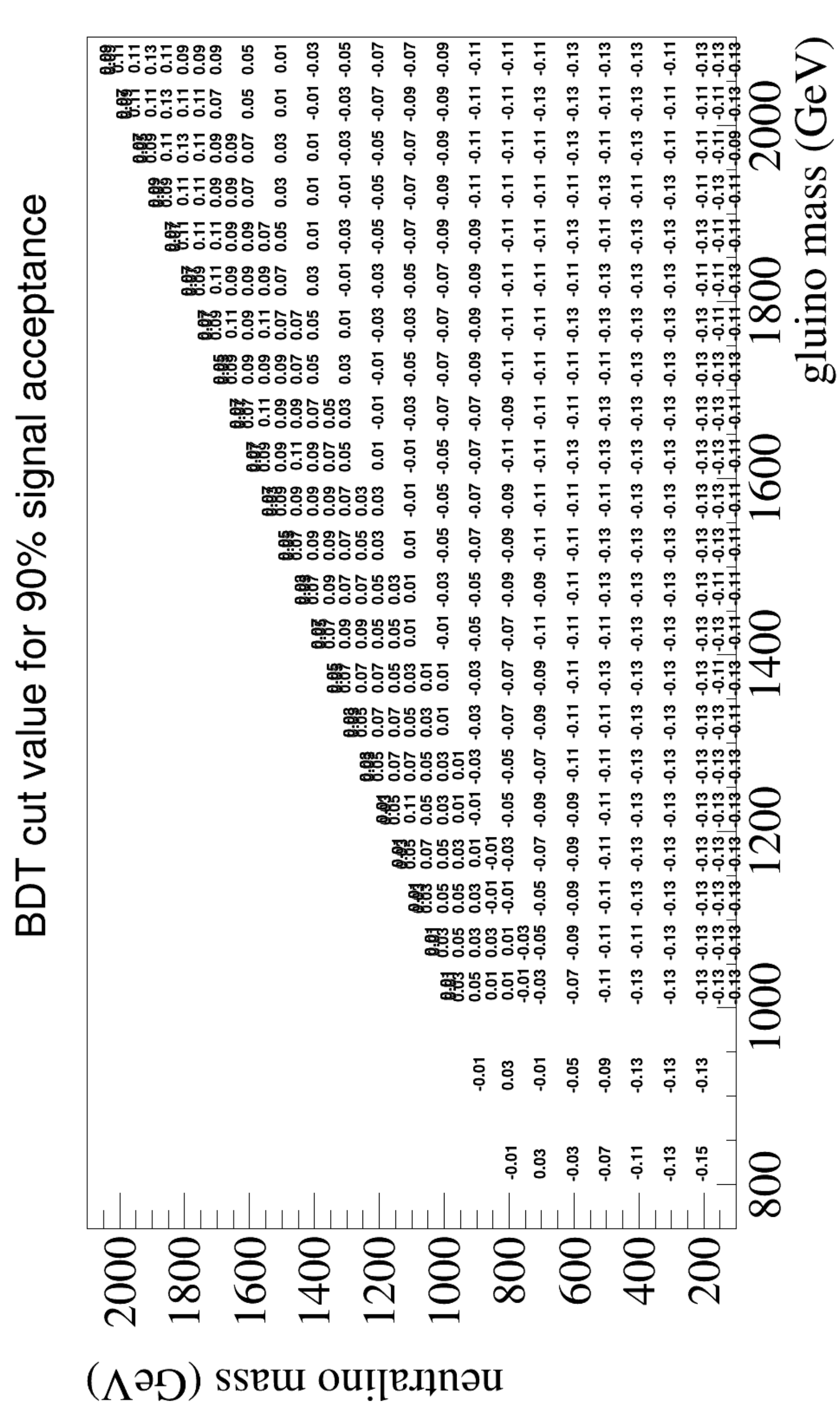

Fig. 7.22: BDT cut values on T5gg models resulting in 90% signal acceptance.

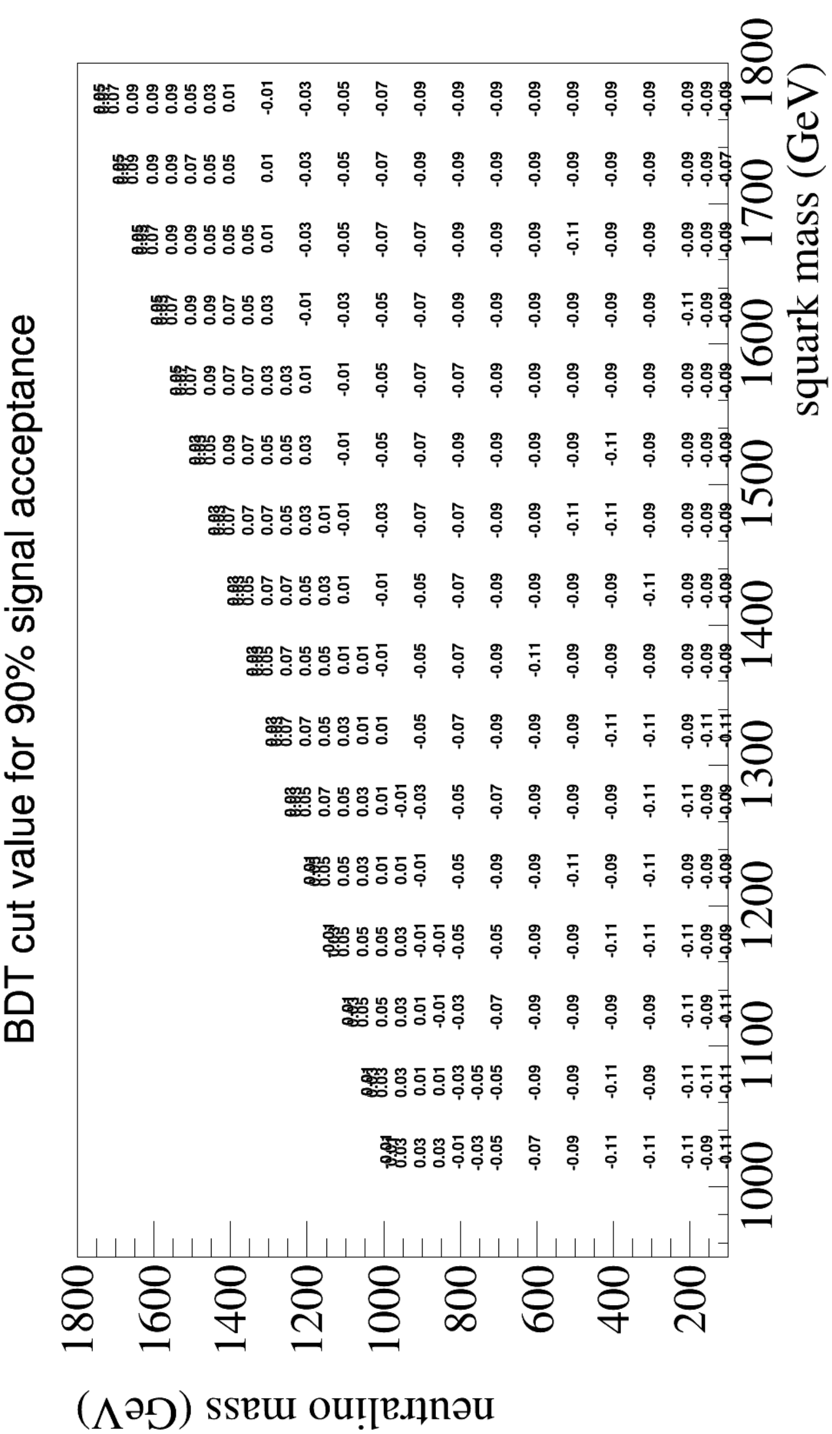

Fig. 7.23: BDT cut values on T6gg models resulting in 90% signal acceptance.

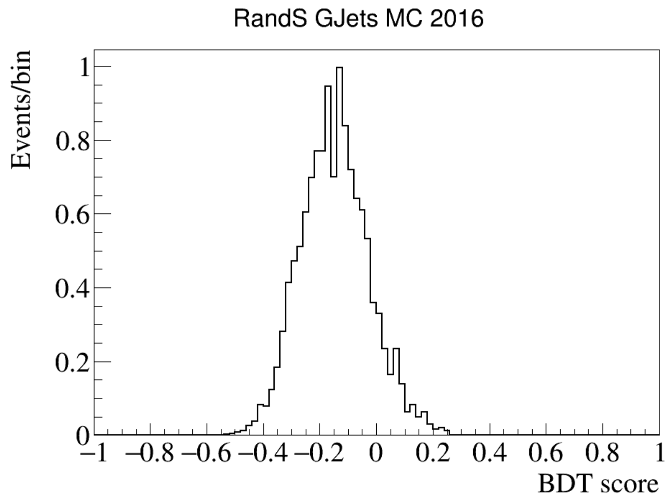

Fig. 7.24: This is the BDT score distribution for Rebalance and Smear events from the 2016 GJets MC samples. Requiring a BDT score above 0.03 removes 90% of this background.

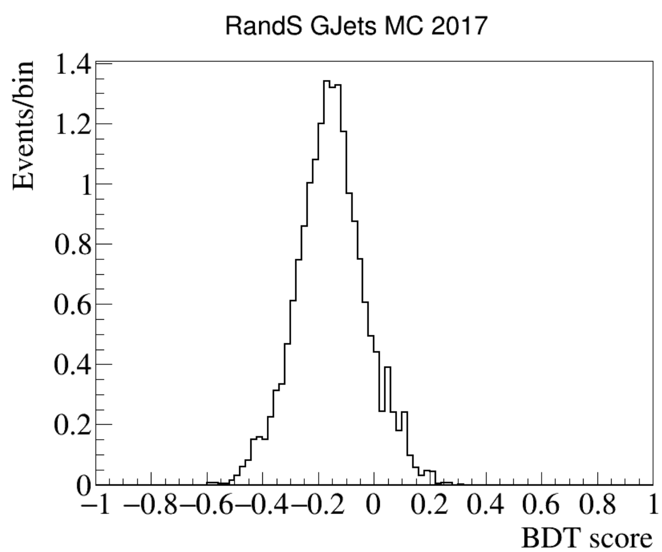

Fig. 7.25: This is the BDT score distribution for Rebalance and Smear events from the 2017 GJets MC samples. Requiring a BDT score above 0.03 removes 90% of this background.

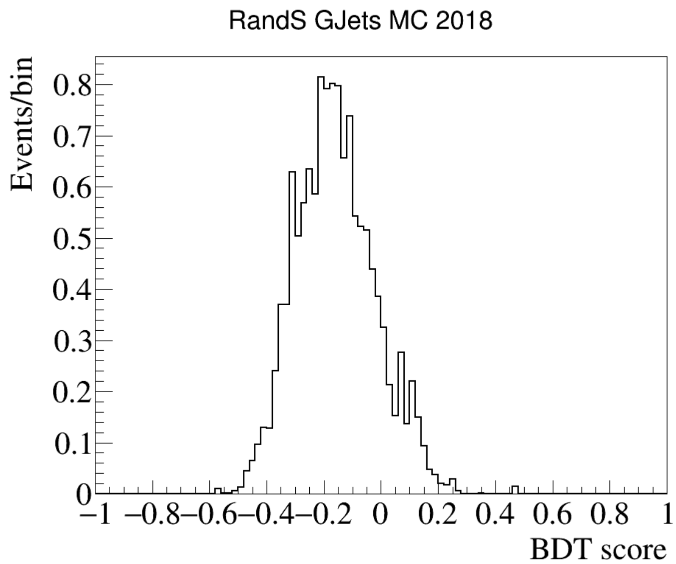

Fig. 7.26: This is the BDT score distribution for Rebalance and Smear events from the 2018 GJets MC samples. Requiring a BDT score above 0.03 removes 90% of this background.

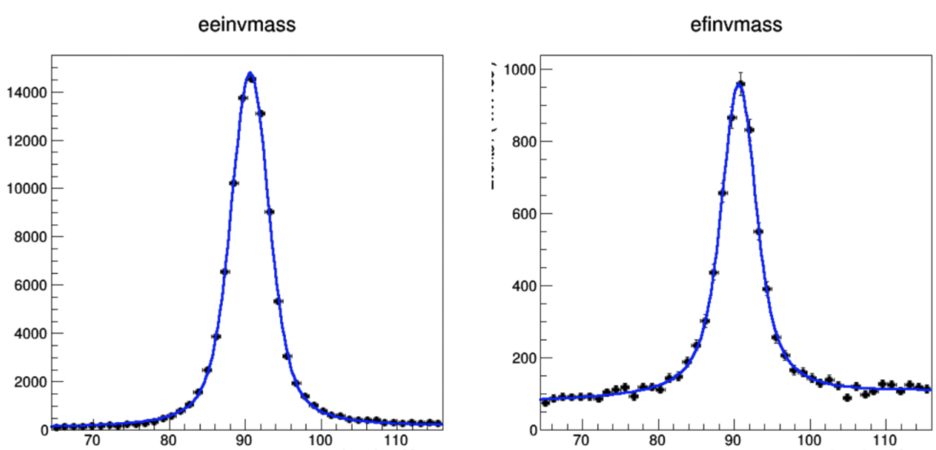

Fig. 7.27: Invariant mass spectrum for electron-electron events (left) and electron-photon events (right)

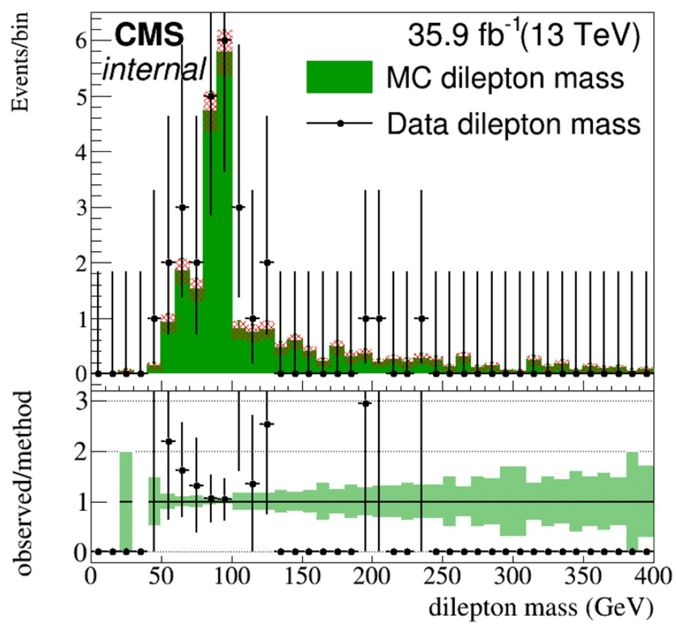

Fig. 7.28: Comparison of dilepton invariant mass spectra from ZGGToLLGG events in MC and data. Good agreement is seen in the region where the invariant mass is within 10 GeV of the Z boson mass (91 GeV).

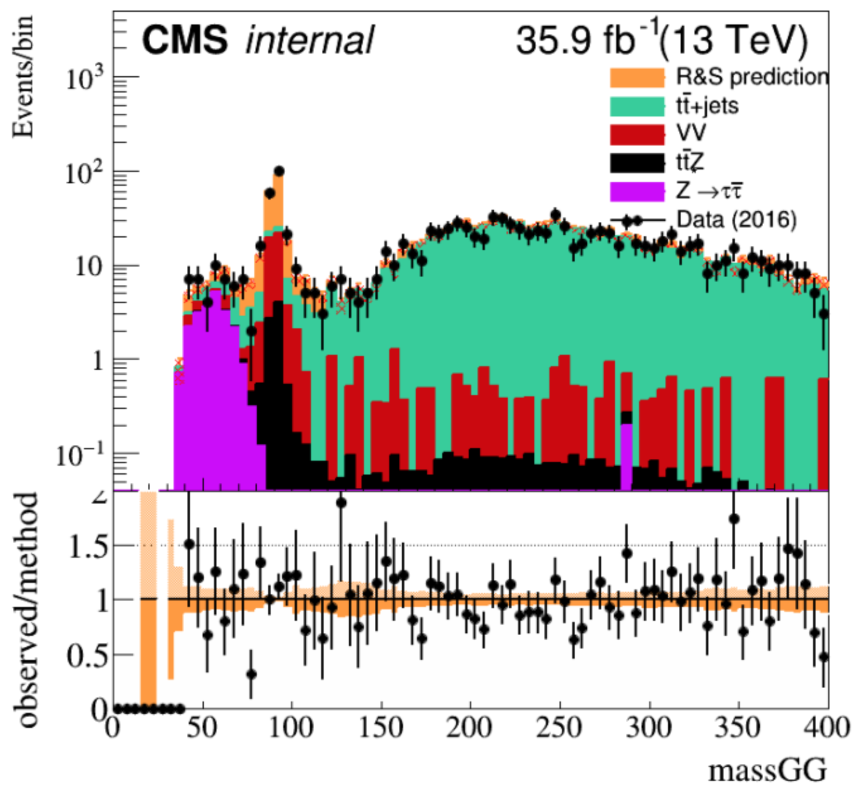

Fig. 7.29: Invariant mass m_{ee} distribution for di-electron control region. The black dots represent data. The backgrounds here are estimated using MC simulation. Each background sample is included in the stacked histogram.

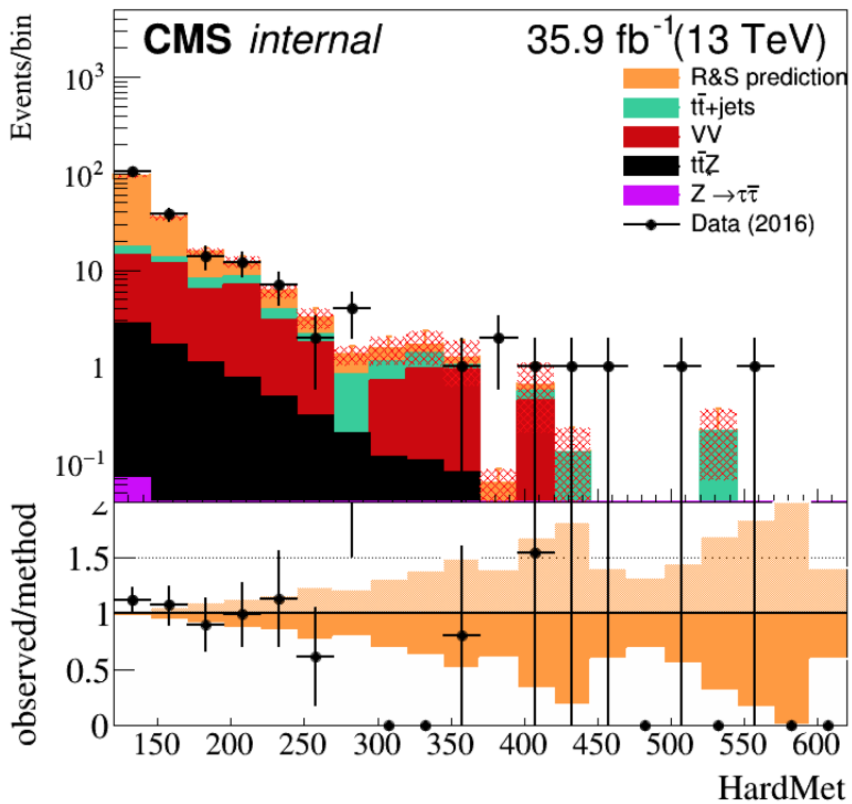

Fig. 7.30: Hard E_T^{miss} distribution for di-electron control region with invariant mass m_{ee} within 10 GeV of the Z boson mass. The black dots represent data. The backgrounds here are estimated using MC simulation. Each background sample is included in the stacked histogram.

8. RESULTS AND INTERPRETATIONS

8.1 Observation vs Predicted

Table 8.1 shows the a summary of the observations made over the course of all three years, giving a total of 137 fb^{-1} of integrated luminosity. Figure 8.1 shows the observations compared to the expected background in each search bin. Each bin represents a Hard E_T^{miss} range and the bins are grouped into regions depending on BDT scores. The low-BDT score control region makes up the first four bins, followed by four mid-BDT bins and then four high-BDT bins which make up the signal region. We don't observe a significant excess above the expected SM backgrounds in any of the search bins so we then use these results to set limits on the allowed squark and gluino masses in the T5gg and T6gg simplified models.

8.2 Simplified models

The interpretation of these results uses the T5gg and T6gg simplified models. The T5gg simplified model gluino ($\tilde{g}$) pair production while the T6gg model assumes squark ($\tilde{q}$) pair production. The lightest supersymmetric particle (LSP) in both models is the gravitino $\tilde{G}$ and the next-to-lightest supersymmetric particle is the neutralino $\tilde{\chi}_1^0$. Figure 7.1 shows examples of

Tab. 8.1: Summary of observations with 137 fb^{-1} of integrated luminosity. Each bin represents a range of Hard E_T^{miss} as can be seen in Figure 8.1 with bin 1 being the left-most. The first four bins are the low-BDT score control region, bins 5-8 are the mid-BDT signal region, and bins 9-12 are the high-BDT signal region.

bin	QCD	EWK	$Z\gamma\gamma$	tot. bkg.	obs.
1	15.68 ± 6.27	1.34 ± 0.13	0.09 ± 0.03	17.11 ± 6.27	20
2	8.78 ± 3.51	1.38 ± 0.14	0.10 ± 0.03	10.26 ± 3.52	6
3	2.90 ± 1.16	0.52 ± 0.05	0.06 ± 0.02	3.47 ± 1.16	4
4	0.49 ± 0.20	0.17 ± 0.02	0.01 ± 0.00	0.68 ± 0.20	0
5	24.37 ± 9.75	3.19 ± 0.32	0.23 ± 0.07	27.79 ± 9.75	28
6	14.90 ± 5.96	2.96 ± 0.30	0.35 ± 0.10	18.22 ± 5.97	27
7	6.36 ± 2.55	2.30 ± 0.23	0.31 ± 0.09	8.97 ± 2.56	12
8	1.74 ± 0.70	0.82 ± 0.08	0.14 ± 0.04	2.70 ± 0.70	2
9	24.27 ± 9.71	5.17 ± 0.52	0.69 ± 0.21	30.13 ± 9.72	28
10	14.88 ± 5.95	5.74 ± 0.57	0.95 ± 0.28	21.56 ± 5.98	23
11	7.94 ± 3.17	5.66 ± 0.57	1.07 ± 0.32	14.66 ± 3.24	19
12	6.31 ± 2.52	5.77 ± 0.58	1.61 ± 0.48	13.68 ± 2.63	18

decay chains for both models.

Monte Carlo scans were used to evaluate the expected signal distributions for these models. The scan for the T5gg model was produced in bins of gluino and neutralino masses while the T6gg scan was binned in squark and neutralino masses. `MadGraph5_aMC@NLO` was used for event generation[8] while `PYTHIA 8` was used for simulating parton showering, hadronization, and multi-parton interactions[46]. The detector response was simulated with CMS fast simulation[5]. Production cross sections were calculated next-to-leading order (NLO) plus next-to-logarithmic (NLL) accuracy [13]. For calculations of gluino cross sections the squark was taken to be heavy and decoupled and vice versa for squark cross section calculations. The cross sections for gluino and squark pair production are shown in Figures 8.2 and

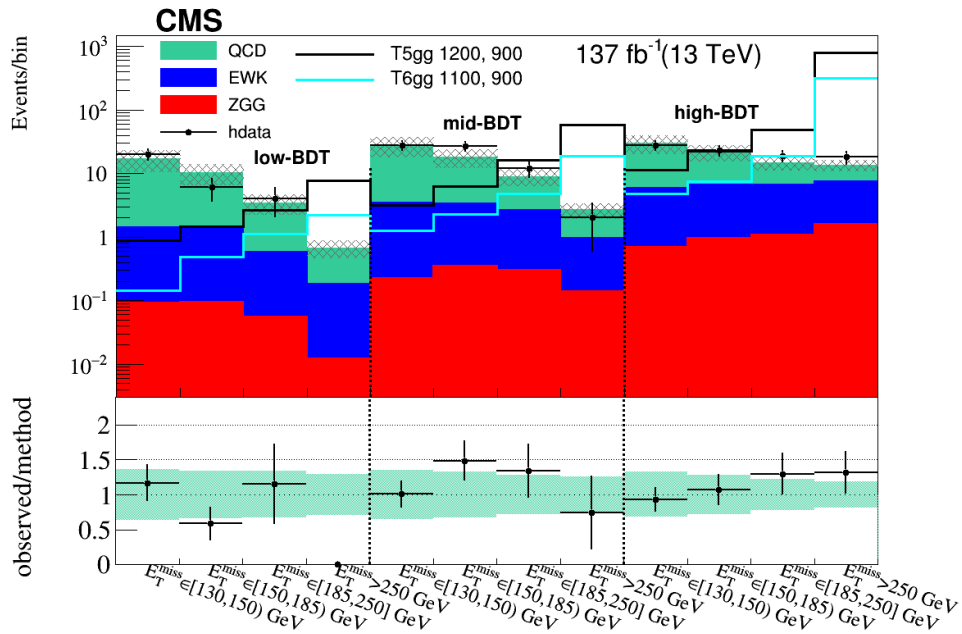

Fig. 8.1: The full background estimation and the observed data for the control and signal regions. The black points represent the observed data. The QCD background (green), the EWK background (blue), and the $Z\gamma\gamma$ backgrounds (red) are displayed as a stacked histogram. Two simulated signal distributions are also shown. The T5gg sample has a gluino mass of 1200 GeV and neutralino mass of 900 GeV. The T6gg sample has a squark mass of 1100 GeV and neutralino mass of 900 GeV.

8.3 respectively.

8.3 Statistical analysis

Upper limits for the production cross section of each signal model are evaluated using the modified frequentist method, CL_s, with a profile likelihood test statistic. The uncertainties that affect the predicted signal and background yields, s and b respectively, are incorporated by introducing nuisance parameters θ. We can then express the signal and background expectations

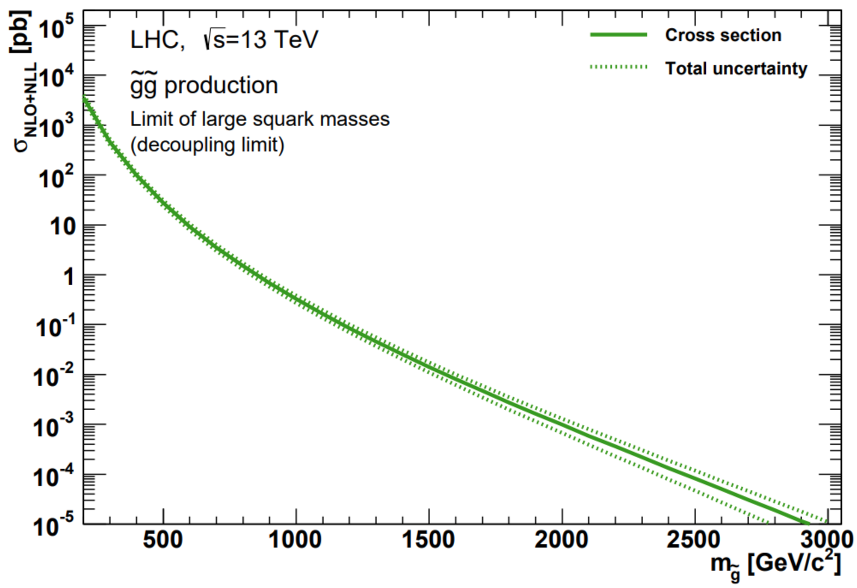

Fig. 8.2: The NLO+NLL cross section for gluino pair production as a function of gluino mass.

as functions of the nuisance parameters. The probability P for a given search region to contain n observed events when expecting to observe b background events and s signal events can be expressed with signal strength modifier μ and the set of nuisance parameters θ as a Poisson distribution as shown in Equation 8.1.

$$P(n|\mu,\theta) = \frac{(\mu s(\theta) + b(\theta))^n}{n!} e^{-(\mu s(\theta)+b(\theta))} \tag{8.1}$$

The probability distribution $p_i(\theta)$ for each nuisance parameter θ_i depends on the uncertainty that it represents. For statistical uncertainties the probability distribution is modeled with a gamma density distribution, while systematic uncertainties are modeled using a log-normal density distribu-

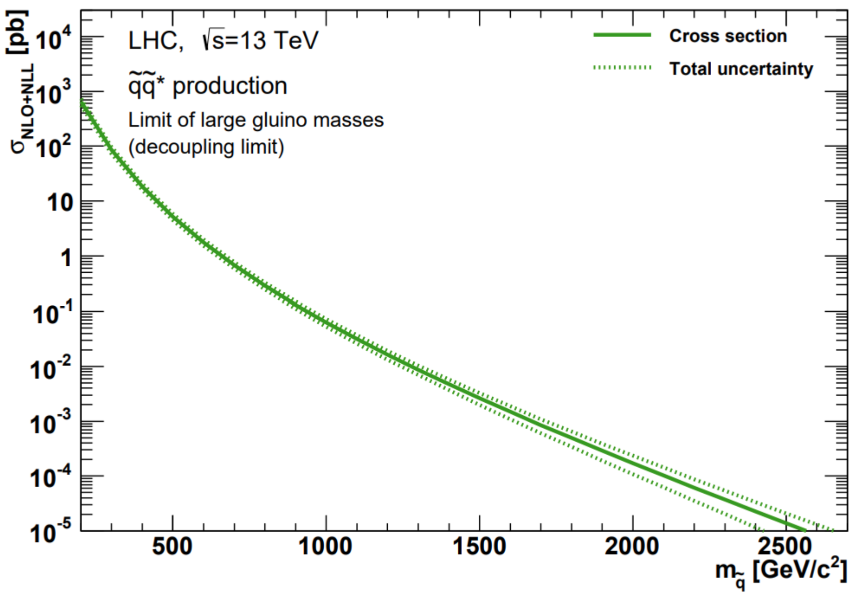

Fig. 8.3: The NLO+NLL cross section for squark pair production as a function of squark mass.

tion.

Combining all of the search regions we can make a likelihood function $\mathcal{L}$, which is the probability to have signal strength μ and the set of nuisance parameters θ given n_i events are observed observed in search region i.

$$\mathcal{L}(n|\mu,\theta) = \prod_i P(n_i|\mu,\theta) \prod_j p_j(\theta) \tag{8.2}$$

We then get the best fit values for μ and θ, which will be represented by $\hat{\mu}$ and $\hat{\theta}$, by maximizing $\mathcal{L}$. The test statistic t_μ is then used to quantify the compatibility of a given value of signal strength μ with the observed data.

That test statistic is defined as

$$t_{\mu} = -2\ln\frac{\mathcal{L}(n|\mu,\tilde{\theta})}{\mathcal{L}(n|\hat{\mu},\hat{\theta})} = -2\ln\frac{\mathcal{L}_{\mu}}{\mathcal{L}_{max}} \tag{8.3}$$

where $\tilde{\theta}$ is the nuisance parameter set with values that maximize $\mathcal{L}$ for a given value of μ. The ratio inside the natural log is essentially the maximum likelihood with fixed μ divided by the maximum likelihood. The best fit values for these nuisance parameters $\hat{\theta}_{\mu}$ are then used to generate toy MC pseudo-data in order to construct probability distributions for the background-only case, where we set $\mu = 0$, and the signal+background case. This gives the p-values for each hypothesis in terms of the a comparison between the value of test statistic resulting from the MC generated pseudo-data (t_{μ}) and the one resulting from observed data (t_{μ}^{obs}) as follows:

$$p_{\mu} = P(t_{\mu} \geq t_{\mu}^{obs}|signal + background) \tag{8.4}$$

$$1 - p_0 = P(t_0 \geq t_0^{obs}|background - only) \tag{8.5}$$

Using the CL$_s$ method, as described in [38] and [40], we have the Confidence Level

$$CL_s(\mu) = \frac{p_{\mu}}{1 - p_0}. \tag{8.6}$$

By adjusting μ until $CL_s = 0.05$ we get an upper limit on the signal strength $\mu^{95\%CL}$ for a particular model with a 95% Confidence Level. We would then say that any model for which $CL_s \leq 0.05$ is excluded. The cross section upper limit for model would then be the product of $\mu^{95\%CL}$ and the expected cross section of that model. This process yields the observed cross section upper limit as it uses real observed data being plugged into the test statistic t_μ. If instead we use background prediction we would get the expected cross section upper limits. Essentially, the expected upper limit is what we expect the find if there is no signal present, i.e. the background-only hypothesis is true.

8.4 Limits for T5gg and T6gg

The upper limits placed on production cross sections and the exclusion contours are shown in Figures 8.4 and 8.5 for the T5gg and T6gg simplified models respectively. The signal models in which the 95% CL upper limit on production cross section is less than the theoretical cross section are considered to be excluded. These excluded signal models are to the left of the exclusion contour. As discussed in the previous section, the expected limit exclusion contour tells us what the region of phase space we can expect to exclude if there is no signal present and everything we observe is processed consistent with the Standard Model. The observed limit exclusion contour tells us what region of phase space is excluded given the data that we observed.

From these observations lower limits were placed on the masses of the squarks and gluinos in the context of gauge mediated supersymmetry breaking. Models with squark masses below 1.79 TeV were excluded at a 95% confidence level as were models with gluino masses below 2.08 TeV. This is a substantial improvement over the previous results, seen in Figure 8.6, which placed these lower limits at 1.59 TeV and 1.86 TeV, respectively[44].

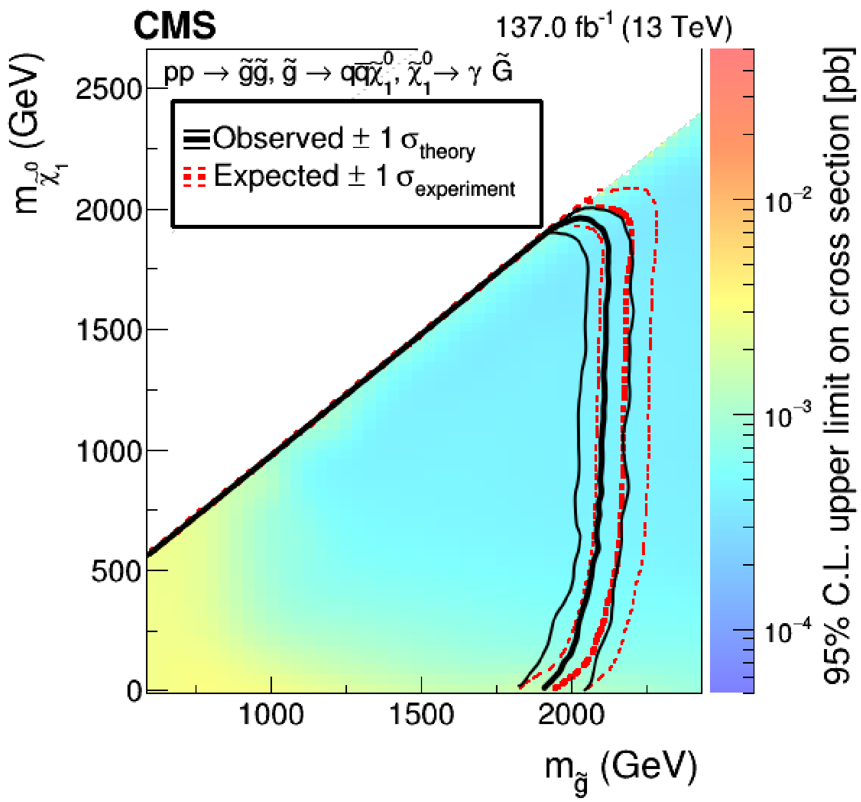

Fig. 8.4: Cross section limits for T5gg simplified model. The expected limit (black) is set by assuming that the observed data is consistent with the background-only model. Observed data in from the signal regions is not used in the calculation of the expected limit. The observed limit (red) is set using observed data from the signal regions.

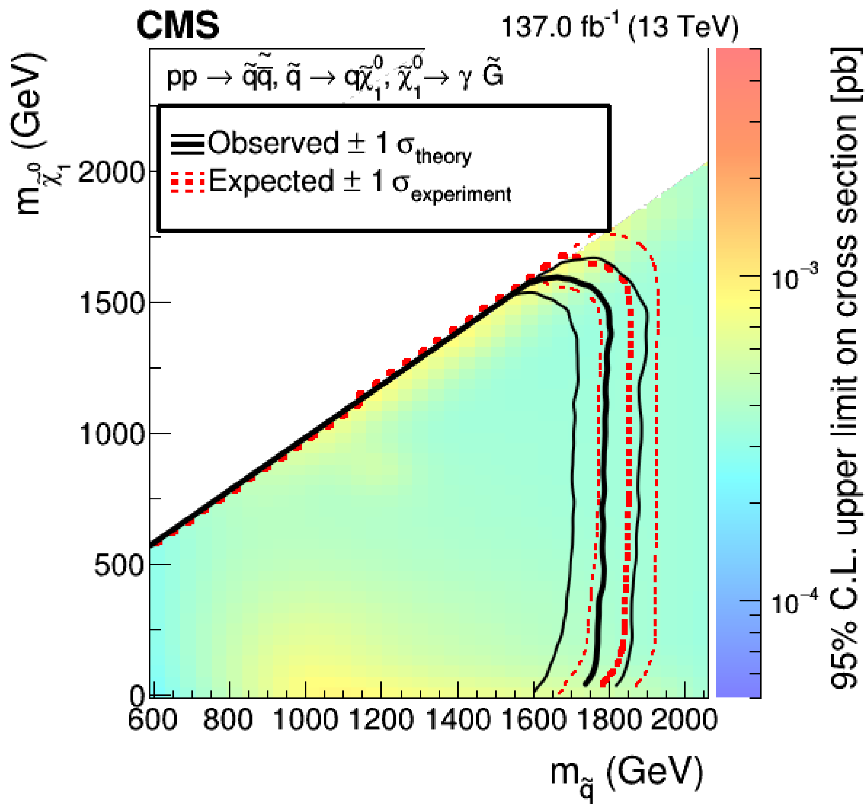

Fig. 8.5: Cross section upper limits for T6gg simplified model.The expected limit (black) is set by assuming that the observed data is consistent with the background-only model. Observed data in from the signal regions is not used in the calculation of the expected limit. The observed limit (red) is set using observed data from the signal regions.

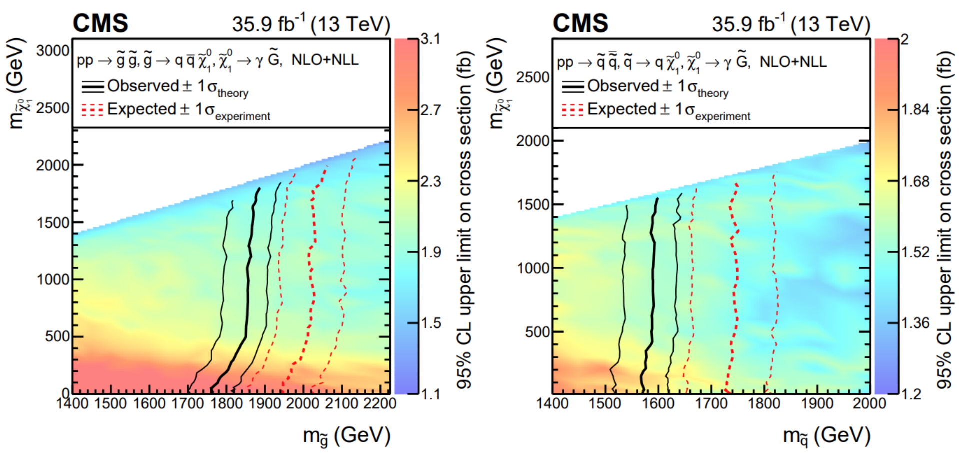

Fig. 8.6: These are the previous results using the T5gg and T6gg simplified models. On the left we see that the observed limit using the T5gg simplified model excludes models with gluino masses less than 1.86 TeV. On the right we see that the observed limit using the T6gg simplified model excludes models with squark masses lower than 1.59 TeV. Reprinted from [44].

9. CONCLUSIONS

A search for new physics in events having two photons, multiple hadronic jets, and missing transverse momentum is described in this thesis. The data used in this analysis was collected from 2016 to 2018 with the CMS detector and adds up to give an integrated luminosity of 137 fb^{-1}. Estimations for two fo the three primary backgrounds were fully data-driven while the third background estimation was data-constrained. A boosted decision tree was used to suppress the QCD background while the QCD background prediction was made using a variation of the Rebalance and Smear method which was modified to include the presence of photons and leptons. The tag-and-probe method was used to determine the rate at which electrons are misidentified as photons, which was then used to predict the EWK background by rescaling $e\gamma$ events. The $Z\gamma\gamma \rightarrow \nu\nu\gamma\gamma$ background was predicted from the simulation model which was renormalized using $Z\gamma\gamma \rightarrow ee\gamma\gamma$ and $Z\gamma\gamma \rightarrow \mu\mu\gamma\gamma$ events from data.

No evidence of physics beyond the Standard Model was observed. Lower limits were placed on the masses of SUSY particles in the context of gauge mediated supersymmetry breaking. In particular, this was done using two simplified models. One being the case where we assume gluino pair production and the other for squark pair production. Gluino masses below 2.08

TeV and squark masses below 1.79 TeV are excluded at a 95% confidence level. This is an improvement of 220 GeV for gluino mass and 200 GeV for squark mass.

Future versions of this analysis will benefit greatly from the greatly increased luminosity provided by the HL-LHC and new analysis tools available using the CMS MIP Timing Detector (MTD), both of which are discussed in the A. Just accounting for the increased amount of integrated luminosity, which should be approximately 3000 fb^{-1}, pushes the expected limit beyond the simulated SUSY masses used in this analysis which were 2.5 TeV for the gluino mass and 2.2 TeV for the squark mass. There is also the possibility to take advantage of the 30 ps timing resolution provide by the MTD. New analysis tools, such as secondary vertex timing and time-of-flight measurements are made possible with the MTD and have the potential to result in a substantial improvement.

APPENDIX

A. FUTURE IMPROVEMENTS: MIP TIMING DETECTOR (MTD)

In the coming years the LHC will be working toward upgrades that will lead a substantial increase in luminosity. The timeline for future operations of the LHC is shown in Figure A.1. In 2019 the LHC entered a two-year shutdown, Long Shutdown 2 (LS2). Upgrades of the LHC injector complex to increase the beam brightness will take place during this shutdown. After LS2 the LHC will enter Run 3 which will run for three years at 13-14 TeV. At the completion of Run 3 the LHC will enter Long Shutdown 3 (LS3) which will last approximately 2.5 years. During LS3 the optics in the interaction region will be upgraded to produce smaller beams at the interaction point. The completion of this upgrade will usher in the High Luminosity (HL-LHC) era or Phase 2 of LHC operations, during which the combination of brighter beams and a new focusing scheme at the IP allows for a potential luminosity of $2\text{x}10^{35}$ $\text{cm}^{-2}\text{s}^{-1}$ at the beginning of each fill [9].

The increased luminosity results in more interactions per bunch crossing or pileup. In order to limit the amount of pileup the experiments must disentangle to more manageable levels, the nominal scenario would be operating at a stable luminosity of 5.0×10^{34} cm^{-2} s^{-1}. This would limit the pileup to an average of 140. The ultimate scenario for operations would

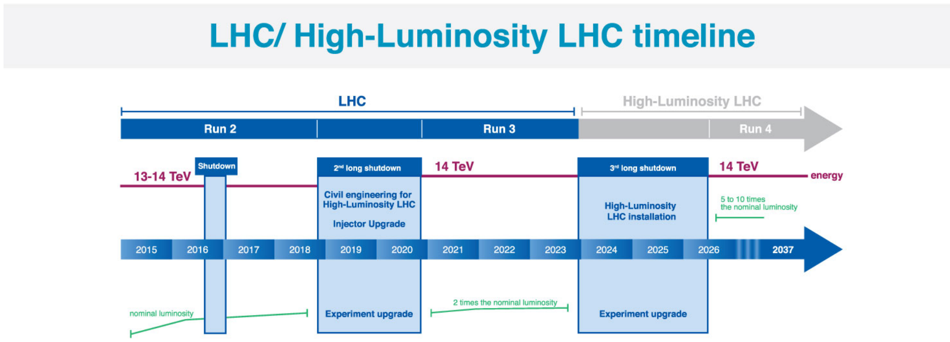

Fig. A.1: Timeline for LHC [26]

be running at 7.5×10^{34} cm^{-2} s^{-1} which brings the average pileup up to 200. The CMS detector in its current state is not capable of dealing with ≈140-200 pileup. At this level of pileup the spacial overlaps of tracks and energy depositions would lead to a degradation in the ability to identify and reconstruct hard interactions. In order to preserve the data quality of the current CMS detector this increased pileup must be reduced to an equivalent level approximately equal to current LHC operations which is ∼40. The collision vertices within a bunch crossing have an RMS spread of 180-200 ps in time. If the beam spot were to be sliced into consecutive snap shots of 30-40 ps then the pileup levels per snapshot would be approximately 40. The space-time reconstruction of a 200 pileup event is shown in Figure A.2. The addition of timing information to the z position spreads apart the vertices that would otherwise have been merged together and indiscernible. In order to achieve this a detector dedicated to the precise timing of minimum ionizing particles (MIPs), the MTD, will be added to the CMS detector.

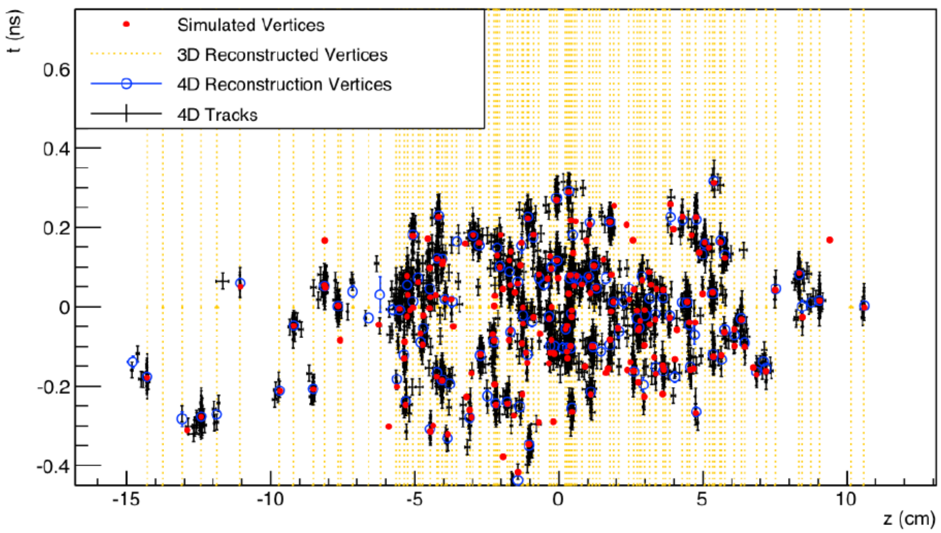

Fig. A.2: Vertices from a simulated 200 pileup event with MTD timing resolution of ∼30 ps. The red dots represent the simulated vertices while the yellow lines indicate vertices reconstructed without the use of timing information. The black crosses and blue open circles represent tracks and vertices reconstructed using time information from the MTD. Reprint from [14]

A.1 Barrel Timing Layer

The Barrel Timing Layer (BTL) makes up the barrel region of the MTD. It will provide pseudorapidity coverage up to $|\eta| = 1.48$ with a geometric acceptance of $\sim 90\%$. The BTL will be capable of detecting MIPs with a time resolution of 30 ps at the start of Phase-2 operations and a luminosity-weighted time resolution of ~ 45 ps when radiation damage effects are taken into account. The BTL is designed to operate without significant performance degradation over an integrated luminosity of at least 3000 fb^{-1}. The predicted level of radiation exposure over that integrated luminosity is listed in Table A.1. [14]

The fundamental element for MIP detection in the BTL is a thin scin-

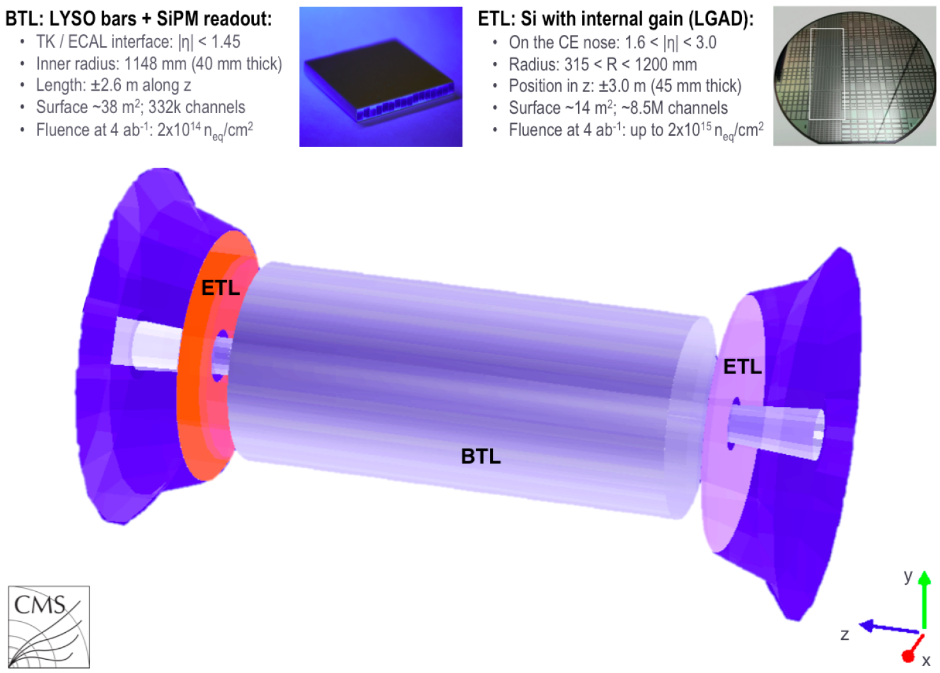

Fig. A.3: Schematic view of the proposed MTD implemented in the GEANT simulation of the CMS detector. The central region makes up the BTL which will be located in the space between the tracker and the ECAL. The ETL will be located in front of the endcap calorimeter. Reprint from [14]

tillating bar made of Lutetium Yttrium Orthosilicate crystals doped with Cerium ($(Lu_{1-X}Y_X)_2SiO_5 : Ce$) which is referred to as LYSO:Ce. The bars are 57 mm long, 3.12 mm wide, and have an average thickness of 3 mm. A silicon photomultiplier (SiPM) is attached to each end of the LYSO:Ce bar. This double-ended readout gives uniform time response along the length of the crystal by eliminating the time delay effect from light propagating along the crystal and the ability to extract positional information for tracking.

An overview of the BTL and its components is shown in Figure A.5. The longitudinal axis of each crystal bar is oriented along the ϕ-direction in the CMS detector. The crystals are grouped in 1×16 ($\phi \times z$) arrays that

Tab. A.1: Predicted radiation doses and fluences at different location of the BTL after an integrated luminosity of 3000 fb^{-1}. The two far right columns include a safety margin of 1.5.

			3000 fb^{-1}		1.5×3000 fb^{-1}	
$\lvert\eta\rvert$	r (cm)	z (cm)	n_{eq}/cm^2	Dose (kGy)	n_{eq}/cm^2	Dose (kGy)
0.0	116	0	1.65×10^{14}	18	2.48×10^{14}	27
1.15	116	170	1.80×10^{14}	25	2.70×10^{14}	38
1.45	116	240	1.90×10^{14}	32	2.85×10^{14}	48

each form a *module*. Each *module* has 32 SiPMs (2 for each bar) resulting in 32 readout channels. These *modules* are then grouped in a 3×8 ($\phi \times z$) arrangement to make up a readout unit (RU) as shown in Figure A.6. Each *module* is read out by a dedicated ASIC called the TOFHIR (Time-of-flight, High Rate) chip which is capable of reading out 32 channels at a time. The TOFHIR chip gives precision timing information using discrimination of the leading edge of pulses from the SiPMs followed by a time-to-digital converter (TDC). When using discrimination techniques like this the time for a pulse to cross the discriminating threshold depends on the height of the pulse. This results in an amplitude-dependent timing variation called time walk. In order to correct for this time walk effect the ASIC also measures pulse amplitude. Six ASICs are mounted on each of four front-end boards (FEBs) on a RU giving a total of 24 ASICs and 768 SiPMs per RU. The RUs are then arranged in trays along the z-direction. Each tray holds six RUs, runs along half the length of the detector, and spans 10° along ϕ. To summarize, a total of 72 trays (36 azimuthal sections each split into a $+z$ and $-z$ section) contain 331776 SiPMs and 165888 LYSO:Ce bars. This gives a detector granularity that has an average occupancy of about 7% at

200 pileup, which limits the likelihood of multiple hits within a single crystal during a bunch crossing.

In order to have a negligible impact on the energy resolution of the ECAL, the thickness of the LYSO:Ce crystals is varied along the z-axis of the detector. This variation is done in three sections such that the thickness of material is as uniform as possible while not exceeding 0.4 X_0 where X_0 is one radiation length. This is done in three sections as a function of η where crystal thicknesses of 3.75 mm, 3.0 mm, and 2.4 mm will be in the $|\eta|$ regions 0-0.7, 0.7-1.1, and 1.1-1.48 respectively. These details are outlined in Table A.2. Figure A.4 shows how the slant thickness changes along η in terms of radiation length for the case where crystal thicknesses are varied as outlined in Table A.2.

$\|\eta\|$ range	0-0.7	0.7-1.1	1.1-1.48
Crystal thickness (mm)	3.75	3.0	2.4
Average slant thickness (mm)	4.0	4.3	4.6

Tab. A.2: Summary of crystal and slant thicknesses in different η regions.

The "time stamp" provided by the BTL is a measurement of the time that a MIP crosses the detector. As a MIP passes through the volume of a LYSO:Ce crystal it will produce optical photons along its path. The number of photons produced is proportional to the light yield (LY) of the crystal, which is a function of the amount of energy deposited. Of these photons, a fraction of them will reflect along the length of the crystal bar and be detected by one of the two SiPMs mounted on the ends. The SiPMs convert these detected photons into photoelectrons to produce electrical signals which are then processed by the TOFHIR chip to provide the "time stamp"

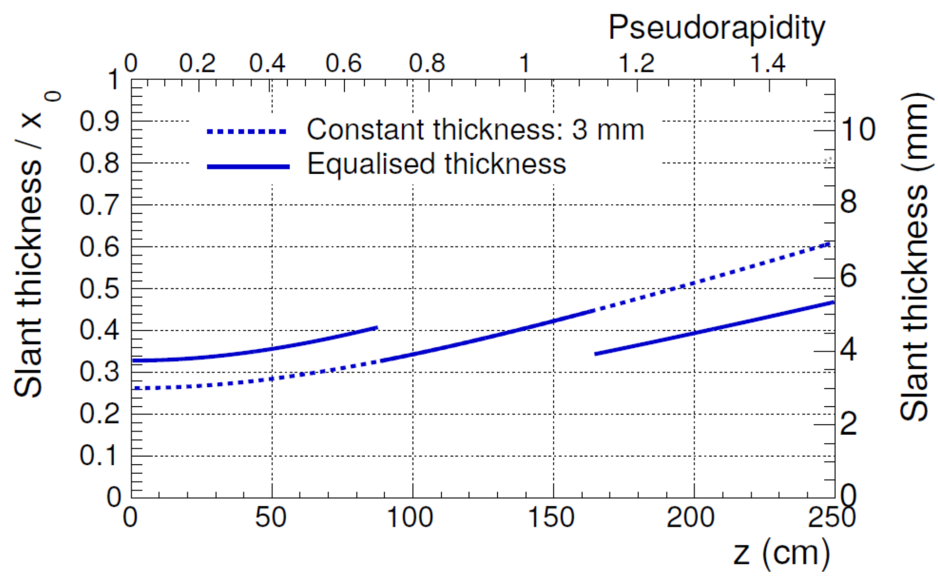

Fig. A.4: The left and right axes show the slant thickness in terms of radiation length and mm respectively. The dotted blue line shows the slant thickness if all LYSO:Ce bars were 3 mm thick while the solid line has bar thicknesses of 3.75, 3.0, and 2.4 mm. Reprinted from

for the MIP. Throughout this process there are multiple contributors to time resolution degradation. The sum of these contributions in quadrature as shown in Equation A.1 gives the overall time resolution for the BTL.

$$\sigma_t^{BTL} = \sigma_t^{clock} \oplus \sigma_t^{digi} \oplus \sigma_t^{ele} \oplus \sigma_t^{pho} \oplus \sigma_t^{DCR} \tag{A.1}$$

The individual contributions are shown in Table **??**. As one can see from this

Source	starting σ_t (ps)	end-of-life (3000 fb^{-1}) σ_t (ps)
Clock jitter	15	15
Digitization	7	7
Electronics	8	8
Photo-statistics	25	30
SiPM dark counts	negligible	50

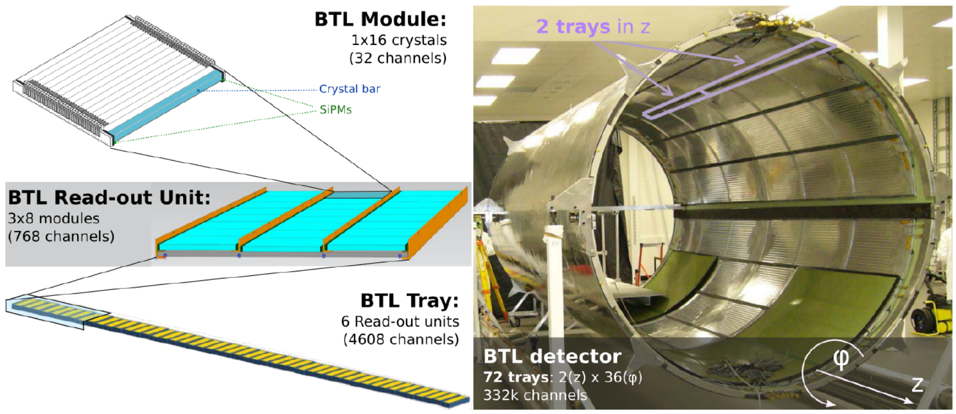

Fig. A.5: On the left is an overview showing how the various components of the BTL fit together into modules, read-out units, and trays. On the right is a view of how the trays will fit into the Tracker Support Tube (TST)

table, the two major factors in overall time resolution are photo-statistics and, at the end of life, dark counts or noise from the SiPMs. The evolution of timing performance of the BTL as a function of the integrated luminosity is shown in Figure A.7. It's clear that the two most important details required to obtain and preserve good time resolution are optimizing the photo-statistics and mitigating the increased noise produced by heavily irradiated SiPMs as the integrated luminosity approaches the 3000 fb^{-1} end of life target. [14]

A.1.1 LYSO:Ce crystals

As previously stated, photo-statistics has a major impact on the achievable time resolution of the BTL. The contribution to the overall time resolution

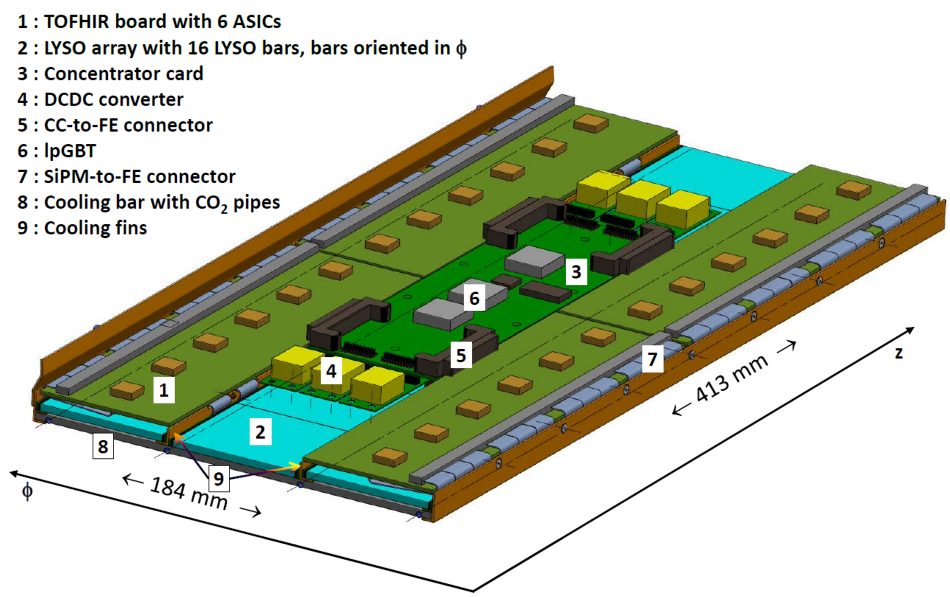

Fig. A.6: Readout unit for the BTL.

can be expressed as

$$\sigma_t^{pho} \propto \sqrt{\frac{\tau_r \tau_d}{N_{phe}}} \propto \sqrt{\frac{\tau_r \tau_d}{E_{dep} \times LY \times LCE \times PDE}}, \tag{A.2}$$

where the rise and decay times of the scintillation pulses are τ_r and τ_d respectively, N_{phe} is the number of photoelectrons produced, E_{dep} is the energy deposited in the crystal, LY is the light yield, LCE is the light collection efficiency which is the fraction of optical photons that make it down the length of the crystal to the SiPMs, and PDE is the photon detection efficiency which is the fraction of photons incident on the SiPM surface that are detected. From Equation A.2 we see that an ideal candidate material for the crystals is one with fast decay and rise times, large E_{dep}, and high LY. LYSO:Ce has a decay time $\sim$ 40 ns and a rise time $<$ 100 ps [34]. The

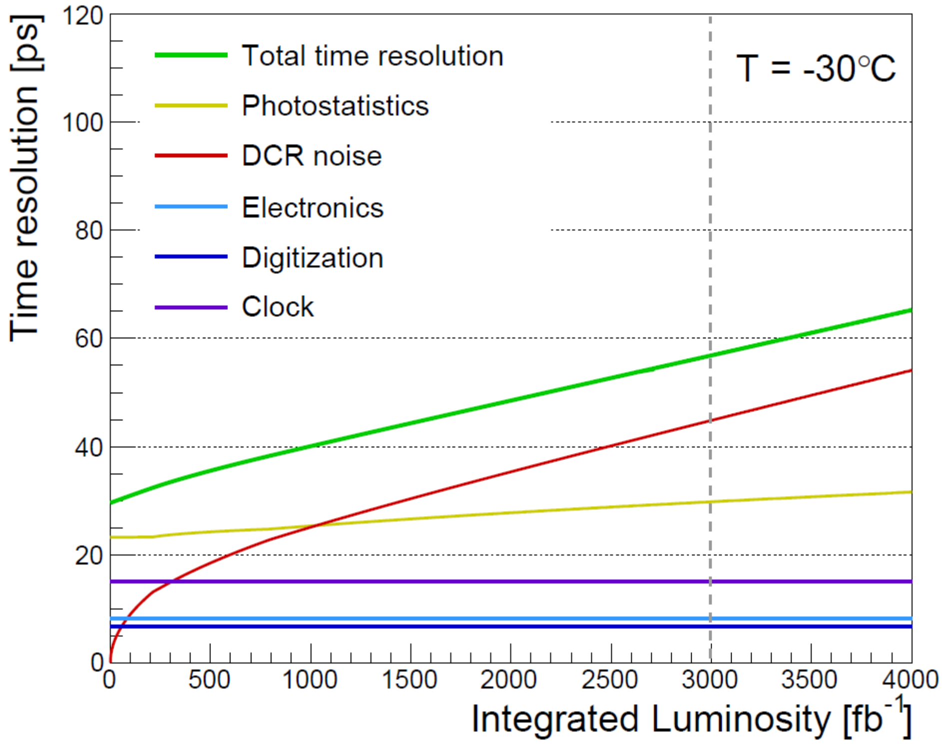

Fig. A.7: Evolution of time resolution for the BTL.

energy deposited by a MIP in a crystal follows a Landau distribution with the most probably value being at 0.86 MeV/mm. For the BTL crystals a MIP deposits an average energy of 4.2 MeV when accounting for the longer path lengths within the LYSO:Ce volume due to track bending in the magnetic field. While the LY is about 40000 photons/MeV, the most important photons are the ”early photons” which are those produced in the first 500 ps of scintillation. LYSO:Ce produces approximately 400 early photons/MeV resulting in about 2000 early photons being produced per MIP in the BTL.

Additionally, these crystals must be tolerant to radiation levels up to those listed in Table A.1 with the 1.5 safety margin. Comparing the change in transparency of LYSO:Ce after exposure to 24 GeV proton to a 2.5×10^{13} cm^{-2} fluence, which is more than the expected level including the safety margin, show a negligible loss in transparency T (Figure A.8). At the LYSO:Ce peak scintillation wavelength of 420 nm the induced absorption coefficient is

$$\mu_{ind} = \frac{\ln(T_{before}/T_{after})}{L} = 0.5m^{-1} \tag{A.3}$$

where L is the length of the crystal bar. In addition to investigating the

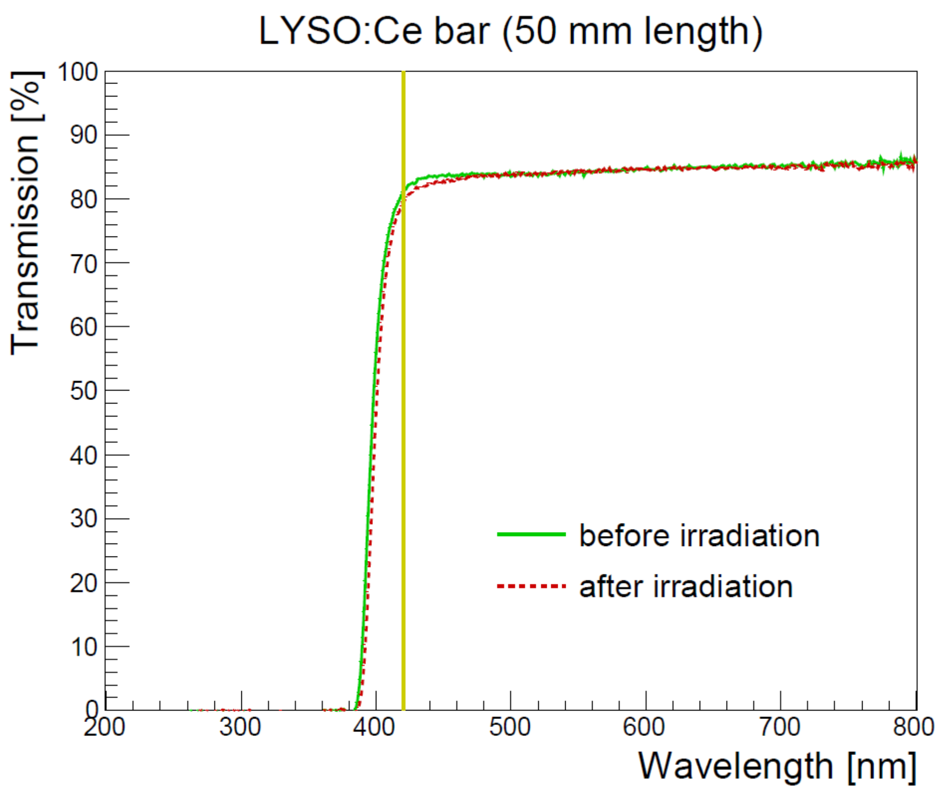

Fig. A.8: Transmission curve across a 50 mm long bar of LYSO:Ce before and after being irradiated to a fluence of 2×10^{13} cm^{-2} with 24 GeV protons. The vertical line indicates the peak wavelength in the scintillation emission spectrum of LYSO:Ce.

changes in optical transmission, the effect on the timing resolution was also checked to insure that the observed changes in the transmission did not have a substantial effect on the timing performance. The time resolution before and after irradiation was measured using 511-keV photons from a Na^{22} source with the results shown in A.9. This shows that there is no statistically significant change in the time resolution due to the radiation induced changes in optical transmission.

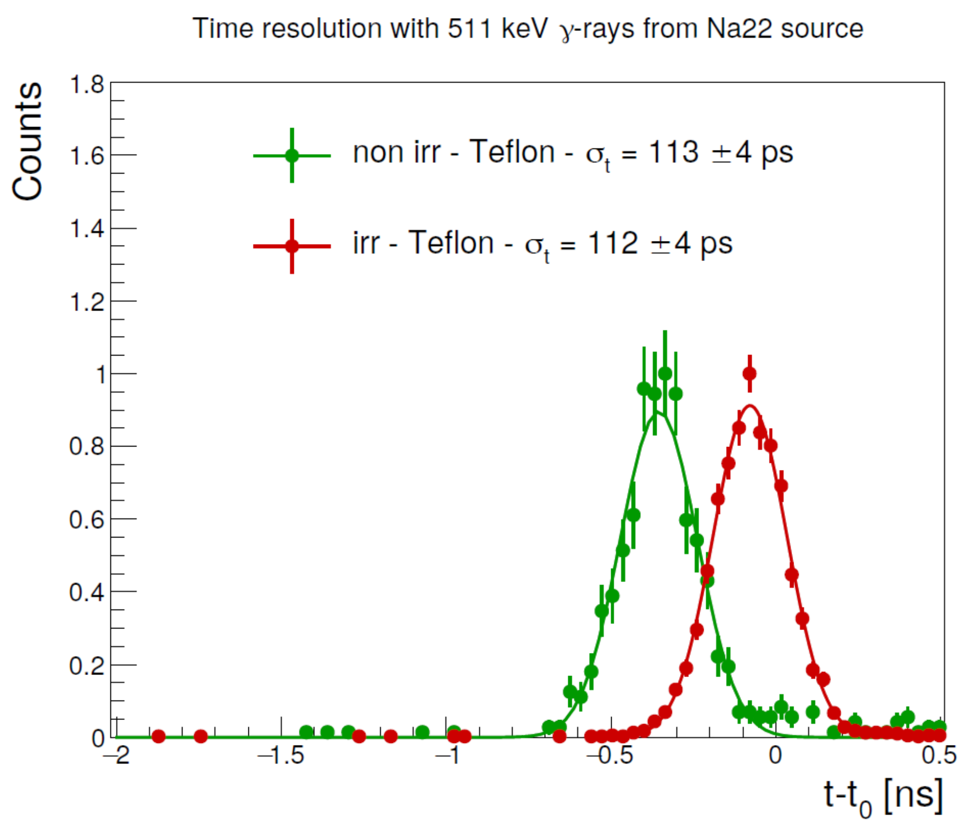

Fig. A.9: The time resolution of a 50 mm long LYSO:Ce bar was measured before and after being irradiated with 24 GeV protons to a 2×10^{13} cm^{-2} fluence. The time resolution was measured using 511 keV photons from a Na^{22} source. There was no significant change in time resolution after being irradiated.

A.1.2 SiPMs

Silicon photomultiplier (SiPMs) were chosen as the photo-sensor to be used in the BTL. In contrast to conventional photomultiplier tubes, SiPMs are compact, robust, and insensitive to external magnetic fields. Several different SiPMs technologies were considered for the BTL. Some important characteristics to consider are radiation tolerance, photon detection efficiency, power consumption, and timing performance. In consideration were the NUV-HD (thin-epi) SiPM from Fondazione Bruno Kessler (FBK) and the S12572 and HDR2 SiPMs which are both produced by Hamamatsu Photonics (HPK). SiPMs with a 15 μm cell size were chosen as it gave the best balance between radiation tolerance and PDE.

A.1.3 Glue qualification

The LYSO:Ce bars and SiPMs will be coupled together using an optical glue. Preliminary glue candidates were chosen to have an index of refraction similar to that of LYSO:Ce and good optical transmission at the peak wavelength of the LYSO:Ce emission spectrum (420 nm). These candidates were NOA-61, RTV-3145, Epotek, Polytec, BC-600, and Meltmount. Additional constraints were that the glues be mechanically strong, capable of withstanding temperatures ranging from -40 to +60°C, and resistant to an ionizing dose of radiation up to $\sim$50 kGy (less than 3% loss in transparency). As Meltmount has a melting temperature below 50°C, it was eliminated from consideration. The remaining glue candidates were tested for radiation hardness using a Cs^{137} irradiator at the University of Virginia

Medical Research Facility which provided an ionizing dose at a rate of 2 Gy/min. The primary decay mode for Cs^{137} is a beta decay to an excited state of Ba^{137} which then produces a 662 keV photon when dropping into its ground state. The energy spectrum of for Cs^{137} is shown in Figure A.10. A preliminary test of radiation tolerance was performed using samples pre-

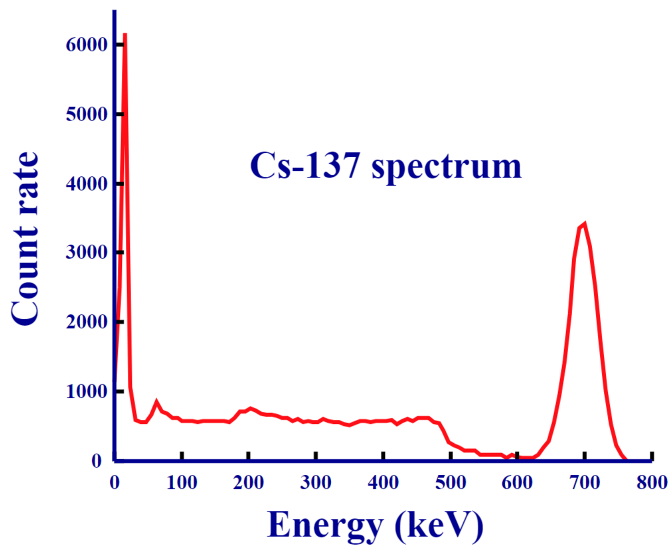

Fig. A.10: Energy spectrum for Cs^{137}.

pared by injecting glue into a teflon mold such as the one shown in Figure A.11a. Once cured, the glue samples (Figure A.11b)were removed from the mold and placed in the Cs^{137} irradiator. The received ionizing dose was calculated by multiplying the total time of exposure by the rate of 2 Gy/min. The results, shown in Figure A.12, narrowed the list of candidates down to NOA-61 and RTV-3145.

At this point a more precise examination of the radiation tolerances for NOA-61 and RTV-3145 were carried out by monitoring transmission

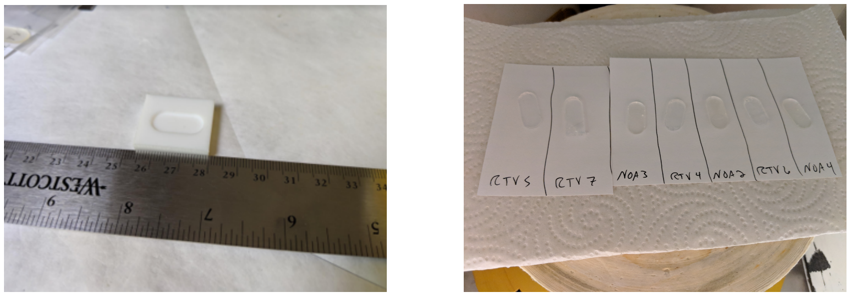

(a) Teflon mold used to produce glue samples

(b) Glue samples used for preliminary radiation tolerance studies

Fig. A.11: Left: This is a teflon mold used to produce glue samples. Right: The glue samples after being removed from the mold. These samples were then placed in the irradiator for radiation exposure.

properties before and after several subsequent exposures until reaching the integrated ionizing dose of about 50 kGy. Transmission measurements were taking using a photo-spectrometer which directs a beam of light with known wavelength through a sample and into a photo-sensor. In order to minimize optical effects not related to radiation damage the samples need to have uniform thickness and surfaces that are both smooth and parallel. To accomplish this the glue samples for this test were prepared by placing glue between two 1-mm thick quartz tiles which were separated by 1-mm thick spacers. The quartz provided smooth surfaces while the spacers insured uniform glue thicknesses and parallel surfaces. Separate transmission measurements were taken with bare quarts tiles that were irradiated alongside the glue samples and showed negligible optical degradation. The transmission curves for both NOA-61 and RTV-3145 are shown in Figure A.14. The comparison of their performance at a wavelength of 420 nm (the peak of the LYSO:Ce emission spectrum) is shown in A.14c. NOA-61 provides better performance prior to irradiation but degrades as the ionizing dose increases. RTV-3145 is less affected and despite starting with a lower transmission ends up with a higher transmission after the full ionizing dose. With the expected thickness of the glue layers in the BTL to be 50 μm or thinner, both glues would have less than 3% loss in transparency and therefore meet the radiation tolerance requirement.

As previously mentioned, the glues would need to withstand temperature ranges from -40 to +60°C. This was checked by gluing pairs of SiPMs to a crystal bar and thermally cycled several times between the aforementioned temperatures. Neither glue showed visible transparency loss nor did they show any signs of structural degradation such as cracks. The bond created by both glues remained mechanically strong. The SiPMs glued with NOA-61 could not be removed from the crystal bar without severely damaging the SiPMs. Those glued with RTV-3145 could be removed but only by applying a large amount of torsion. As it is, both glues remain potential candidates as they have both surpassed the standards required for usage in the BTL. RTV-3145 is slightly favored as it was used in the CMS ECAL with good results and has been shown to be more radiation tolerant than NOA-61. Another benefit of RTV-3145 over NOA-61 is that the crystal bars will be covered in a wrapping prior to gluing. This is problematic for NOA-61 because it requires exposure to UV light in order to cure and this is made difficult by the opaque wrapping.

A.1.4 Performance at test beam

Test beam facilities at both CERN and Fermilab were used to test the BTL sensor prototypes throughout the research and development process. These facilities provide well calibrated sources of MIPs in the form of high energy pions at CERN and protons at Fermilab.

Among the first test beam campaigns was an investigation of potential LYSO:Ce geometries and SiPM arrangements. Figure A.15 shows three configurations. All of these configuration used HBK S12572 SiPMs having a 3×3 mm^2 sensitive area and 15 μm cell pitch. These were, from left to right, a $5 \times 3 \times 3$ mm^3 bar with one SiPM on each end, a $5 \times 5 \times 3$ mm^3 tile with an array of three SiPMs on each side, and a $5 \times 5 \times 3$ mm^3 tile with a single SiPM centered on the back. The crystals were wrapped in Teflon to limit external light leakage. The time resolution for the tiles showed impact point position dependence while using the average time between the two SiPMs on the bar showed a minimal dependence. This led to the decision to use a bar geometry for the scintillating crystal with SiPMs connected to each end.

The next step was to verify that the target of 30 ps time resolution was attainable with the bar geometry. In this test beam campaign the same type of SiPMs, HBK 12572, were used. This time they were connected to a $50 \times 3 \times 3$ mm^3 LYSO:Ce bar. Figure A.16 shows the experimental configuration used. In addition to what is shown, a microchannel plate detector (MCP) was placed downstream of the bars to act as a time reference. The time resolution was determined by taking the standard deviation of the average time of a MIP signal relative the time of a signal in the MCP which is shown here.

$$t_{avg} = \frac{(t_L - t_{MCP}) + (t_R - t_{MCP})}{2} \tag{A.4}$$

This gives a time resolution of

$$\sigma_{t_{avg}} = \frac{\sigma_{t_{L,R}}}{\sqrt{2}} \tag{A.5}$$

The results are shown in Figure A.17 where we see the average time resolution along the length of the bar is around 28 ps. There is ongoing research and development for the MTD and with its proven time resolution capabilities it will be a very promising addition to the CMS experiment.

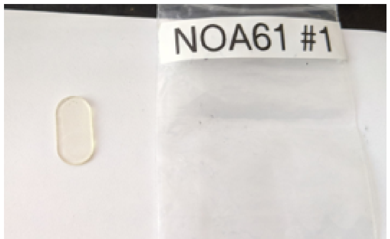

(a) NOA-61 irradiated to 13.7 kGy

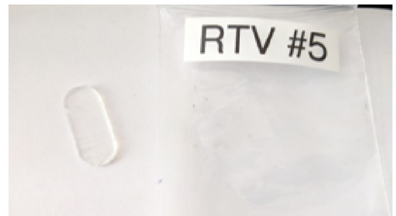

(b) RTV-3145 irradiated to 7.9 kGy

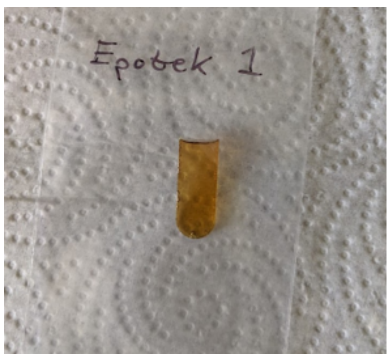

(c) Epotek irradiated to 7.9 kGy

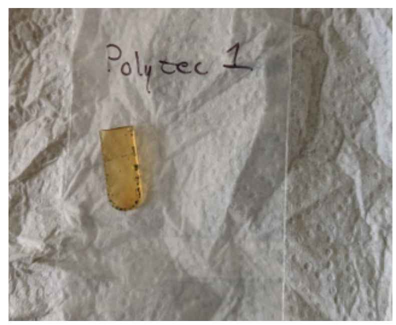

(d) Polytec irradiated to 7.9 kGy

(e) BC-600 irradiated to 10.8 kGy

Fig. A.12: Preliminary radiation tolerance studies of the top five glue candidates show that only NOA-61 and RTV-3145 are viable. Epotek, Polytec, and BC-600 all show substantial optical degradation after just a fraction of 50 kGy target.

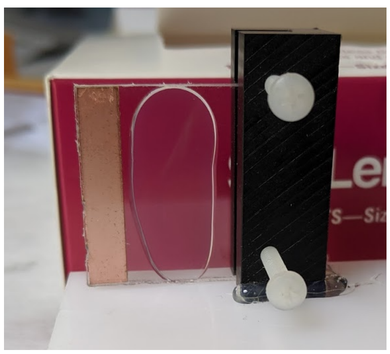

(a) Glue sample between two quartz slides

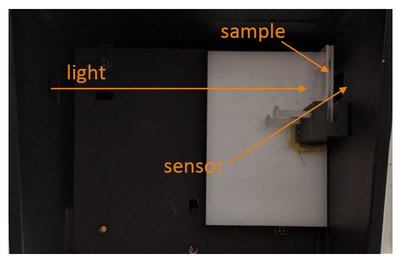

(b) Glue sample positioned in photo-spectrometer

Fig. A.13: Figure A.13a shows an example a glue sample ready for transmission measurements. Figure A.13b shows how the measurement is taken with the sample placed inside the photo-spectrometer.

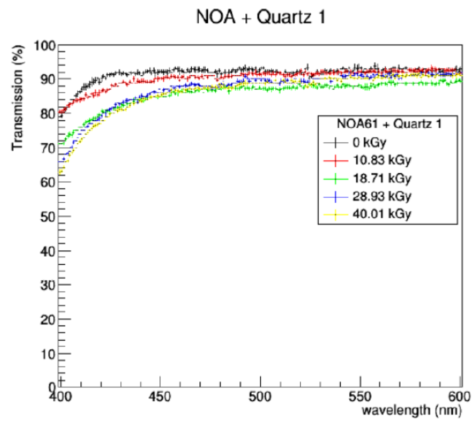

(a) Optical transmission curves for NOA-61 with increasing doses of radiation

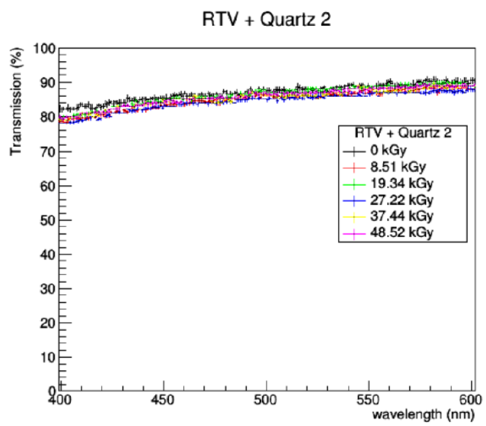

(b) Optical transmission curves for RTV-3145 with increasing doses of radiation

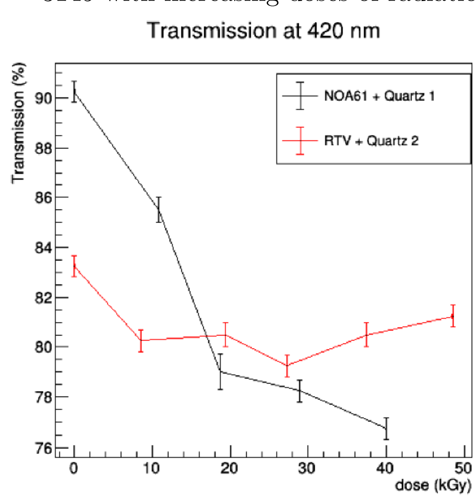

(c) Transmission at at wavelength of 420 nm after various ionizing doses

Fig. A.14: Transmission curves for both NOA-61 (Figure A.14a and RTV-3145 (Figure A.14b). Figure A.14c shows the transmission at 420 nm, the peak of the LYSO:Ce emission spectrum, with increasing ionizing doses. While NOA-61 starts with a higher transmission, RTV-3145 is more radiation tolerant and has a higher transmission after the full ionizing dose.

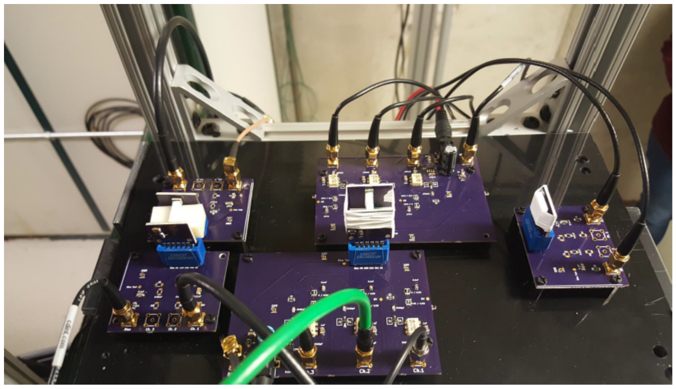

Fig. A.15: Three BTL sensor configurations investigated during a test beam campaign at Fermilab. On the left is a $5 \times 3 \times 3$ mm^3 LYSO:Ce bar instrumented with SiPMs on both ends. In the middle is a $5 \times 5 \times 3$ mm^3 tile with an array of three SiPMs on each side. To the right is $5 \times 5 \times 3$ mm^3 tile with a single SiPM in the middle behind the tile.

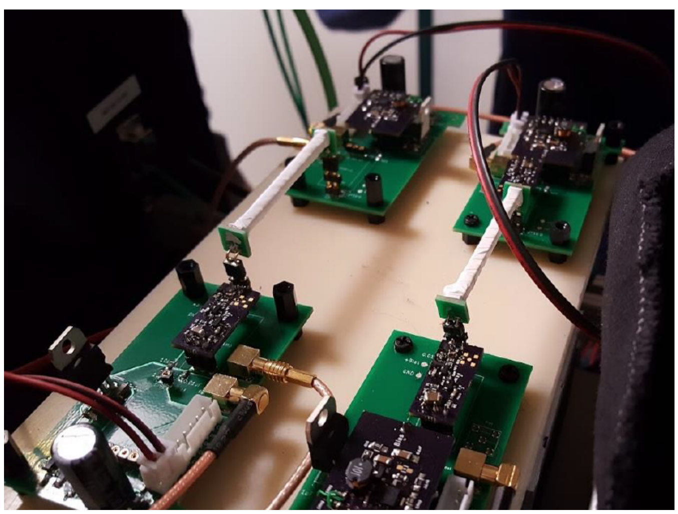

Fig. A.16: Two bar assemblies with SiPMs tested during a test beam campaign at Fermilab. The LYSO:Ce bars had a cross-section of 3×3 mm^2 and a length of 50 mm with HBK 12572 SiPMs instrumented on both ends. The bars were wrapped in teflon tape to minimize light leaking into the crystal.

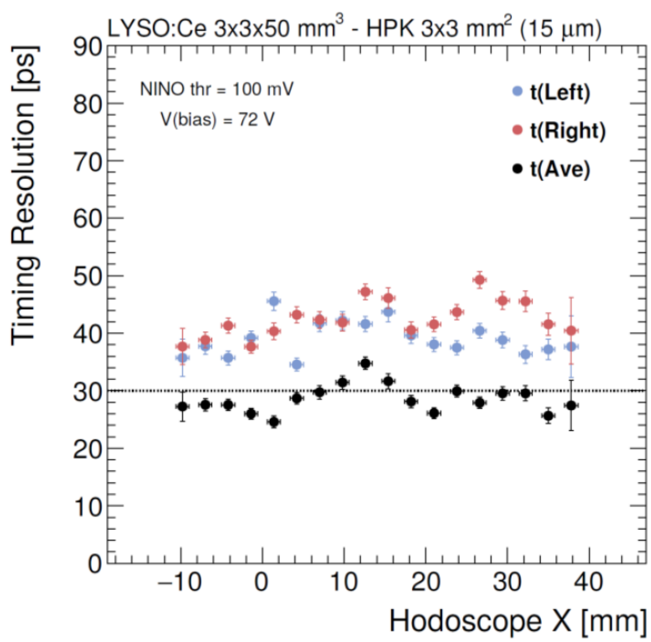

Fig. A.17: The time resolution measured for the SiPMs + LYSO:Ce bar configuration. The red and blue data points are for each SiPM on the bar while the black data points are the average of the two.

BIBLIOGRAPHY

[1] *The CMS electromagnetic calorimeter project: Technical Design Report*. Technical design report. CMS. CERN, Geneva, 1997.

[2] *The CMS hadron calorimeter project: Technical Design Report*. Technical design report. CMS. CERN, Geneva, 1997.

[3] CMS Technical Design Report for the Level-1 Trigger Upgrade. 6 2013.

[4] Georges Aad et al. Observation of a new particle in the search for the Standard Model Higgs boson with the ATLAS detector at the LHC. *Phys. Lett. B*, 716:1–29, 2012.

[5] S. Abdullin, P. Azzi, F. Beaudette, P. Janot, and A. Perrotta. The fast simulation of the CMS detector at LHC. *J. Phys. Conf. Ser.*, 331:032049, 2011.

[6] S. Abdullin et al. The CMS barrel calorimeter response to particle beams from 2-GeV/c to 350-GeV/c. *Eur. Phys. J. C*, 60:359–373, 2009. [Erratum: Eur.Phys.J.C 61, 353–356 (2009)].

[7] L. Alvarez-Gaume and J. Ellis. Eyes on a prize particle. *Nature Phys*, 7:2–3, 2011.

[8] J. Alwall, R. Frederix, S. Frixione, V. Hirschi, F. Maltoni, O. Mattelaer, H. S. Shao, T. Stelzer, P. Torrielli, and M. Zaro. The automated computation of tree-level and next-to-leading order differential cross sections, and their matching to parton shower simulations. *JHEP*, 07:079, 2014.

[9] G. Apollinari, O. Brüning, T. Nakamoto, and Lucio Rossi. High Luminosity Large Hadron Collider HL-LHC. *CERN Yellow Rep.*, (5):1–19, 2015.

[10] S Baird. Accelerators for pedestrians; rev. version. Technical Report AB-Note-2007-014. CERN-AB-Note-2007-014. PS-OP-Note-95-17-Rev-2. CERN-PS-OP-Note-95-17-Rev-2, CERN, Geneva, Feb 2007.

[11] David Barney. CMS Slice, https://cds.cern.ch/record/2628641. Feb 2015.

[12] Gianfranco Bertone, Dan Hooper, and Joseph Silk. Particle dark matter: Evidence, candidates and constraints. *Phys. Rept.*, 405:279–390, 2005.

[13] Christoph Borschensky, Michael Krämer, Anna Kulesza, Michelangelo Mangano, Sanjay Padhi, Tilman Plehn, and Xavier Portell. Squark and gluino production cross sections in pp collisions at $\sqrt{s} = 13$, 14, 33 and 100 TeV. *Eur. Phys. J. C*, 74(12):3174, 2014.

[14] Joel N. Butler and Tommaso Tabarelli de Fatis. A MIP Timing Detector for the CMS Phase-2 Upgrade. 2019.

[15] Matteo Cacciari, Gavin P. Salam, and Gregory Soyez. The anti-k_t jet clustering algorithm. *JHEP*, 04:063, 2008.

[16] L. Cadamuro. The CMS Level-1 trigger system for LHC Run II. *JINST*, 12(03):C03021, 2017.

[17] Jean-Luc Caron. Cross section of lhc dipole.. dipole lhc: coupe transversale. "AC Collection. Legacy of AC. Pictures from 1992 to 2002.", May 1998.

[18] S Chatrchyan et al. Performance of CMS Muon Reconstruction in Cosmic-Ray Events. *JINST*, 5:T03022, 2010.

[19] S Chatrchyan et al. Precise Mapping of the Magnetic Field in the CMS Barrel Yoke using Cosmic Rays. *JINST*, 5:T03021, 2010.

[20] Serguei Chatrchyan et al. Observation of a New Boson at a Mass of 125 GeV with the CMS Experiment at the LHC. *Phys. Lett. B*, 716:30–61, 2012.

[21] CMS Collaboration. EGM ID recipes Run II, https://twiki.cern.ch/twiki/bin/view/CMS/EgammaIDRecipesRun2.

[22] CMS Collaboration. CMS Technical Design Report for the Pixel Detector Upgrade. Technical Report CERN-LHCC-2012-016. CMS-TDR-11, Sep 2012. Additional contacts: Jeffrey Spalding, Fermilab, Jeffrey.Spalding@cern.ch Didier Contardo, Universite Claude Bernard-Lyon I, didier.claude.contardo@cern.ch.

[23] CMS Collaboration. Description and performance of track and primary-vertex reconstruction with the CMS tracker. *JINST*, 9(CMS-TRK-11-001. CERN-PH-EP-2014-070. CMS-TRK-11-001):P10009. 80 p, May 2014. Comments: Replaced with published version. Added journal reference and DOI.

[24] The CMS Collaboration. The CMS experiment at the CERN LHC. *Journal of Instrumentation*, 3(08):S08004–S08004, aug 2008.

[25] The CMS collaboration. The performance of the CMS muon detector in proton-proton collisions at $\sqrt{s}$=7 TeV at the LHC. *Journal of Instrumentation*, 8(11):P11002–P11002, nov 2013.

[26] Cinzia De Melis. Timeline for the LHC and High-Luminosity LHC. Frise chronologique du LHC et du LHC haute luminosité. Oct 2015. General Photo.

[27] J. D'Hondt, S. Lowette, O. L. Buchmuller, S. Cucciarelli, F. P. Schilling, M. Spiropulu, S. Paktinat Mehdiabadi, D. Benedetti, and L. Pape. Fitting of event topologies with external kinematic constraints in CMS. 1 2006.

[28] John R. Ellis. Limits of the standard model. In *PSI Zuoz Summer School on Exploring the Limits of the Standard Model*, 11 2002.

[29] Lyndon Evans and Philip Bryant. LHC machine. *Journal of Instrumentation*, 3(08):S08001–S08001, aug 2008.

[30] R. Fruhwirth. Application of Kalman filtering to track and vertex fitting. *Nucl. Instrum. Meth. A*, 262:444–450, 1987.

[31] Murray Gell-Mann. A Schematic Model of Baryons and Mesons. *Phys. Lett.*, 8:214–215, 1964.

[32] Kristin Goebel. *Probing supersymmetry based on precise jet measurements at the CMS experiment*. PhD thesis, U. Hamburg, Dept. Phys., 2015.

[33] J. Goldstone. Field Theories with Superconductor Solutions. *Nuovo Cim.*, 19:154–164, 1961.

[34] S. Gundacker, R. M. Turtos, E. Auffray, and P. Lecoq. Precise rise and decay time measurements of inorganic scintillators by means of X-ray and 511 keV excitation. *Nucl. Instrum. Meth. A*, 891:42–52, 2018.

[35] Peter W. Higgs. Broken Symmetries and the Masses of Gauge Bosons. *Phys. Rev. Lett.*, 13:508–509, 1964.

[36] Andreas Hocker et al. TMVA - Toolkit for Multivariate Data Analysis. 3 2007.

[37] Yutaro Iiyama. *Search for Supersymmetry in pp Collisions at $\sqrt{s}$ = 8 TeV with a Photon, Lepton, and Missing Transverse Energy*. PhD thesis, Carnegie Mellon U., 2 2015.

[38] Thomas Junk. Confidence level computation for combining searches with small statistics. *Nucl. Instrum. Meth. A*, 434:435–443, 1999.

[39] Stephen P. Martin. A Supersymmetry primer. *Adv. Ser. Direct. High Energy Phys.*, 18:1–98, 1998.

[40] Alexander L. Read. Presentation of search results: The CL(s) technique. *J. Phys. G*, 28:2693–2704, 2002.

[41] Jonas Rembser. CMS Electron and Photon Performance at 13 TeV. *J. Phys.: Conf. Ser.*, 1162(1):012008. 8 p, 2019.

[42] Tai Sakuma and Thomas McCauley. Detector and event visualization with SketchUp at the CMS experiment. *Journal of Physics: Conference Series*, 513(2):022032, jun 2014.

[43] Albert M Sirunyan et al. Search for supersymmetry in multijet events with missing transverse momentum in proton-proton collisions at 13 TeV. *Phys. Rev. D*, 96(3):032003, 2017.

[44] Albert M Sirunyan et al. Search for supersymmetry in final states with photons and missing transverse momentum in proton-proton collisions at 13 TeV. *JHEP*, 06:143, 2019.

[45] A.M. Sirunyan et al. Performance of the CMS muon detector and muon reconstruction with proton-proton collisions at $\sqrt{s}$=13 TeV. *Journal of Instrumentation*, 13(06):P06015–P06015, jun 2018.

[46] Torbjorn Sjostrand, Stephen Mrenna, and Peter Z. Skands. A Brief Introduction to PYTHIA 8.1. *Comput. Phys. Commun.*, 178:852–867, 2008.

[47] Mark Terwort. Searches for GMSB at the LHC. In *16th International Workshop on Deep Inelastic Scattering and Related Subjects*, page 110, 5 2008.

[48] Steven Weinberg. The Making of the standard model. *Eur. Phys. J. C*, 34:5–13, 2004.

[49] J. Wittmann, B. Arnold, H. Bergauer, M. Jeitler, T. Matsushita, D. Rabady, B. Rahbaran, and C.-E. Wulz. The upgrade of the CMS global trigger. *Journal of Instrumentation*, 11(02):C02029–C02029, feb 2016.

[50] Chen-Ning Yang and Robert L. Mills. Conservation of Isotopic Spin and Isotopic Gauge Invariance. *Phys. Rev.*, 96:191–195, 1954.

[51] G. Zweig. *An SU(3) model for strong interaction symmetry and its breaking. Version 2.* 2 1964.